Yuji Hasegawa

TECHNISCHE UNIVERSITÄT WIEN
Vienna | Austria

Diplomarbeit

Spin-Rotation Coupling in a Neutron Polarimeter Experiment

ausgeführt am Atominstitut
der TU Wien

unter der Anleitung von

Ass.-Prof. Dipl.-Ing. Dr. Yuji Hasegawa

durch

Armin Danner
Neulerchenfelder Straße 13/8, 1160 Vienna

Datum

Armin Danner

To my family.

Abstract

This thesis studies an effect of rotations on the spin of neutrons $\vec{S}$. In quantum mechanics, one means to describe the effects are geometrical phases, whose study has been a productive field since their description by Berry [1]. The phase caused by spin-rotation coupling is written in a Hamiltonian as an additional term $\vec{\Omega} \cdot \vec{S}$ with the rotations vector $\vec{\Omega}$. Mashhoon and co-authors proposed in a series of articles [2–4] experimental set-ups to single out and measure the spin-rotation coupling with neutrons in an interferometer experiment. The latest paper [4] furthermore suggests the use of spin manipulators which generate rotating magnetic fields. Demirel et al. [5] adapted the set-up to a polarimeter experiment using the rotating magnetic field generated by the spin manipulator called the "Mashhoon box". Their results demonstrated a linear dependence of the phase shift from the frequency of rotation.

Their experiment was mainly criticised to address a non-quantum mechanical effect. In a subsequent attempt to clarify this critisism and measure the phase interferometrically, the first interferograms had low contrast due to dephasing between the two sub-beams. The dephasing was induced by interaction with material in the cross-section of the neutron beam due to the geometry of the coil at that time. Furthermore, the Mashhoon box's water cooler, necessary in such an interferometer experiment, leaked and further measurements were impossible.

With the present thesis, a second attempt is prepared by further developing the Mashhoon box. The specifications for the new design were a window for the neutron beam without material and a sudden field transition while the coil still has to be installable in a single crystal neutron interferometer. The magnetic fields of three main coil designs were studied by simulations and by testing them in a neutron polarimeter: a Helmholtz geometry, a miniature of the coil Demirel et al. used, and a grooved coil. The Helmholtz coil has a long field transition and could not be properly operated in the polarimeter. The miniature has wires in the window. Its simulation shows a sudden field change at entry and exit. In the polarimeter, the results of basic spin manipulations with the miniature were good. The grooved coil is a combination of the two other geometries. While the grooves hold the wires on the sides of the window like in the geometry of the miniature, at the entry and exit of the window the wires are wound on top and bottom of the window like in the Helmholtz geometry. The grooved coil prooved to be the best in the polarimeter. With it, the set-up of Demirel et al. and the resulting linear dependence of the coupling phase from the frequency was reproduced. A water cooler for neutron interferometry was designed in adjustment to the new coil geometry.

Kurzfassung

Diese Diplomarbeit beschäftigt sich mit einem Effekt von Rotation auf den Neutronenspin $\vec{S}$. Ein Mittel den Effekt quantenmechanisch zu beschreiben sind geometrische Phasen, deren Studium ein produktives Arbeitsfeld seit ihrer Einführung durch Berry [1] sind. Eine von ihnen, verursacht durch Spin-Rotations-Kopplung, die in einem Hamiltonoperator als $\vec{\Omega} \cdot \vec{S}$ geschrieben wird, wurde von Mashhoon und Co-Autoren in einer Reihe von Artikeln behandelt [2–4]. Sie schlagen darin vor, die Spin-Rotations-Kopplung in einem Interferometer-Experiment mit Neutronen zu isolieren und zu messen. Im letzten derartigen Artikel [4] regen die Autoren auch die Verwendung von Spinmanipulatoren an, die rotierende Magnetfelder erzeugen. Demirel et al. [5] haben den Aufbau zu einem Polarimeter-Experiment adaptiert und das rotierende Feld verwendet, das vom zentralen Spin-Manipulator in Form einer Spule, genannt „Mashhoon-Box“, erzeugt wird. Ihre Ergebnisse zeigen eine lineare Abhängigkeit der Kopplungsphase von der Rotationsfrequenz.

Ihr Experiment wurde vor allem dafür kritisiert, sich mit einem nichtquantenmechanischen Effekt zu befassen. In einem anschließenden Versuch diesen Kritikpunkt zu klären und den Effekt interferometrisch zu messen, hatten die Interferogramme wegen unerwünschter Phasenverschiebungen zwischen den Teilstrahlen geringen Kontrast. Die Phasenverschiebungen waren durch Wechselwirkung mit Material im Querschnitt des Neutronenstrahls induziert, verursacht durch die damalige Spulengeometrie der Mashhoon-Box. Darüber hinaus leckte die Wasserkühlung der Mashhoon-Box, die bei solchen Interferometer-Experimenten nötig wird, und verunmöglichte weitere Messungen.

Mit der vorliegenden Arbeit wurde ein erneuter Versuch vorbereitet, indem die Mashhoon-Box weiterentwickelt wurde. Die Bedingungen für den neuen Entwurf waren ein Fenster für den Neutronenstrahl frei von Material und ein plötzlicher Feldübergang, während die Spule gleichzeitig in einem Interferometer eingebaut werden können muss. Drei unterschiedliche Designs wurden in einem Polarimeter getestet und ihre Felder simuliert: eine Spule mit Helmholtz-Geometrie, eine Miniatur der von Demirel et al. verwendeten und eine gerillte Spule. Die Helmholtz-Spule hat einen langen Feldübergang und konnte nicht geeignet genutzt werden. Die Miniatur hat Drähte im Fenster. Ihre Simulation zeigt einen plötzlichen Feldübergang beim Ein- und Ausgang. Die Resultate von elementaren Spinmanipulationen mit der Miniatur im Polarimeter waren zufriedenstellend. Die gerillte Spule ist eine Kombination der anderen beiden Geometrien. Während die Rillen die Drähte an den Seiten halten wie bei der Miniatur, sind die Drähte an Ein- und Ausgang des Fensters über und unter dem Fenster gewickelt wie bei der Helmholtz-Spule. Die gerillte Spule hat sich im Polarimeter als die beste erwiesen. Mit ihr wurde der Aufbau von Demirel et al. wiederhergestellt und deren Ergebnisse einer linearen Abhängigkeit der Kopplungsphase von der Rotationsfrequenz reproduziert. Eine Wasserkühlung für Neutroneninterferometrie wurde entwickelt, die der neuen Geometrie Rechnung trägt.

Contents

Chapter 1

Introduction

Rotating systems play a substantial role in physics. Every measurement on Earth is executed in the rotating frame of the Earth and the resulting effects have to be known. Also the role of rotations in our understanding of the properties of space itself was and is of great importance: their investigation, besides translations, was a significant factor in the development of our paradigm of relativity, both special and general alike [6, 7]. When Foucault introduced his pendulum in Paris to demonstrate Earth's rotation, it was the first tool to see its classical effects accessible to many people. The Sagnac effect [8] is, in todays view, a manifestation of special relativity in a rotating frame of reference like the effects observed in the more famous Michelson-Morley experiment [9] that deals with translations.

Neutrons can be used to probe effects on their spin, a quantum mechanical property of intrinsic rotation and magnetism. The charge of neutrons is experimentally well confined at zero and electrostatic influences can be excluded. The method of neutron interferometry has been used to demonstate the wave properties of neutrons [10] and has since been adapted in research on quantum contextuality [11], Bell's theorem [12, 13], the effect of a quantum Cheshire Cat [14] and topological phases [15] whose classical analogon, describing the Foucault Pendulum, has since been found in the form of Hannay angles [16].

Dynamical phases describe a present state configuration of a system. Additional topological phases can occur in contrast when the properties of the sytem are also path-dependent. For example, the Sagnac effect is mathematically formulated as coupling between orbital angular momentum $\vec{L}$ and a rotation vector $\vec{\Omega}$ in the Hamiltonian $\hat{H}$ that fulfills the relation

$$\hat{H} \sim \vec{\Omega} \cdot \vec{L}. \tag{1.1}$$

The rotation vector $\vec{\Omega}$ is proportional to the rotation frequency and the area which a particle circles while the direction of the orbital angular momentum $\vec{L}$ is given by the specific motion. Therefore the Sagnac effect is path-dependent and can be described with topological phases. The right-handed expression in Equation (1.1) can be generalised to a total angular momentum term $\vec{\Omega} \cdot \vec{J} = \vec{\Omega} \cdot (\vec{L} + \vec{S})$ with an additional spin term $\vec{S}$. This can be respecified to the case of spin-rotation coupling which leads to a path dependence as well. For neutrons with $S = 1/2$, the path is then the time evolution of the spin on the Bloch sphere. The phenomena of this

$$\vec{\Omega} \cdot \vec{S} \tag{1.2}$$

term are nowadays used regularly, e.g. in nuclear magnetic resonance. A manifest approach demonstrating the effect on single neutrons using the method of neutron interferometry was suggested by Werner and Mashhoon [2]. It predicts a coupling between mechanical rotation and spin. Since

it was revised [3, 4] suggesting the coupling to rotating magnetic fields of spin flippers. Such a spin flipper is called a “Mashhoon box” in this thesis.

An adapted approach using neutron polarimetry has since been executed by Demirel et al. [5]. Their results show the predicted linear dependence between phase shifts of polarograms and the rotation frequency of a magnetic field. However, there has been doubt it even shows a quantum mechanical effect. To meet this critique, an adaptational realisation of the originally proposed interferometrical design has been prepared in this thesis.

Prior to this master thesis, I already completed a project thesis with the same goal [17]. The attempt to produce results in the form of measurements was not successful. The main reason for it was the lack of testing of the water-cooling parts. They leaked and it was not possible to complete the measurements. Now, in this master thesis, I revised and reworked the concept of the Mashhoon box in order to provide stable measurements of better quality. The actual measurements do not form part of this thesis.

In chapter 2, the theoretical concepts are discussed briefly. Chapter 3 explains the mechanisms of the devices used carrying out the experiments. The main executional effort of this thesis is documented in chapters 4 and 5. The former describes the developmental process that was needed. The latter one contains the tests to reproduce the results of Demirel et al. in polarimetry with a Mashhoon box compatible to interferometry.

Chapter 2

Theoretical and Experimental Background of the Study

The topic of this thesis, spin-rotation coupling, is brought in this chapter into the broader context of classical rotations and quantum mechanics. Then the more specific experimental techniques are explained briefly.

2.1 Rotations in Classical Physics

It has taken a vast intellectual effort to reach our present-day understanding of nature. The most determinative regularity for humankind has always been the sequence of day and night. Many cultures interpreted them in a mythological or religous context – including the seasons, with their importance to agriculture. Knowledge concerning those phenomena was and is a powerful tool.

For the past few hundred years, the common basis for new knowledge has been the scientific method. Using its principles, our society has been able to abstract basic properties and, based on them, more complex features of nature. The conclusions of this approach now allow us to think of the above periodicities as results of the rotation of Earth around its own axis and Earth around the Sun. A few examples of formative experiments in the research of rotations in science are recapitulated next. The basic question concerning rotations, i.e. as to what reference they rotate to, is still open to discussion.

A basic description of classical rotations can be found in every standard textbook on mechanics such as source [18].

2.1.1 Galilei's Pendulum

It is said that one day, when Galileo Galilei was sitting in a church, he observed the candelabras hanging on the ceiling swinging all with the same frequency. However, he studied pendulums and identified a connection between pendulum suspention length l and oscillation period T: a longer suspension causes a longer period (formula below). He also claimed the independence of the frequency from the angle of displacement ϕ from the position of rest. This principle was consequently used in mechanical clocks. We nowadays describe the ideal pendulum with the

differential equation of motion as

$$\begin{aligned} l\ddot{\phi} &= -\,g\sin\phi \\ \Rightarrow 0 &= \ddot{\phi} + \frac{g}{l}\sin\phi \\ |\phi \to 0| \Rightarrow 0 &= \ddot{\phi} + \frac{g}{l}\phi \end{aligned} \tag{2.1}$$

with Earth's acceleration of gravitation $g = 9.81\,\mathrm{m/s^2}$. The ansatz $\phi = \phi_0 \sin(\omega t + \varphi)$ with arbitrary phase φ and $\omega = \sqrt{\frac{g}{l}}$ solves the last of Equations (2.1). Angular velocity ω, frequency f and period are connected via $\frac{\omega}{2\pi} = f = \frac{1}{T}$.

The Galileian notion of constant frequency for all displacements ϕ_0 is in this treatment an approximation for small angles. It is known as "Hooke's law" and equivalent to a quadratic potential, the main assumption of harmonic oscillators. Of course, the oscillation is not a pure rotation but can be abstracted from it through trigonometric functions. Technology has improved since then and multiple generations of clock mechanisms were developed. But in today's quantum mechanics this approximation can still describe some basic phenomena: for the case of a system with a continuous potential featuring a global minimum potential energy, a ground states arises. Because the potential can be locally approximated by a harmonic term in the minimum, the pendulum is still helpful to describe many properties of such ground states.

2.1.2 Newton's Bucket Gedankenexperiment

The paradigm change in celestial mechanics from Aristotle to Copernicus took as long as it did because we do not recognise the effects of rotations in our daily lives on objects in our sphere of influence and can regard Earth for these purposes as static. When the notion of Earth as revolving around the Sun and rotating on its own axis became widely accepted, the properties of rotations and reference frames began to be researched more deeply.

Newton describes the situation of a bucket that is filled with water, the shape of whose surface on top does react significantly to forces. He argues that the surface is even for all whom we now call "inertial observers" if the bucket is not rotated. If the bucket is rotated, the water is accelerated due to friction on the walls and the surface becomes a paraboloid of revolution. An observer located on the surface and rotating with it can distinguish the curved stable surface from the flat one and can, like the inertial observer, also conclude his system is rotating. One can deduce from this that a test for one's own rotation is always possible basen on this principle. The scenario reflects Newton's notion of absolute space [6]. Although he formulated Galileian invariance as fundamental pillar for all developments on classical inertial frames, he still assumed a distinguished system in principle non-identifiable through physical laws.

An adaptation of this model is Mach's bucket: His notion of space is based on the relativity of inertial frames and neglects absolute space [7]. In contrast all dynamics should be referenced to the fixed stars that constitute an approximately inertial system. If the bucket is rotated against this system, the paraboloid shape will develop, too. Furthermore, he presents the situation that everything, the entire universe as the reference for rotations, is rotating around the bucket. Then the drag of all fixed stars on space itself would induce bucket and liquid to rotate.

Both perceptions, Newton's and Mach's, have fundamental weaknesses from today's perspective: The concept of Newtonian absolute space has been replaced by local inertial frames in general relativity that are always equivalent to the assumption of an acceleration towards a centre of gravity on geodesics. In Mach's interpretation, the situations of only the rotated bucket and fixed environment and vice versa are physically indistinguishable. Also the mechanism of how the distant stars induce such local observations is still missing and is a current object of research in general relativity.

2.1.3 Foucault Pendulum

An important source for this section was reference [19].

As a synthesis of the previous two sections, a pendulum can be used to measure the rotation of a system: The mass of a pendulum bob is equal to its inertia. If only a displacement initially causes a pendulum to oscillate in a certain plane, it will only leave this plane due to another external force. A crucial experimental feature is a suspension with minimised transfer of angular momenta. For demonstrating of the rotation of Earth around its axis, as Foucault did in 1851, the geographic lattitude ϕ is relevant: If a pendulum oscillates on the poles and no additional force is applied, the pendulum will remain in that plane while Earth is rotating below it with angular velocity Ω; the rotation vector $\vec{\Omega}$ and the vector $\vec{n}$ normal to Earth's surface fulfill the relation $\vec{\Omega} \parallel \vec{n}$. In the rotating frame, an exchange of momentum occurs.

For an observer rotating with Earth, the trajectory of the pendulum composes a rose (see Fig. 2.1). Around the turning points of the pendulum bob, this is easily understood: Before the turning point, the pendulum bob has some displacement. Until the same displacement is reached again after the maximum displacement, Earth rotated and the two displacements do not have the same orientation in the rotating system. They are only conneted by the trajectory that takes the form of a rose. Despite this fact, an approximate measurement of the oscillation direction is always possible for the given problem also in the rotating system.

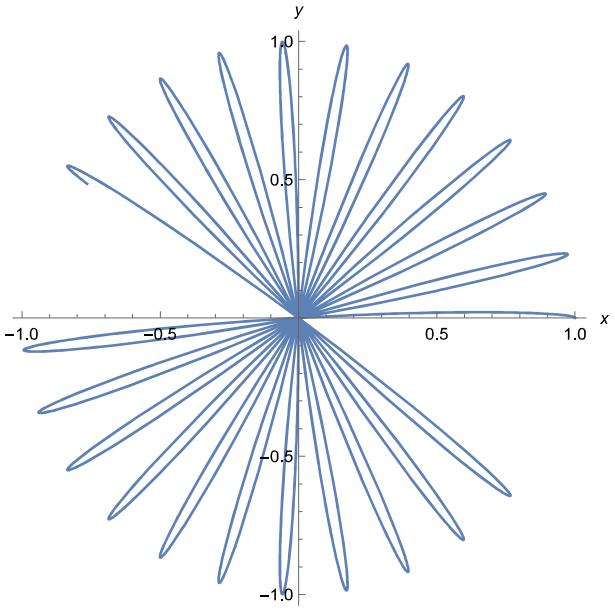

Figure 2.1: The path of the Foucault Pendulum in the rotating system composes a rose.

On the equator, two possible planes of oscillation arise: either in the equatorial plane or a longitudinal one. In the first case, the orientation of the oscillation plane to Earth is maintained. In the latter case the translation of the plane induces a tilt in the rotating system. As an extreme overrepresentation, if Earth rotated by $\pi/2$, the oscillation plane would be horizontal. This situation will, of course, not emerge. But the present continuous tilt until this extreme case can be regarded as constant stimulus perpendicular to the initial swinging direction. Both resulting displacements can be regarded as independently superposing. The second, superposed oscillation caused is small in comparison and only accentuates the rose pattern that is already present for the rotating observer. In both cases on the equator, the relation $\vec{\Omega} \perp \vec{n}$ holds. In the rotating frame of reference the oscillation plane distinguished will not change.

In the lattitudes in between, as already implied, the coupling is an intermediate case proportional to the ratio $\vec{\Omega} \cdot \vec{n}$. The Foucault pendulum changes its oscillation plane in our accelerated system of observation with a frequency of

$$f = \frac{\Omega \sin \phi}{2\pi} \tag{2.2}$$

as an indirect measurement of Earth's rotation.

Generally, the same method could measure Earth's rotation around the Sun and our solar system's in the Milky Way and so on. As the regimes become bigger, the effects become only apparent with longer time. The necessary stabilisation over those periods is not possible with this experimental type due to friction.

2.1.4 Sagnac Effect

Another example used for measuring rotations is the Sagnac interferometer [8]. The whole apparatus (see Fig. 2.2) stands on a table rotating to a system regarded as an inertial frame. A source emits light in a specific direction. This beam enters the interferometer via a half-silvered mirror that splits the waves' amplitudes. One half is transmitted while the other half is reflected. The following beam paths classify the Sagnac interferometer as common path interferometer: Both beams are reflected by the same mirrors to a cyclic revolution with opposite senses of rotation back to the half-silvered mirror. This last mirroring causes both beams to interfere with same directions of propagation again. Because the half-silvered mirror splits both beams also at the second encounter, there are two such directions: towards the source and perpendicular, away from the mirror towards a detector. The path lengths must be aligned the same very accurately to generate the expected maximum on the optical axis towards the detector in the stationary case of $\Omega = 0$.

With rotation ($\Omega \neq 0$), the effects can be described with special relativity (SR): for the inertial observer, the speed of light in all directions is the same. While one beam revolves through the interferometer against the sense of rotation and traverses a shorter length back to the half-silvered mirror than in the static case, the other beam traverses in the same sense of the rotation direction and has a longer path to take. The result with the mathematical description of waves is a phase shift φ between the two sub-beams at the second encounter of the half-silvered mirror. It can effect to constructive ($\Delta\varphi = 2\pi n$) or destructive ($\Delta\varphi = \pi n$) interference in the optical axis towards the detector. The phase depends on the orbital angular velocity and the area A the beams are enclosing as the relative phase is given by

$$\Delta\varphi = \frac{4}{c\lambda}\vec{\Omega} \cdot \vec{A} = 2 \cdot \frac{1}{\hbar}\vec{\Omega} \cdot \vec{L}\, t \tag{2.3}$$

which can be regarded as coupling of orbital angular momentum and rotation.

Sagnac himself considered his experimental results as proof of the ether, the medium of light expansion, that is dragged with the apparatus and modifies the two speeds of light. This consideration can predict the same results as SR that is nowadays considered the prefered model, as it does not require the assumption of an unobservable ether.

2.2 Spin of Neutrons

The total angular momentum $\vec{J}$ of some particle can be split according to $\vec{J} = \vec{L} + \vec{S}$ where the spin $\vec{S}$ is the intrinsic part of the total angular momentum that is independent of the particle's state of motion. All three, $\vec{J}$, $\vec{L}$ and $\vec{S}$, are properties quantised in units of $\hbar$, i.e. Planck's

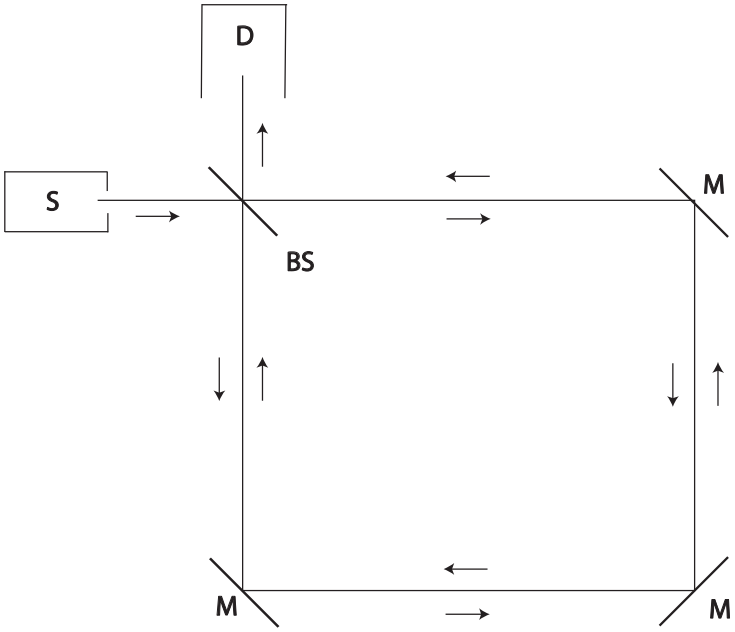

Figure 2.2: Sketch of the principle of a Sagnac interferometer with light source (S), a beam splitter (BS), an interferometer with three further mirrors (M) and a detector (D). Arrows mark the propagation directions of the beams. The whole apparatus can be rotated around an axis perpendicular to the image plane.

constant divided by 2π. Each particle or quasiparticle can be assigned with a value of its spin. For neutrons the spin quantum number is $|\vec{S}| = S = 1/2$. This classifies it as a fermion because of its half-integral spin value. Another quantum number m_S describes the orientation of the spin along a certain chosen axis. Since

$$m_s = \{-S, -S+1, ..., S-1, S\}\,, \tag{2.4}$$

the neutron spin orientation has only two possible values $m_s = \{-1/2, 1/2\}$ which can be considered a simple two-level system.

Although we cannot assign the spin to any spatial movement in classical physics, it shares the rotational property with the orbital angular momentum. This mechanical property of the particle corresponds to an electromagnetic one: the magnetic moment of the neutron $\vec{\mu}$. Even though the neutron has no electric charge, as its name suggests, it has electromagnetic features and can interact with magnetic fields. This is evidence for an inner structure of the neutron. It is now considered to comprise of three quarks, one up and two down, and a complex system of gauge particles, mainly gluons (see for example [20]).

However, the neutron can for the purposes of this thesis be generally assumed to be an elementary Dirac fermion that fulfills

$$\vec{\mu} = \mu\vec{\sigma} = \gamma\vec{S} = g\frac{\mu_p}{\hbar}\vec{S} = g\frac{e}{2m_p}\vec{S} \tag{2.5}$$

with value of the neutron's magnetic moment $\mu = -9.662\,364\,723 \cdot 10^{-27}\,\mathrm{J/T}$, the gyromagnetic ratio γ, the protons magnetic moment μ_p, the g-factor for the neutron $g = -3.82608545$, that gives some particles magnetic moment in units of the proton's, the elementary charge $e = 1.602 \cdot 10^{-19}\,\mathrm{C}$ and the proton's mass $m_p = 1.6726 \cdot 10^{-27}\,\mathrm{kg}$. With the negative value of g, magnetic moment and spin have opposite directions for neutrons, while g is positive for protons. The mathematical description of the spin in an environmental magnetic field with the Schrödinger equation of motion

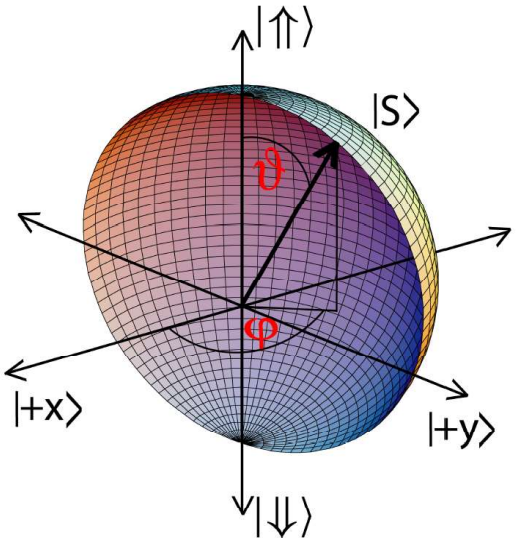

Figure 2.3: Representation of the spin state on the Bloch sphere with the angles ϑ and φ as in Equation 2.7.

is given by

$$\hat{H}\,|\psi\rangle = i\hbar\partial_t\,|\psi\rangle \tag{2.6}$$

with the abstract wavefunction $|\psi\rangle$ which involves a Hamiltonian $H_{mag} = -\vec{\mu}\cdot\vec{B}$ that has two eigenstates parallel and antiparallel to the magnetic field. In Hilbert space of states $\mathcal{H}$, they are written as $|\uparrow\rangle$ (up-spin) and $|\downarrow\rangle$ (down-spin). Each state is customarily expressed as a superposition

$$|S\rangle = \cos(\vartheta/2)\,|\uparrow\rangle + e^{i\varphi}\sin(\vartheta/2)\,|\downarrow\rangle \tag{2.7}$$

of these eigenstates. This spin part can be separated in the total wavefunction $|\psi\rangle = |\phi\rangle\,|S\rangle$ from the spatial part $|\phi\rangle$. For a geometrical representation of complex superpositions of the two eigenstates in their two-level system, the Bloch sphere can be used (see Fig. 2.3). The polar angle ϑ defines the portions of up and downspin to a state. The poles of the Bloch sphere represent states identical to one of the eigenstates. The remaining surface represents states with portions of both eigenstates. The smaller the polar angle ϑ on the sphere, the larger the portion of the up-spin component becomes. The azimutal angle φ defines the relative phase between the two eigenstates. The polarisation vector $\vec{P}$ is the expectation value of the spin orientation calculated as

$$\vec{P} = \langle\vec{\sigma}\rangle = \langle\psi|\,\vec{\sigma}\,|\psi\rangle \tag{2.8}$$

where the vector $\vec{\sigma}$ comprises of the Pauli matrices

$$\vec{\sigma} = \begin{pmatrix} \hat{\sigma}_x \\ \hat{\sigma}_y \\ \hat{\sigma}_z \end{pmatrix} \tag{2.9}$$

with

$$\hat{\sigma}_x = \begin{pmatrix} 0 & 1 \\ 1 & 0 \end{pmatrix}, \quad \hat{\sigma}_y = \begin{pmatrix} 0 & -i \\ i & 0 \end{pmatrix}, \quad \hat{\sigma}_z = \begin{pmatrix} 1 & 0 \\ 0 & -1 \end{pmatrix} \tag{2.10}$$

in the z-eigenbasis. The expectation value of the spin of a superpostion follows the probabilistic description

$$P_\uparrow = |\langle\uparrow|\,|\psi\rangle\,|^2 = \cos^2(\vartheta/2), \tag{2.11}$$

$$P_{\downarrow} = |\langle\downarrow|\,|\psi\rangle\,|^2 = \sin^2(\vartheta/2), \tag{2.12}$$

$$P_{\uparrow} + P_{\downarrow} = 1. \tag{2.13}$$

The azimutal angle φ affects measurements of spin components in other directions $P_{\pm x}$, $P_{\pm y}$. A perfect polarisation is described with a polarisation vector with absolute value of 1. A depolarised ensemble is represented by a polarisation vector with smaller absulute value that does not reach the surface of the sphere. A single wave function can then not describe all physical properties of a system.

2.3 Time Evolution and Different Kinds of Phases

The expectation value of the spin orientation is represented by the polarisation vector $\vec{P}$ where $\vec{P}(t) = \langle\vec{\sigma}\rangle(t) = \langle\psi(t)|\,\vec{\sigma}\,|\psi(t)\rangle$. Its time evolution is

$$\begin{aligned}\frac{d\vec{P}}{dt} &= \frac{d}{dt}\left(\langle\psi(t)|\,\vec{\sigma}\,|\psi(t)\rangle\right)\\ &= \left(\frac{d}{dt}\langle\psi(t)|\right)\vec{\sigma}\,|\psi(t)\rangle + \langle\psi(t)|\left(\frac{d\vec{\sigma}}{dt}\right)|\psi(t)\rangle + \langle\psi(t)|\,\vec{\sigma}\left(\frac{d}{dt}\,|\psi(t)\rangle\right) + \langle\psi(t)|\,[\frac{d}{dt},\vec{\sigma}]\,|\psi(t)\rangle\\ &= \langle\frac{d\vec{\sigma}}{dt}\rangle - \frac{i}{\hbar}\langle[\vec{\sigma},\hat{H}]\rangle.\end{aligned} \tag{2.14}$$

In Schrödinger notation, the operators are constant and the first term vanishes. For a system in a magnetic field, where $H = -\vec{\mu}\cdot\vec{B}$, it follows that

$$\frac{d\vec{P}}{dt} = \frac{i\mu}{\hbar}[\vec{\sigma},\vec{\sigma}\cdot\vec{B}] \tag{2.15}$$

The commutation relations for angular momenta

$$[\hat{\sigma}_i,\hat{\sigma}_j] = 2i\epsilon_{ijk}\hat{\sigma}_k \tag{2.16}$$

lead to

$$\frac{d\vec{P}}{dt} = \gamma\vec{P}\times\vec{B}. \tag{2.17}$$

This is also the relation for a magnetic moment in a magnetic field in classical mechanics. For a static field, the spin orientation evolves on a circle around the field direction.

A related but more general approach exists. It allows the introduction of the Berry phase that is essential for this thesis. A helpful source for this section was the detailed overview of K. Durstberger [21], which itself follows the original paper by Berry [1].

The time evolution of a spin state can change the polar angle ϑ and azimutal angle φ on the Bloch sphere. These are phases that rely only on the present state and which are also described by Equation (2.17) in the case of a perfect degree of polarisation. The Schrödinger equation of a system with time dependence described by the Hamilton operator $\hat{H}$ and a parametrisation $R(t)$ is

$$\hat{H}(R(t))\,|\psi(t)\rangle = i\hbar\frac{d}{dt}\,|\psi(t)\rangle\,. \tag{2.18}$$

The eigenvalue equation for each eigenstate $|\psi_n(R(t))\rangle$ is

$$\hat{H}(R(t))\,|\psi_n(R(t))\rangle = E_n(R(t))\,|\psi_n(R(t))\rangle\,. \tag{2.19}$$

If we consider an eigenstate as the initial state of the system,

$$|\psi(0)\rangle = |\psi_n(R(0))\rangle\,, \tag{2.20}$$

any changes in a non-degenerate system will only affect the state, and no transitions will occur. The time-dependent solution of the wavefunction of the system is then

$$|\psi(t)\rangle = e^{i\delta_n(t)} |\psi_n(R(0))\rangle , \tag{2.21}$$

where the phase δ_n is written as

$$\delta(t) = \epsilon(t) + \gamma(t). \tag{2.22}$$

The first term on the right hand side is the dynamical phase

$$\epsilon(t) = -\frac{1}{\hbar}\int_0^t E_n(t')dt'. \tag{2.23}$$

The expression for the remaining phase γ is derived by solving the Schrödinger equation with both ansatze (2.21) and (2.22) which gives

$$\frac{d}{dt}(\gamma(t) + \epsilon(t)) = i \langle\psi_n(R(t))| \frac{d}{dt} |\psi(R(t))\rangle - \frac{1}{\hbar} E_n(R(t)). \tag{2.24}$$

Besides the time derivation of the already presented ϵ, the remaining expression reads

$$\begin{aligned} \frac{d\gamma(t)}{dt} &= i \langle\psi_n(R(t))| \frac{d}{dt} |\psi_n(R(t))\rangle \\ &= i \langle\psi_n(R(t))| \frac{d}{dR} |\psi_n(R(t))\rangle \frac{dR}{dt} \\ \Rightarrow \gamma(t) &= i \int_{R_i}^{R_f} \langle\psi_n(R(t))| \frac{d}{dR} |\psi_n(R(t))\rangle \, dR. \end{aligned} \tag{2.25}$$

The Berry phase is dependent on the path and is therefore also called “geometric phase”. A classical geometric analogue was found after the quantum mechanical one that describes, e.g., the Foucault pendulum in terms of Hannay angles.

As Berry was already considering interferometrical measurements to confirm this phase, he assumed a cyclic revolution of the state in one interferometer arm that could be compared with an unaffected one in the other arm (see Section 3.6.1). Neither the cyclic case nor adiabaticity are necessary conditions for the derivation. These restrictions have since been lifted in generalisations by Samuel and Bhandari [22], and Aharanov and Anandan [23] respectively. But as will be shown in the next section, the measurements of this thesis nonetheless use the cyclic case. The non-adiabatic case is essential for all real measurements.

2.4 Spin-Rotation Coupling

Naturally expanding the Sagnac effect from $\vec{\Omega} \cdot \vec{L}$ to all kinds of angular momenta $\vec{J}$, an additional term $\vec{\Omega} \cdot \vec{S}$ should arise. The neutrons used in the experiment have velocities v of approx. 2 km/s (see Table 3.1). Compared to c, the speed of light, $v \ll c$. This means the non-relativistic approximation suffices to explain the measured effects. The following derivation of the spin-rotation coupling is, in principle, adopted from the sources [5, 24] and the non-relativistic limit of derivations such as [25, 26].

The rotating magnetic field with arbitrary initial orientation is

$$\vec{B} = B_0 \begin{pmatrix} \cos(\Omega t + \beta) \\ 0 \\ \sin(\Omega t + \beta) \end{pmatrix}. \tag{2.26}$$

The interaction is considered present from time $t = 0$ with a sudden process of turning on and off. This will be important later in the design of the coil generating the magnetic field (see Sections

4.1 and 4.2). The phase β determines the angle in the x-z-plane between the field and a spin orientation. Any spin orientation can be represented by a superposition of y-spins with relative phase for which the phase shift β is insignificant. The effects of the rotating field can, therefore, be reduced to y-spins. The spin manipulations of the experiment are constrained to cyclic evolutions of these y-spins, as will be explained with Equation (2.41). In this case, the phase shift β is irrelevant and chosen zero.

The one-dimensional Pauli-Schrödinger equation for a spin-1/2 particle moving in y-direction is

$$\hat{H}\psi(y,t) = \left(-\frac{\hbar^2}{2m}\vec{\nabla}_y^2 - \mu\vec{\sigma}\cdot\vec{B}(y,t)\right)\psi(y,t) = i\hbar\frac{\partial}{\partial t}\psi(y,t) \tag{2.27}$$

with the neutron's mass $m = 1.6749 \cdot 10^{-27}\,\mathrm{kg}$. Separating spatial and time components with the ansatz

$$\psi(y,t) = \phi(y)\chi(t) = \phi(y)\begin{pmatrix}\chi_1(t)\\ \chi_2(t)\end{pmatrix}, \tag{2.28}$$

where $\chi(t)$ includes the two-level system of spin eigenstates, gives the two differential equations

$$-\frac{\hbar^2}{2m}\frac{\partial_y^2\phi(y)}{\phi(y)} = i\hbar\frac{\partial_t\chi(t)}{\chi(t)} + \mu\vec{\sigma}\cdot\vec{B} = \kappa. \tag{2.29}$$

The number κ is equal to the left side, the kinetic energy operator eigenvalue. Applied to a wavefunction, this operator results in the expression $\frac{\hbar^2k^2}{2m}$ with the wave number k. The spatial part can then be solved by the normalised stationary wave oriented with the rotation axis to

$$\phi(y) = \frac{1}{\sqrt{2\pi}}e^{iky}. \tag{2.30}$$

In the time dependent part, the transformation

$$\chi(t) = e^{-i\frac{\hbar k^2}{2m}t}\xi(t) \tag{2.31}$$

leads to the one-dimensional differential equation

$$\left[i\hbar\partial_t + \mu B_0(\hat{\sigma}_x\cos\Omega t + \hat{\sigma}_z\sin\Omega t)\right]\xi(t) = 0. \tag{2.32}$$

The last two exponentials of Equations (2.30) and (2.31) together compose a plain wave with wave number k. To describe a neutron, a wave packet with a distribution of wave numbers $a(k)$ is used that in one dimension is characterised by a wave function $\zeta(x,t)$. This wave function is written as

$$\zeta(x,t) = \int_{k=0}^{\infty} a(k)e^{i(kx-\omega(k)t)}\mathrm{d}k. \tag{2.33}$$

However, the below result of the spin-rotation coupling phase is independent of the wave number. For the calculation of the phase, the restriction to a single wave number is sufficient.

Another transformation substituted in Equation (2.32) with a spin-rotation like term in the ansatz

$$\xi(t) = e^{i\frac{\vec{\Omega}\cdot\vec{S}_y}{\hbar}t}\xi_r(t) = e^{i\frac{\Omega t}{2}\hat{\sigma}_y}\xi_r(t) \tag{2.34}$$

represents the change into the reference system rotating with the magnetic field. With the relation

$$e^{-i\frac{\Omega t}{2}\hat{\sigma}_y}\left(\hat{\sigma}_x\cos\Omega t + \hat{\sigma}_z\sin\Omega t\right)e^{i\frac{\Omega t}{2}\hat{\sigma}_y} = \hat{\sigma}_x \tag{2.35}$$

(see appendix A.1 for derivation) this leads to the integrable equation

$$i\hbar\partial_t\xi_r(t) = \left(\frac{\hbar\Omega}{2}\hat{\sigma}_y - \mu B_0\hat{\sigma}_x\right)\xi_r(t) \tag{2.36}$$

resulting in

$$\xi_r(t) = e^{-i\left(\frac{\Omega}{2}\hat{\sigma}_y - \frac{\mu B_0}{\hbar}\hat{\sigma}_x\right)t}\xi_r(0) = e^{-i\frac{\vec{\alpha}\cdot\vec{\sigma}}{2}}\xi_r(0). \tag{2.37}$$

With the Larmor precession angular velocity $\omega_0 = -2\mu B_0/\hbar$, the rotation vector $\vec{\alpha}$ with absolute value α and direction $\hat{\alpha}$ reads

$$\vec{\alpha} = \alpha\hat{\alpha} = \begin{pmatrix} \omega_0 t \\ \Omega t \\ 0 \end{pmatrix}. \tag{2.38}$$

In this last vector the x-component is a Larmor precession around the rotating field that rotates the spin component in the plane normal to the field. Connected to it is a second spin-rotation coupling term in the y-component. This part rotates the spin around the for both systems common y-axis. The combination of the two components leads to an intricate trajectory on the Bloch sphere in the non-rotating frame of reference (see trajectories constrained by Equation (2.42) with $n = 1$ in Fig. 2.4). The complete wave function that solves the initial Schrödinger equation follows as

$$\psi(y,t) = \phi(y)\xi(t) = \frac{1}{\sqrt{2\pi}}e^{iky}e^{-i\frac{\hbar k^2}{2m}t}e^{i\frac{\Omega t}{2}\hat{\sigma}_y}e^{-i\frac{\vec{\alpha}\cdot\vec{\sigma}}{2}}\xi_r(0). \tag{2.39}$$

The expression Ωt is included in each of the last two exponentials with opposing signs. However, due to the Baker-Campbell-Hausdorff formula, the latter operator cannot be split in operators only dependent on $\hat{\sigma}_x$ and $\hat{\sigma}_y$ and a simplification is not possible. The latter operator can however (and the purpose of this will soon be made clear) be transformed into the shape $-\vec{\mu}\cdot\vec{B}$ of the Hamiltonian of a magnetic moment in a magnetic field as

$$\alpha = t\sqrt{\omega_0^2 + \Omega^2} = |\gamma|t\sqrt{B_0^2 + \left(\frac{\Omega}{\gamma}\right)^2} = |\gamma|tB_{\text{eff}}. \tag{2.40}$$

This form allows to control the phase of the last exponential with only the effective field B_{eff}. To single out the spin-rotation coupling of the second unitary operator in Equation (2.39), the last unitary operator must have identity character:

$$\pm\,\mathbb{1} = e^{-i\frac{\vec{\alpha}\cdot\vec{\sigma}}{2}} = \mathbb{1}\cos(\frac{\alpha}{2}) - i\hat{\alpha}\cdot\vec{\sigma}\sin(\frac{\alpha}{2}). \tag{2.41}$$

(See appendix A for a prove of this relation.) It follows that

$$2\pi n = \alpha = |\gamma|tB_{\text{eff}}. \tag{2.42}$$

Such a phase of $\alpha = 2\pi n$ corresponds to the cyclic trajectory originally proposed by Berry. The adaptation of the field amplitude to the frequency yields

$$B_0(\Omega) = \frac{1}{|\gamma|}\sqrt{\left(\frac{2\pi n}{t}\right)^2 - \Omega^2}. \tag{2.43}$$

The ampliutde decreses with rising frequency $f = \frac{\Omega}{2\pi}$. When this condition is fulfilled, an initial spin state $|\pm y\rangle$, collinear to the axis of rotation, gains only a phase proportional to the frequency of the field written as

$$\vec{S}\cdot\vec{\Omega}. \tag{2.44}$$

This last expression has to be integrated over time to calculate the absolute value of the phase (in this time-independent case multiplied with the time period). For a spin manipulating coil, the time t is set to the time T of exposure to the magnetic field (see also the adjustment in Section 5.3).

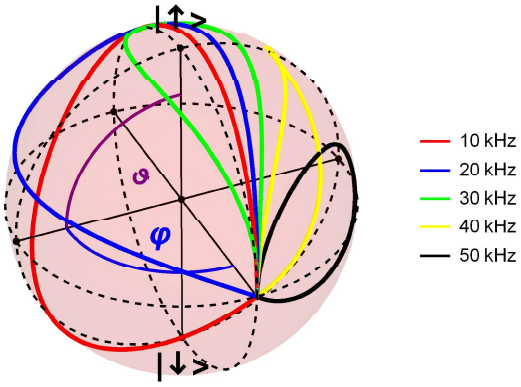

Figure 2.4: Time evolution of the spin orientation on cyclic paths with different rotation frequencies of the magentic field in the case of Equation (2.42) and $n = 1$. The initial state is collinear to the rotation vector. At $t = 0$, the direction of propagation of the spin orientation is the same for all frequencies (upward). With increasing time, the field directions diverge from each other and at the end of the interaction with the magnetic field , $t = T$, the spin states converge from different directions. The evolution path for the lowest frequency is closest to the rotation on a great circle with a static field.

2.5 Concepts of Relevant Experimental Techniques

2.5.1 Neutron Interferometry

If phases occur, what method is used to confirm them? A phase itself cannot be measured by recording intensities and a global phase does not change any experimental outcome. But in the interference of two states in which one of them has an additional phase, this phase can have an explicit effect on measured values. A schematically simple approach is to spatially split a beam of a selected state into two halves (see Fig. 2.5). One half can be the subject to an interaction in question which induces a phase shift $\Delta\chi$. The other half takes another path where this interaction is not present. Both paths, consequently also called arms or sub-beams, are then brought back together coherently. This is the principle of a Mach-Zehnder type interferometer. The two beams emerging from the interferometer, O and H-beam, are detected. The O-beam is only shifted to the incident beam while the H-beam is refracted with respect to the incident beam. Depending on the phase shift $\Delta\chi$, the intensities in the two detected beams are changed. A more detailed overview of neutron interferometry is given in Section 3.6.1.

2.5.2 Neutron Polarimetry

Instead of spatially separating the beams, one can also use the fact that perpendicular spin states (i.e. antiparallel spin orientations) gain in the time evolution phases with opposing signs in an interaction whose Hamiltonian has them as eigenstates. As basis of the further argumentation, a superposition of equal portions of up and down-spin is considered. It is only unambiguous with a fixed relative phase. An additional relative phase changes the longitude on the Bloch sphere. With an interaction, including a spin operator present, both states gather phases that sum up to a doubled additional relative phase. A measurement of the polarisation in either x or y-direction will then be affected by the relative phase. An experimental effect can be divided by 2 if one wants to know how big it is for a single spin state.

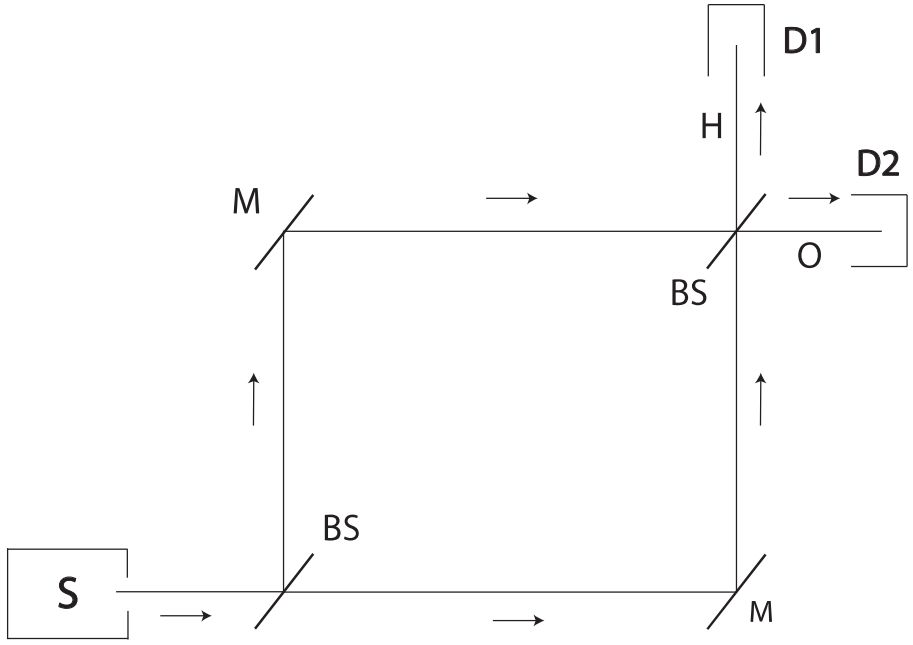

Figure 2.5: Principle of a Mach-Zehnder interferometer. A source (S) emits a beam which is split by a beam splitter (BS) in two paths. Mirrors (M) reflect the sub-beams which interfere behind another beam splitter. Detectors (D1 and D2) measure the intensity of the two beams (O and H) behind the interferometer. Arrows mark the propagation directions of the beams.

This is the principle of another common path interferometer, as in the Sagnac experiment, and the experimental method of this thesis. A more detailed overview of neutron polarimetry is given in Section 3.6.2.

2.6 Spin-Rotation Coupling in Neutron Interferometry

It is the goal in the projected measurements with polarised interferometry to induce and measure a phase shift originating from spin-rotation coupling to confirm the theoretically predicted linearity of the phase shift.

The earliest proposal, to my knwledge, for an experiment that tests for spin-rotation coupling came from Samuel A. Werner published by Mashhoon [2]. He describes a mechanically rotating set-up (interferometer, spin manipulators and detectors) in which neutrons with the same spin orientation as the rotation vector are split on two different paths in the interferometer. In one interferometer arm the spin is flipped after the separation and before being recombined. The phases induced in the single arms are thus added to a redoubled relative phase $\Delta\chi$. Since $\Delta\chi$ is proportional to the time of traversal through the rotating interferometer and the rotation frequency, the effect is very small for thermal neutrons, typical measures of perfect crystal interferometers, and possible mechanical rotation frequencies.

A first tribute to those circumstances was, in another suggestion for an experiment [3], to use spin flippers in each arm (see Fig. 2.6). They ought to perform both a π-flip while one of them is rotated mechanically. This smaller device might be rotated with higher frequency. For a π-flip the interference in the O-beam is time dependent and time-resolved detection is necessary. The next change in concept regarding applicability was to also contemplate the equivalence of a rotating coil to a rotating magnetic field [4]. With two coils generating perpendicular fields, much higher frequencies are accessible electromagnetically compared to mechanical rotation.

The method used in the planned measurements will be to use a spin flipper in only one arm that induces a 2π-flip with a rotating field that is expected to induce an additional phase. Similarly oriented spin states are superposed at the last interferometer blade. Whether a spin-rotation coupling phase changes the interference of the perpendicular path states in the beams leaving the interferometer compared to a static field, will be observed.

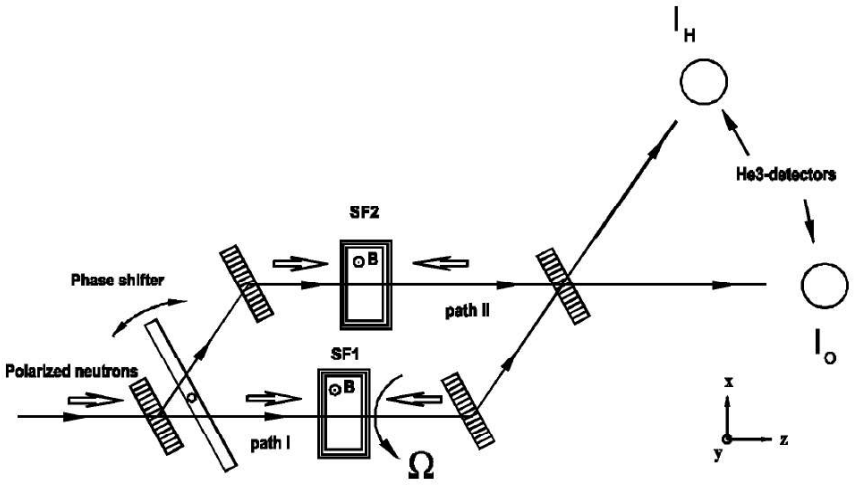

Figure 2.6: Proposed set-up by Mashhoon in his 2006 paper [4]. A neutron beam polarised in beam direction is split in two in a neutron interferometer. In both arms a π-spin flip is done. The bottom spin flipper has a rotating magnetic field, realised either by rotating the spin manipulator mechanically or supplying its coils with oscillating currents. The intensity counted by the detector is time-dependent with the period of the rotation. A phase shifter can be tilted to generate interferograms.

2.7 Previous Polarimeter Experiment by Demirel et al.

The set-up implemented by Demirel et al. (see Fig. 2.7) adapted the last proposal of Mashhoon. Instead of using the sophisticated method of neutron interferometry, two spin states are superposed in a polarimeter. The emerging effect is doubled, because no static reference state is used but both interact with the magnetic field with opposing phases. The authors also changed the value of α from π to 2π, resulting in stationary interference with no necessity for time-resolved measurements. The resulting polarograms are dependent on the frequency of the rotating field (see Fig. 2.8). They found a linear dependence, as expected, of the relative phase shift from the rotation frequency (see Fig. 2.9).

However, the experiment was criticised. In the course of the peer-review process, it was argued by one referee that the presented results did not have explicitly quantum mechanical origin and could be predicted classically as well. As declared earlier, the purpose of this thesis is to prepare the spin manipulator called Mashhoon box for the neutron interferometry experiment that should, with a positiv effect, produce results that can be described only quantum mechanically. Nevertheless, the goal of this thesis was to reproduce the results of Demirel et al. in the same polarimetric set-up with a Mashhoon box applicable for neutron interferometry.

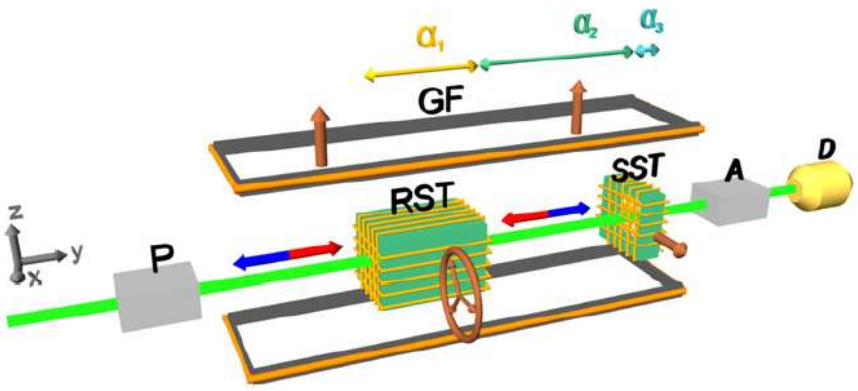

Figure 2.7: The set-up of Demirel et al. [5]:"Actual neutron polarimeter set-up with a total length of roughly 3 m. Blue and red arrows indicate spin states. Polarizing supermirror (P); guide field (GF); rotating spin turner (RST); static spin turner (SST); analyzing supermirror (A); detector (D). The GF is compensated inside the RST and SST."

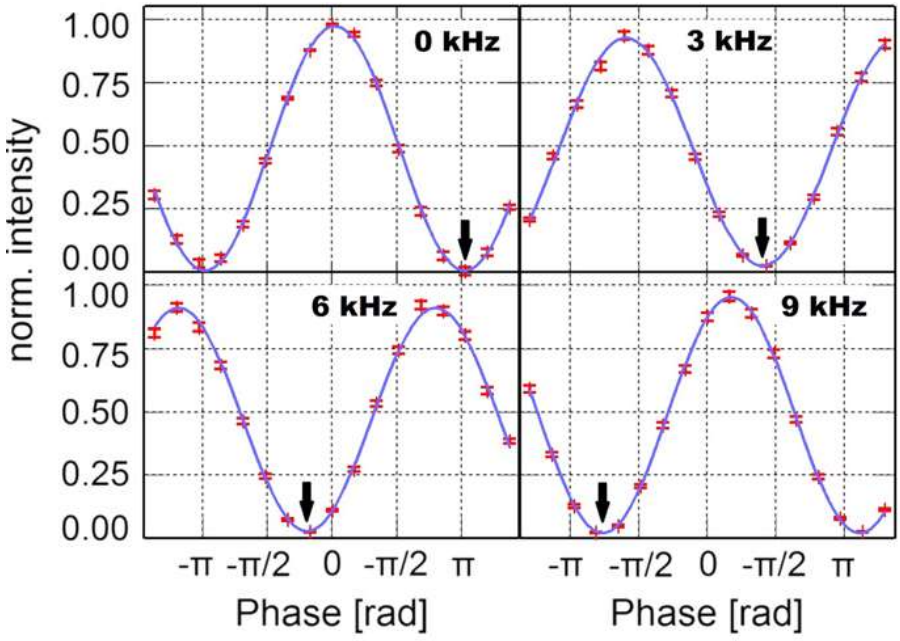

Figure 2.8: Polarograms of Demirel et al. [5]:"Shift of the periodic signal depending on the frequency. The minimum is marked with a bold black arrow to guide the eye. Each point has been measured for 2 min. The count rate at the intensity maximum is ≈4500 neutrons min^{-1}."

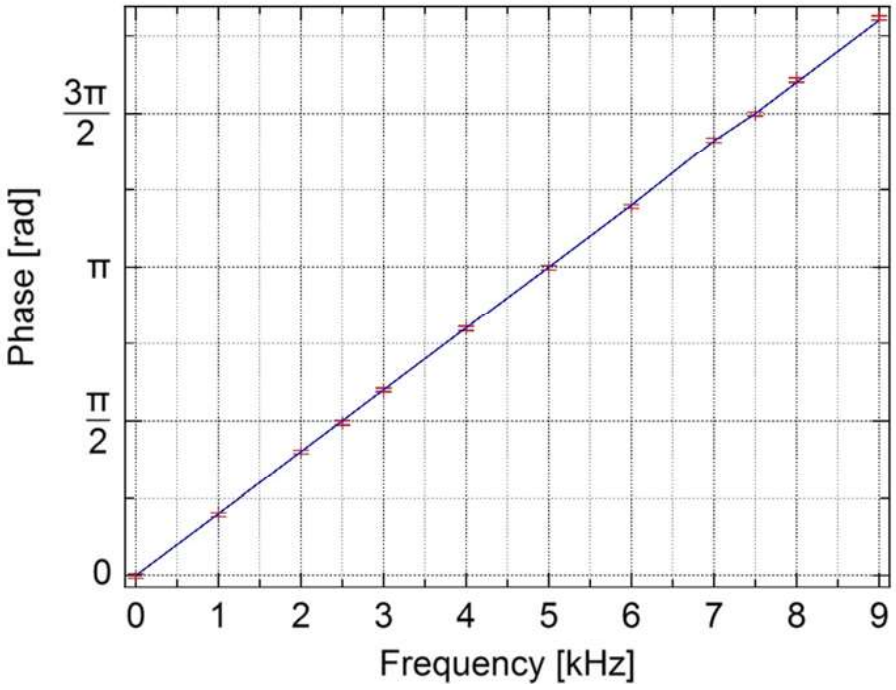

Figure 2.9: Results of the phase shift of Demirel et al. [5] :"Observed phase shift [...] together with the theoretically predicted dependence."

2.8 Proposed Interferometer Set-Up for Measurements in Grenoble

The planned set-up for an interferometrical experiment in Grenoble is as follows; the used devices are explained in more detail in chapter 3: A silicon monochromator is set into the neutron beam coming from the reactor. Its orientation is set to extract neutrons with a wavelength in the range of the maximum of the reactor spectrum of about 2 Å. The (220) net plane is suitable for this purpose. It reflects a beam with a peak at 1.91 Å. These neutrons pass through the magnetic prisms which split the paths of neutrons with different spin states (see Fig. 2.10).

Afterwards, the neutrons propagate into the region of the guide field. The first and last device in the guide field is a DC coil. Located between them are an aperture, the interferometer with the phase shifter in both arms, a Helmholtz coil and the Mashhoon box in a different beam each (more information about the Mashhoon box in chapters 4 and 5). The guide field ends in front of a supermirror that passes on neutrons with up-spins to the O-detector. The H-beam's intensity is recorded with a second detector for control purposes.

The first DC coil rotates the up-spins by $\pi/2$ into the horizontal plane. From here on, they undergo the Larmor precession in the guide field. The aperture trims the beam and reduces its divergence. A bigger window increases the count rate while reducing the contrast. A 5 mm × 5 mm cross-section is expected to be a good trade-off.

The interferometer is adjusted in a way that the beam of former up-spins is split by the first plate and traverses the interferometer on the proposed paths. The less than an arcsecond diverging beam of former down-spins deviates from Bragg's condition enough to allow only a small portion to be reflected. This portion produces a depolarising effect on the measurement. In the following, the behaviour of the chosen spin orientation is described. While in the interferometer, the neutron in the right arm of the interferometer enters the Mashhoon box with spin in beam direction. The spin

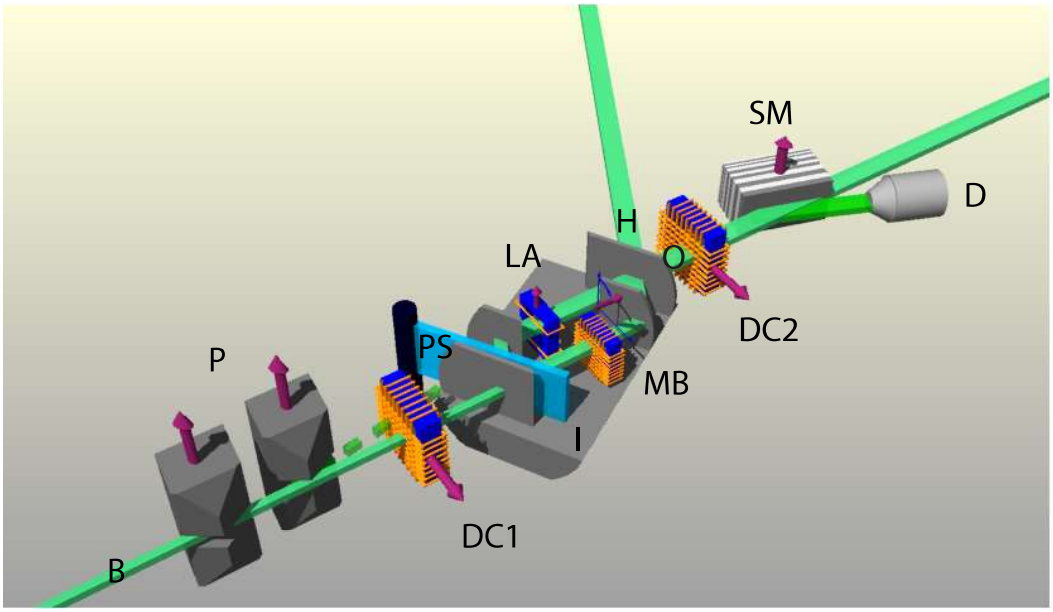

Figure 2.10: Planned arrangement of the optical devices after the monochromator for the interferometer experiment in Grenoble. The beam (B) is split by the magnetic prisms (P) according to the spin state of the neutrons (solid and dashed beams). The used beam is split into sub-beams at the first plate of the interferometer (I). Both sub-beams interfere behind the last plate as O and H-beams (O and H). A supermirror (SM) selects the neutrons of the O-beam with a specific spin state. A detector (D) measures the intensity behind the supermirror. Four coils are used in the set-up: the Mashhoon box (MB), a Larmor accelerator (LA), and two static spin manipulators (DC1 and DC2). The region of the guide field starts in front of DC1 and ends behind DC2. The phase shifter (PS) induces a relative phase between the two sub-beams. The neutrons of the dashed beam are not detected.

orientation is rotated by $\alpha = 2\pi$ inside the box (see Equation (2.42)) with a certain to measure phase. After leaving the Mashhoon box, the orientation precesses around the guide field again until the second DC coil which it enters in beam direction and wherein it is rotated by $\pi/2$ into an up-spin.

The second arm serves as a reference to the phase gathered by the proposed spin-rotation coupling inside the field of the Mashhoon box. At the last plate, the spin directions of both arms are tuned to be the same. To equalise the spin orientation at the point of recombination, the second beam is accordingly Larmor accelerated with a Helmholtz coil. This Helmholtz coil also equalises local guide field inhomogeneities that would induce another unwanted phase shift.

The phase shifter angle changes the relative phase between the two path states and regulates the detected intensities in the H and O-beam in the form of interferograms. The phase of sinusoidal fits to the interferograms is expected to be linearly dependent to the applied frequency in the Mashhoon box.

Chapter 3

Neutron Optics

3.1 Neutron-Optical Ansatz

The neutron was discovered in 1932 through its particle behaviour in collisions in experiments by Chadwick [27]. The connection between wave and particle properties is given by de Broglie's relation

$$\lambda = h/p, \tag{3.1}$$

with the wavelength λ, Planck's constant h and the particle momentum p. At high energies, the wavelengths get shorter and the interactions with the environment are confined to distances that are short compared to the environmental structures with distances a between them. We know the resulting singular effects as collisions. The considered object interacts with periodic structures when

$$\lambda \gg a, \tag{3.2}$$

which is the regime of light optics.

Although the respective particles, neutrons and photons, themselves differ in various ways, their common wave property seems similar in a mathematical and physical way. Experiments regarding the wave behaviour of neutrons use the basic concepts of optics developed for the manipulation of light. Many devices in neutron optics therefore copy the functions of their photonic counterparts and their names are similar. In this case, the scheme of the set-up is: source, monochromator, polariser, polarisation manipulators, analyser and detector. All the apparatus involved in the experiment are described below. Some of them violate Equation (3.2) as their function depends on $\lambda \sim a$.

The best known light-optical device, the lens, is not used for this type of experiment. The lens deals with divergence of light from a small source. The region where single neutrons are created radiates them radially in all directions, too. However, the divergence is mainly oppressed by apertures and, since it is small enough, it can be neglected in concept, although its effects can be measured.

3.2 Neutron Sources

Nowadays, experiments involving a large number of neutrons are realised mostly with reactors. Spallation neutron sources can be used, too. To initiate the nuclear reaction in the reactor, a radioactive neutron emitter is required which has a specific half-life and an according neutron flux depending on the geometry. A reactor creates an environment in which this neutron flux is

enhanced via a nuclear chain reaction and stabilised at a higher level of neutron flux. Usually, a mixture of uranium-235 and uranium-238 (^{235}U, respectively ^{238}U) is used in fuel elements that are arrayed as the reactor core. In the course of experimenting for this thesis, the TRIGA Mark II reactor at the Atominstitut of the TU Wien was used (see Fig. 3.1). TRIGA stands for training, research, isotope production, General Atomics. The reactor has a thermal power of 250 kW with a free neutron flux of $10^{13}\,\mathrm{cm}^{-2}\,\mathrm{s}^{-1}$ in the centre region [28]. The design is of the "swimming pool" type, with an open pool of water containing the core and control rods (see Fig. 3.2).

Figure 3.1: TRIGA Mark II Reactor in Vienna in the yellow coloured containment and different beam ports around it where free neutrons are used for experiments. (Photo from Section "Photos" in [28].)

Let us assume a nearly equal abundance of the two mentioned uranium isotopes at the beginning of our solar system some 4 billion years ago. Then the half-lives of about 4 billion years for the heavier isotope and 800 million years for the lighter one roughly explain the natural abundance of 0.72 % ^{235}U today. All others are trace isotopes.

The reactor is used to fission ^{235}U nuclei. ^{238}U is only present in the fuel because of the process to enrich the smaller isotope: chemically the isotopes cannot be separated, but centrifuges can concentrate them on their insides and outsides. The uranium enrichment of ^{235}U in the fuel elements is just below 20 %, the threshold between low and highly-enriched. The United States of America (USA) supply the fuel elements and assume enrichments above this threshold as being applicable for nuclear weapons. Therefore, they no longer deliver highly enriched uranium compositions. After the fuel is burned out, it is stipulated by contract, according to Austrian law (StrSchG §36b [29]), that the USA take them back. They are planning a deep geological repository at Yucca Mountain, Nevada. Whether it will hold steady the nuclear waste for the necessary time period of hundreds of thousands of years must be doubted. Only the low and intermediate level waste stays in Austria in the Seibersdorf Laboratories where most the nuclear waste of the country

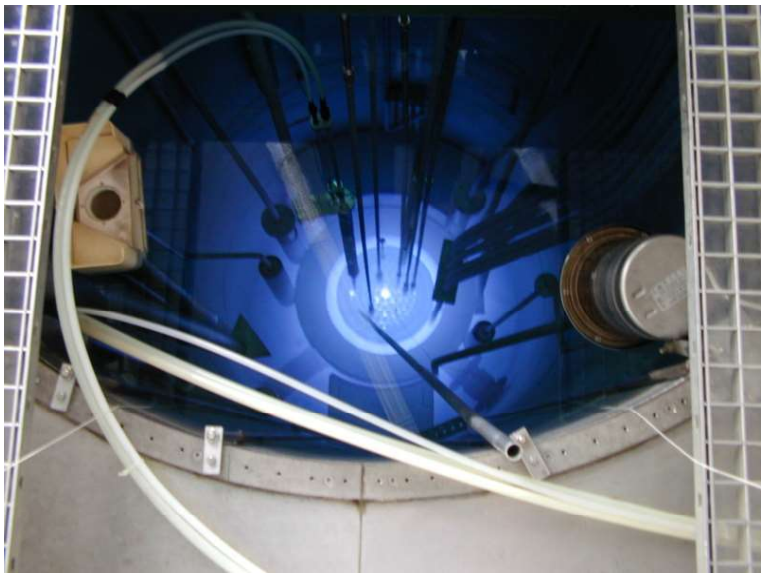

Figure 3.2: View of the reactor core inside the "swimming pool" illuminated by Cerenkov radiation. (Photo from Section "Photos" in [28].)

is stored according to law (StrSchG §36c [30]) on a provisional basis. Until now, some 350 000 t of waste have been stored there from sources like research reactors, medicine and industry. Some of the stored waste has decreased in its activity to below the dangerous limits, but what to do with the remaining waste in the future remains an open question. Austria will also have to find a deep geological repository for storage of many hundreds of years.

The history of nuclear technology is closely intertwined with military purposes. The commercial pressurised light water reactor is a result of research for submarine propulsion. Research on an alternative liquid fluoride thorium reactor (LFTR) type, which is claimed to have higher intrinsic safety during operation, supposedly produces magnitudes of order smaller quantities of waste and could even use some kinds of waste as fuel was suspended in the 1970s in favour of reactors breeding plutonium for nuclear weapons. In the last few years, LFTR has become popular again and might fulfil those high hopes in a couple of decades. Until then, we, the research community, can only hope that the waste produced in our investigations is responsible in light of human curiosity.

To return to the reactor, uranium has a specific half-life with free neutron emission in the range of billions of years. The resulting neutron flux of the fuel elements without chain reaction is very low. At a start-up where an exponential growth of neutron flux (supercritical level, described below) is necessary at some time, one needs to know the initial equilibrium in some precision. The devices used to measure the neutron flux inside the reactor cannot characterise the equilibrium of the reactor accurately enough at this level.

To ensure a sufficient neutron flux, a Sb-Be (antimony-beryllium) photoneutron source is used. ^{9}Be can be excited by photons with an energy of 1.67 MeV to decay in a nuclear reaction emitting a free neutron with an average energy of 24 keV. The necessary photons themselves are emitted by ^{124}Sb with a slightly higher but close enough energy of 1.69 MeV. ^{124}Sb is not a stable isotope. It is produced by neutron activation of the stable isotopes ^{121}Sb and ^{123}Sb, which are roughly of same abundance, in a reactor started with another neutron source. This characteristic classifies the Sb-Be source as secondary. Primary sources are used to start a reactor for the first time or after a long shut down when a secondary source has declined in its activity.

With their initial energy of keV the beryllium neutrons cannot induce fissions of ^{235}U nuclei.

Table 3.1: Classification of neutrons according to their energy, excerpted form [31].

energy (eV)	velocity (m/s)	neutrons' name
$<2 \cdot 10^{-5}$	<40	ultra cold
10^{-5} - $5 \cdot 10^{-3}$	40 - 10^{3}	cold
$5 \cdot 10^{-3}$ - $5 \cdot 10^{-1}$	10^{3} - 10^{4}	thermal
$5 \cdot 10^{-1}$ - 10^{3}	10^{4} - $4 \cdot 10^{5}$	epithermal
10^{3} - 10^{5}	$4 \cdot 10^{5}$ - $4 \cdot 10^{6}$	intermediate
10^{5} - $2 \cdot 10^{7}$	$4 \cdot 10^{6}$ - $4 \cdot 10^{7}$	fast
$>2 \cdot 10^{7}$	$<4 \cdot 10^{7}$	relativistic

Slower, "thermal" neutrons are far more likely to do that (see Table 3.1 for neutron classifications). To slow the neutrons down, collisions with other nuclei can be used. This is called "moderation". Good moderators are hydrogen, carbon and zirconium. Their absorption cross-section is small, but collisions transfer some of the neutrons's energy into their own motion. After many collisions, the energy distribution of free neutrons changes from the original peak characterising the initial nuclear reaction to a continuous thermal one, characterised by the temperature of the moderating elements of 300–600 K or 25–50 meV, respectively. The maximum of the new distribution is in this range. These thermal neutrons can actually stimulate ^{235}U to fission. Besides the two main daughter nuclei, their spallation also results in one or two fast neutrons with energies of some MeV which are moderated in turn. This means that a single free neutron can be transformed via moderation and fission into many more. Each step in the multiplication of the neutron number is called a "generation". Such a chain reaction mathematically results in exponential growth (supercritical chain reaction), decay (subcritical) or in stability (critical).

A small percentage of the fast neutrons will also fission ^{238}U nuclei inducing free neutron emission and contribute to the chain reaction without moderation.

A small portion of free neutrons come from the daughter nuclei. They are distributed in their mass with two peaks at about half of the mass of the parental nucleus. However, in general the ratio between protons and neutrons in the new nuclei is not ideal in terms of energy. Thus, the weak force can transform them into each other via β-decay. The remaining nucleus will be in an excited state. This stimulus decays most of the time via γ-radiation, but a small fraction is excited enough to emit a neutron. In time it is delayed to the initial fission process with its "prompt neutrons" and therefore called a "delayed neutron". The delay ranges from milliseconds to minutes and is very important for controlling the reactor at the supercritical level. A preferred way to start a reactor is to stay in the region of delayed supercriticality: without delayed neutrons the reactor would be subcritical, which slows the exponential growth in flux down. The control mechanisms react to the signals from sensors that measure e.g. neutron flux or temperature. In delayed supercriticality, the time window during a start-up between the occurance of an objectionable value and the moment the resulting problem gets out of hand is lengthened. The control is technically realised with different elements: moderators; reflectors that can redirect some part of the incoming neutrons back to their source where they may fission ^{235}U; absorbers that have the property of absorbing neutrons, and subsequently react without emitting neutrons again. Whereas reflectors and moderators are passive elements fixed in their positions inside the reactor, absorber rods are active control elements used to start, control and stop the chain reaction. These rods can be lifted and lowered to change their position in the high-flux region and their rate of neutron absorption.

A stable neutron flux is arranged if the rate of newly produced neutrons equals all losses of neutrons. The losses at a research reactor include for the chain reaction which are the whole reason for setting it up: the experiments using free neutrons. Neutrons can leave the TRIGA

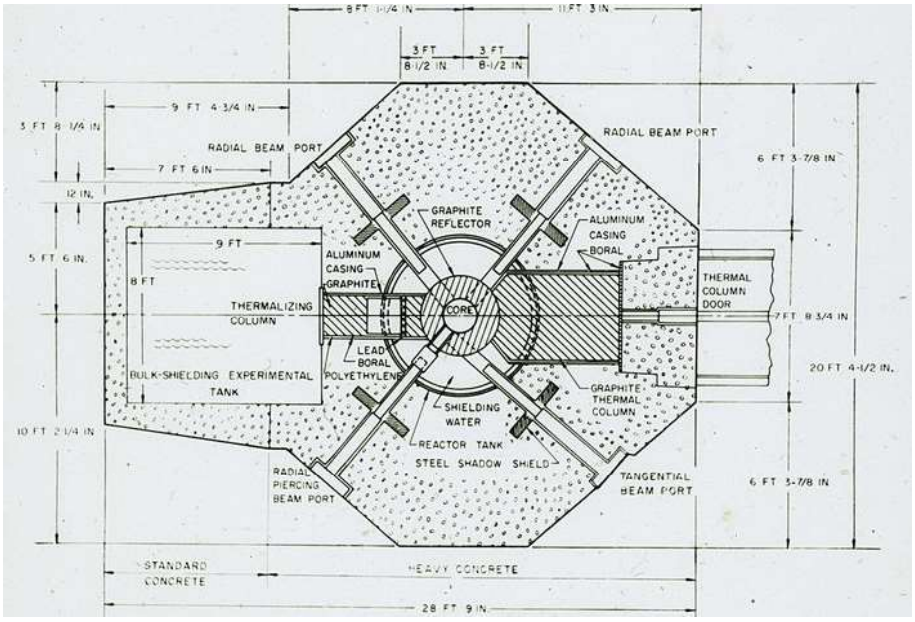

Figure 3.3: Cross-section of the reactor with four beam ports, the tangential beam port is to the lower right. (Figure from Section "Historical Photos" in [28].)

Mark II reactor through six opnenings that have no heavy concrete shielding. A shutter, that can be opened and closed, is positioned in each of these channels to block the resulting neutron beam at will. To conduct the measurements of this thesis, the tangential beam port was used (see Fig. 3.3). It does not directly show into the centre of the reactor but is shifted to the periphery of the core which causes a reduced neutron flux at this particular beam port. The advantage is the lowered γ-ray emission, hence less shielding is needed around the beam.

The experimental data collected by our working group is always gathered in form of intensities by counting neutrons. The count rate at a fixed set-up is always proportional to the level of neutron flux inside the reactor core. Examples of the neutron count rate in a single reactor start-up and shut-down is shown in Figure 3.4. Each one has a period of exponiential growth or decline that is in keeping with the microscopic model of neutron generations.

In Figure 3.4 the statistical errors for each count rate are also presented. Although in this section the process of the chain reaction was described where most free neutrons are caused by other neutrons, the underlying model for the error bars assumes all detected neutrons to be independent from each other. This assumption is backed by the fact that no prediction can be made if or where a neutron induces fission. The resulting Poisson distribution implies that a standard deviation for the average count rate N is given by its square root $\sqrt{N}$. Therefore, a higher count-rate has a reduced relative error.

Beside the neutrons, many other free particles are created – for example, from the β-decays charged electrons and positrons with relativistic energies. In the medium water wherein the speed of light is reduced, they can be propagating faster than light but still slower than light in vacuum. They interact electromagnetically with the water, resulting in their deceleration whilst emitting electromagnetic waves. As this light is slower than its generating particle, a light cone is produced (see Fig. 3.5). Its continuous spectrum reaches a maximum at high frequencies. Its visible portion is therefore in the blue (see Fig. 3.2 again).

This thesis deals with preparations for an interferometer experiment at the High-Flux Reactor at Institut Laue-Langevin in Grenoble with a thermal power of 58.3 MW. It works on the described principles, too. Inside the moderator region of the High-Flux reactor, the neutron flux is

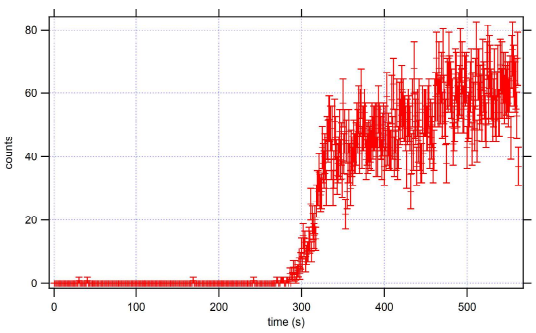

(a) Intensity of the neutron beam at the start-up. When the reactor is shut down, the count rate is near zero. At the start-up, the count rate grows exponentially and is stabilised at a specific level. At approx. 450 s, the guide field is turned on (see Section 3.4.1), that increases the intensity about 10 %.

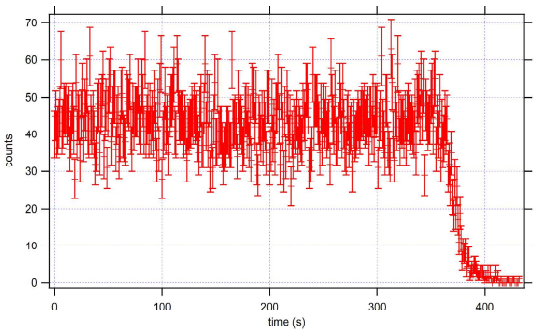

(b) Intensity of the neutron beam at the shut-down. The intensity is stable before it decreases exponentially.

Figure 3.4: Count rate at start-up and shut-down.

$1.5 \cdot 10^{15}\,\mathrm{cm}^{-2}\,\mathrm{s}^{-1}$, roughly corresponding to the difference in thermal power to the TRIGA Mark II reactor of the factor 200.

To understand why the reactor in Grenoble will be used, one has to grasp the measuring process itself: interferograms can only be recorded under conditions of thermal stability of the interferometer in the range of $\Delta T = 0.01\,\mathrm{K}$. Taking into account temperature fluctuations caused by varying weather conditions with their delayed influence on the temperature of the interferometer, this corresponds to a certain time window that can be used for recording an interferogram. With the present techniques used to insulate the interferometer in Grenoble, described in Section 3.6.1, this time window is in the range of hours. Carrying out a measurement with the same counts per measurement point required to comply the scientific standard would take weeks in Vienna. A thermal insulation shielding the temperature differences in such a time frame is not arguable. The TRIGA Mark II reactor is, therefore, not suitable for polarised interferometry.

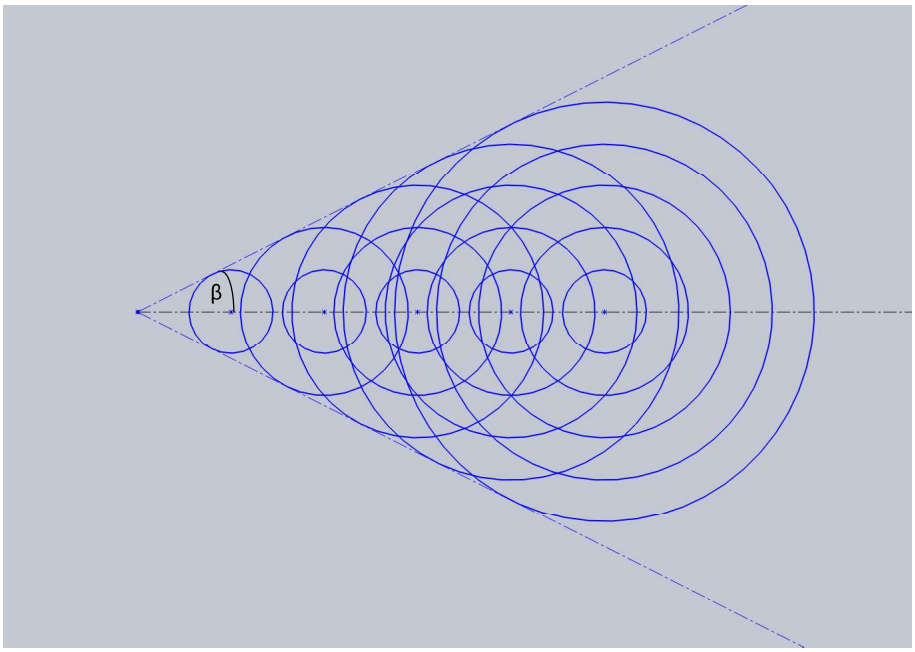

Figure 3.5: Scheme of spherical wavefronts generated by a particle with a higher velocity than the speed of light in the medium: the particle moves from right to left and continuously emits light. The partial wave fronts of equidistant points are shown. The merged wavefronts form a light cone with an opening angle β, with $\sin\beta = c/v$ where $c < v$.

3.3 Preparation

To research basic physical properties, it is necessary to simplify the process of manipulation. Each neutron should be manipulated in the same way, or at least in a known way. This means the neutrons should have similar properties when the manipulation takes place. Three important devices for the experiment are presented next that narrow the state space of the neutrons used.

3.3.1 Monochromator

A typical monochromator is a crystal with known composition and structure. It interacts with the beam from the reactor whose spectrum is continuous with a thermal characteristic. The lattice planes of the crystal have a distinguished orientation and reflect a Gaussian peak around a specific wavelength. Bragg's condition describes this process:

$$n\lambda = 2d_{hkl}\sin\theta, \tag{3.3}$$

with an integer n, the distance between the lattice planes d_{hkl} and the angle between incoming wave and the lattice plane θ (see Fig. 3.6). The indices h, k, l are the Miller indices that specify a set of lattice planes and a corresponding direction perpendicular to them. The formula results from the wave property of neutrons and specifies the case where the single reflected waves are phase shifted by $2\pi n$ which results in constructive interference. The refraction index for neutrons, like for x-rays, is generally smaller inside a material (see Section 3.3.3). Thus, the neutron wave undergoes no phase shift at the reflection itself.

Substituting de Broglie's relation (3.1) in (3.3), only neutrons with specific velocities are reflected at the angle θ. The integer n makes the relation ambiguous and higher order wavelengths with $n > 1$, the so-called harmonics, are also reflected in the same direction. As the maximum

of the thermal wavelength distribution coming from the reactor has been conveniently chosen to be the main peak, the secondary peaks are often of low intensity. Although the secondary peaks have influence on the experimental results, only one wavelength to be present is often a good assumption.

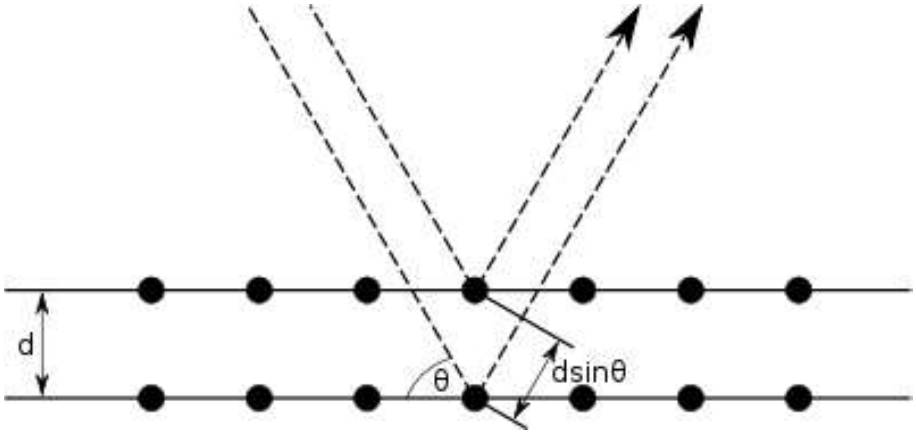

Figure 3.6: "Bragg diffraction. Two beams with identical wavelength and phase approach a crystalline solid and are scattered off two different atoms within it. The lower beam traverses an extra length of $2d\sin(\theta)$. Constructive interference occurs when this length is equal to an integer multiple of the wavelength of the radiation." Schematic under public domain from Wikipedia [32].

At the tangential beam-port in Vienna, three graphite mosaic crystals are used to extract neutrons with the three wavelengths 1.7 Å, 2.0 Å and 2.7 Å as seen in Figure 3.7, whereupon the beam with the latter has two other, considerable contributions of secondary peaks in its spectrum. In contrast to a single crystal, in a mosaic crystal many small crystals are pasted together with slightly varying orientations, resulting in a broadened peak in the spectrum reflected towards the beamline. The benefit lies in the intensity: if one domain of the mosaic does not allow neutrons of the desired wavelength to be reflected so that it is transmitted, the next one may have a suitable orientation for the reflection towards the beamline. The measurements of this thesis took place at the 1.7 Å beamline.

In Vienna, the monochromators and optical benches are fixed in their angles. In Grenoble, the instrument S18 is used for neutron interferometry as well as ulta small angle neutron scattering (USANS). The latter requires a different wavelength that is adjusted by a different angle via Equation (3.3). Moreover, the flux in Grenoble is high enough to sharpen the wavelength distribution of the neutrons: the wavelength peak is narrowed by implementation of three successive Bragg reflections on a silicon perfect crystal (see Fig. 3.8).

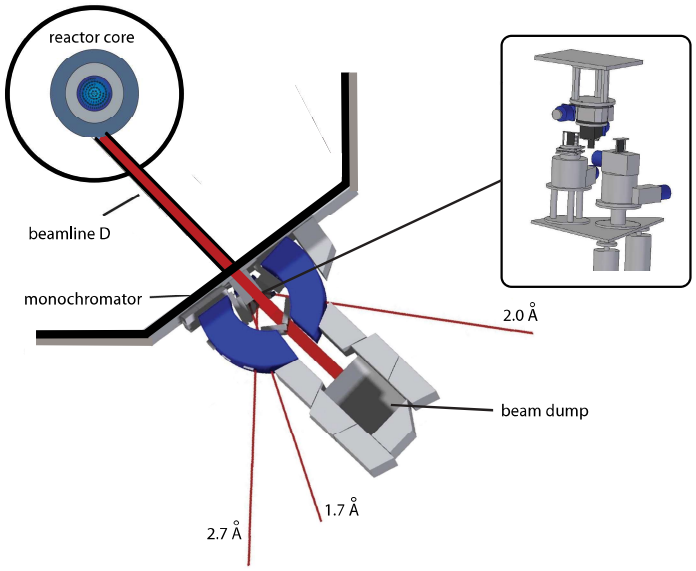

Figure 3.7: Tangential beam port with beam paths and arrangement of the monochromators.

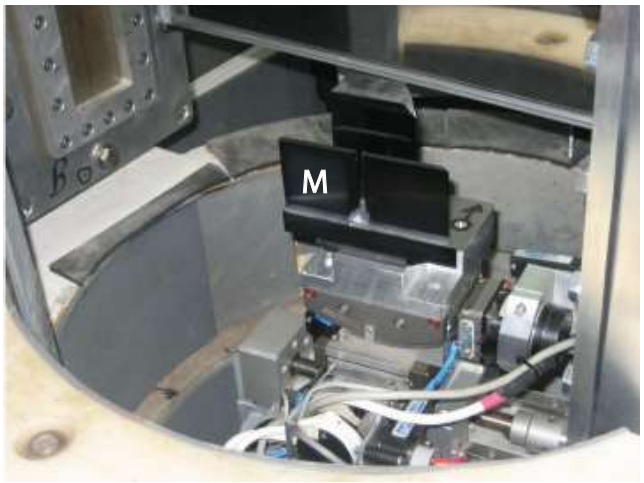

Figure 3.8: Monochromator (M) used in Grenoble with three plates for each reflection.

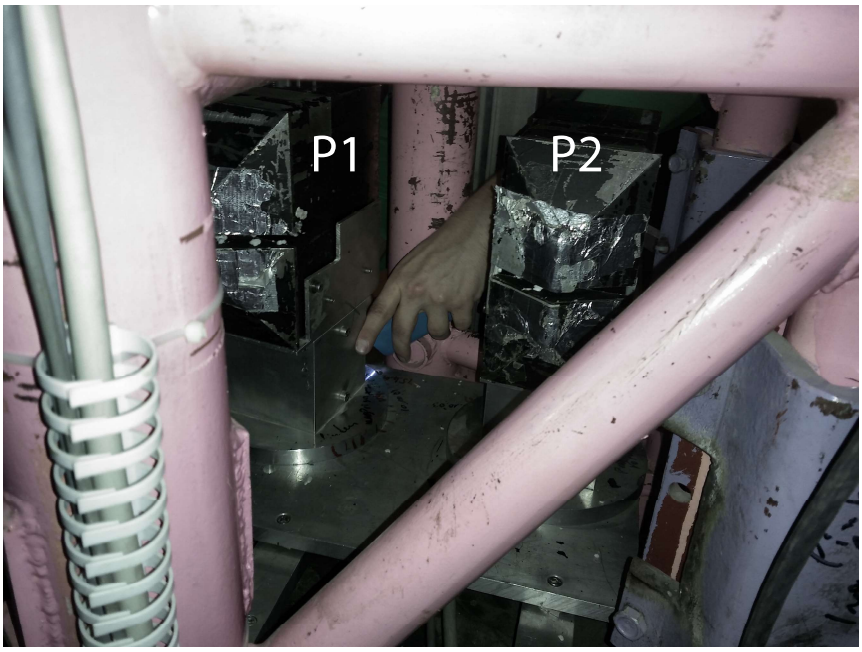

Figure 3.9: Two magnetic prisms (P1 and P2) as polarisers at S18 in Grenoble during the installation. Their slits are at the height of the back of the hand.

3.3.2 Magnetic Prism

To separate neutrons with different spin states from each other, magnetic prisms are utilised that interact with the neutron spin depending on the incident orientation. The prism itself is a large permanent magnet with a horizontal slit (see Fig. 3.9) where magnetic fields of about 1 T occur. To this day, higher fields can only be produced using superconducting magnets. Like light through an optical prism, neutrons flying through the triangular cross-section of the slit are refracted: Only a plane with $z = \text{const.}$ at the height of the slit is considered next. For the sake of the argument, the field inside the slit is regarded as constant and only in z-direction. Then only the transitions on the outsides of the slit have a field gradient. The Hamiltonian of this system is written $\hat{H} = -\vec{\mu} \cdot \vec{B} = -\mu_z \cdot B_z$ and any force $\vec{F} = -\vec{\nabla} E = \mu_z \vec{\nabla} B_z$. When the neutrons pass the first transition in y-direction, the force parallel to the direction of motion is

$$\vec{F_{\parallel}} = \mu_z \frac{\partial B_z}{\partial y}, \tag{3.4}$$

changing the velocity, whereas the force separating the trajectories of the spin states is

$$\vec{F_{\perp}} = \mu_z \frac{\partial B_z}{\partial x} \tag{3.5}$$

(see Fig. 3.10). The latter force vanishes only at perpendicular incidence into the slit. The resulting kinetic energies inside the field accord to the Zeeman effect:

$$E'_{kin;\uparrow,\downarrow} = E_0 \mp \mu B, \tag{3.6}$$

with the initial energy E_0. The negative sign corresponds to the case of an up-spin, the positive sign to a down-spin. Thus, neutrons with spins opposite the field's orientation have higher kinetic energy and velocity. According to their spin states, the neutrons will propagate in different directions. When leaving the prism through the second transition, the neutrons have different velocities and directions. Thus, the period of interacting with the second field gradient, that induces the forces,

also differs. In the second transition and in a specific parameter region of the angles of the geometry, the forces perpendicular to the directions of propagation cause neutrons with different spins to diverge even further. Simultaneously, the parallel forces realign their velocities again in any case.

In terms of waves, the wave number k is changed inside the field region:

$$\vec{p} = h\vec{k} \Rightarrow k = |\vec{k}| = |\vec{p}/\hbar|. \tag{3.7}$$

Alternatively, the Schrödinger equation gives the wave number (see next section). With $E_{kin} = p^2/(2m)$, Equation (3.7) results in

$$n_{\uparrow,\downarrow} = \frac{k_{\uparrow,\downarrow}}{k_0} = \frac{\frac{\sqrt{2m(E_0 \mp \mu B)}}{\hbar}}{\frac{\sqrt{2mE_0}}{\hbar}} = \sqrt{1 \mp \frac{\mu B}{E_0}}, \tag{3.8}$$

where the field as a medium is denser for the down-spins. Assuming small Zeeman splits $\mu B \ll E_0$, the generated angle of divergence δ was presented in [33] as

$$\delta = \frac{2\mu B}{E_0} \frac{\sin\phi}{\cos\phi + \cos 2\epsilon}. \tag{3.9}$$

With the apex angle $\phi = 116°$, a magnetic field in the slit of 0.88 T and a neutron wavelength of 1.895 Å, the calculated maximum divergence for two prisms is then about $2.4 \cdot 10^{-3}$ deg at the asymetric angle $\epsilon = 25°$. Figure 3.11 shows a measurement of an empirically good divergence of $1.2 \cdot 10^{-3}$ deg.

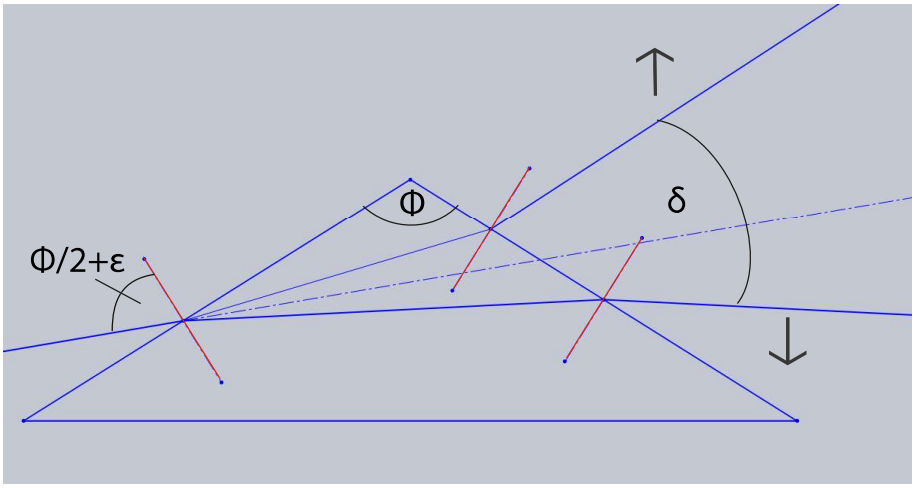

Figure 3.10: Scheme of the beam paths with plumbs to the surfaces in red. Initally co-traversing neutrons with different spin whose beampath is characterised by the asymmetric angle ϵ are refracted in a prism with apex angle ϕ to diverge with angle δ.

3.3.3 Supermirror

Before one can understand the use of the supermirror (see Fig. 3.12), the main steps in its development are presented: when dealing with neutrons, an essential problem is to arrange their direction of propagation. A beam port acts like an aperture. Behind it, a beam with a specific divergence and intensity of neutrons is produced. A common objective for high intensities is then to split the neutrons from the γ-radiation to reduce the radiation at the experiments with neutrons. One way to do this is to bend the neutron beam while the γ-radiation propagates straight to heavy

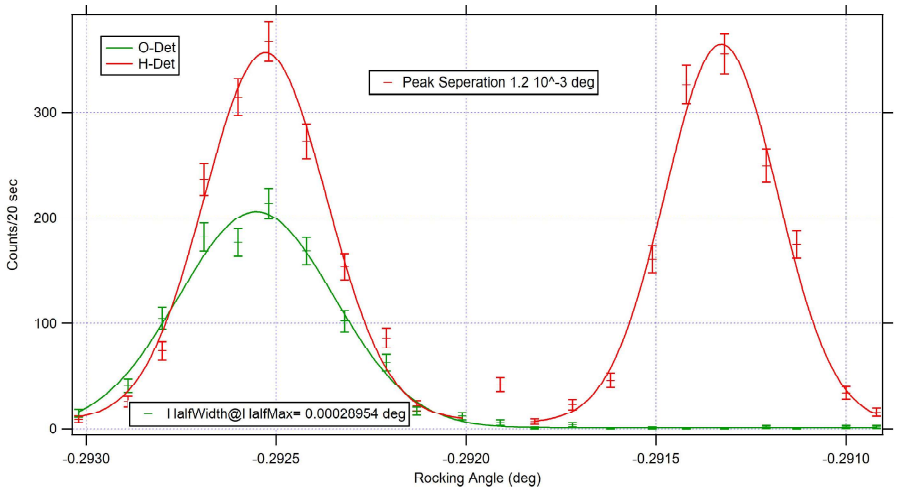

Figure 3.11: Measurement of the beam divergence after both magnetic prisms. Intensities of O and H-beam dependent on the orientation of the interferometer are recorded. Two peaks, each corresponding to a spin state, occur in the H-beam. In front of the O-detector, an analysing supermirror is placed which reflects only neutrons with a specific spin state towards the detector and suppresses the second peak.

shielding. For this purpose a curved neutron guide is used (see Fig. 3.13). Mathematically, the wave function of neutrons interacting with the material of such a guide represented by the potential V is described by the time-independent Schrödinger equation, calculated in this case as

$$\begin{aligned} \hat{H}\Psi(\vec{r}) &= E\Psi(\vec{r}), \\ \left(-\frac{\hbar^2}{2m}\vec{\nabla}^2 + V(\vec{r})\right)\Psi(\vec{r}) &= i\hbar\frac{\partial}{\partial t}\Psi(\vec{r}), \end{aligned} \tag{3.10}$$

$$\Rightarrow 0 = \left(\vec{\nabla}^2 + \frac{2m(E - V(\vec{r}))}{\hbar^2}\right)\Psi(\vec{r}) = \left(\vec{\nabla}^2 + k^2\right)\Psi(\vec{r}). \tag{3.11}$$

The wave number without interaction k_0 is

$$k_0 = \sqrt{\frac{2mE}{\hbar^2}}. \tag{3.12}$$

Then the refractive index inside the medium n follows as

$$n = \frac{k}{k_0} = \sqrt{1 - V/E}. \tag{3.13}$$

The potential V can in general be split into a nuclear (V_{nuc}) and a magnetic part depending on the spin orientation (V_{mag}) as

$$V_{\uparrow,\downarrow} = V_{nuc} + V_{mag} = \frac{2\pi\hbar^2 N}{m} b_c \pm \mu B_{eff}, \tag{3.14}$$

with the nuclei density N, the coherent scattering length b_c and the effective magnetic field in the medium B_{eff}. The nuclear potential here is derived from a Fermi pseudopotential

$$V_{nuc} = \sum_i \frac{2\pi\hbar^2}{m} b_c \delta(\vec{r} - \vec{r_i}), \tag{3.15}$$

with i as the index for all nuclei. The case $V/E > 1$ yields a complex n representing absorption or incoherent scattering. $0 \leq V/E < 1$ yields a refractive index $1 \geq n > 0$ and vacuum or air

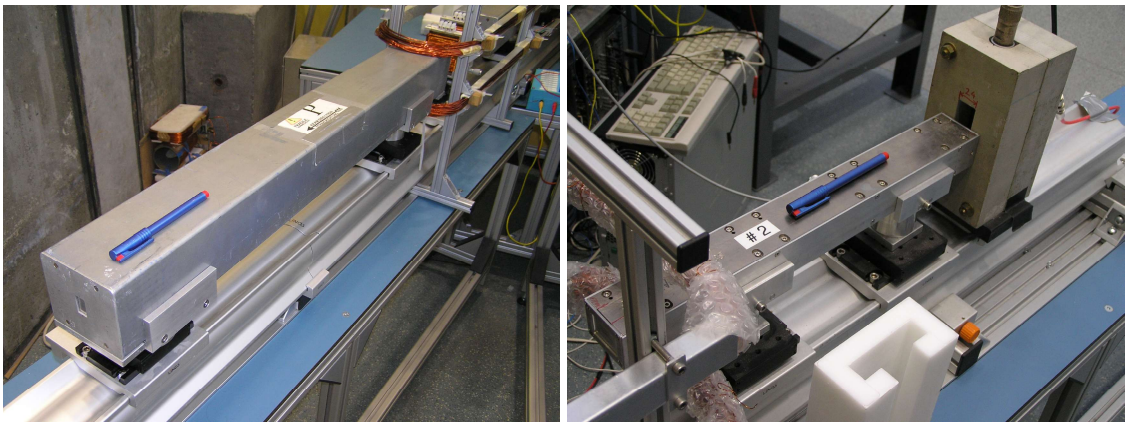

Figure 3.12: Two supermirrors with pen for comparison: to the left a larger model with higher degree of polarisation $> 97\,\%$ also used in Grenoble, to the right a smaller one used for the experimental tests of this thesis with degree of polarisation $> 90\,\%$. Please mention the windows located on their fronts, that neutrons can pass. The same type of window is on their backs as well.

will have a higher optical density than the medium. This latter case means that total reflection occurs below the critical angle between incident beam and the reflecting surface (see Fig. 3.14). For example nickel has a critical angle of approx. $0.1\,^\circ\,\text{Å}^{-1}$. A neutron beam with a higher divergence loses intensity. There are different approaches to avoid the loss of intensity for beams with higher divergence and make higher curvatures of beam guides possible.

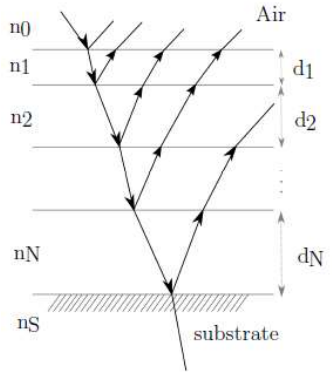

Figure 3.13: The structure of a general layer system of N layers with diameters d_i and refraction indices n_i between air and a substrate. [31] An incident neutron beam interacts with the structure. At each boundary layer, some ratio is reflected. In the case of the neutron guide, N equals 1 and only one layer is present. For the multilayer structure, two alternating materials are prepared with $n_1 = n_3 = n_5 = ...$ and $n_2 = n_4 = n_6 = ...$ Also the diameters are fixed and $d_1 = d_i$. In a supermirror, the materials are also alternating, but the diameters are decreasing with increasing number i of the layer. The resulting reflectivities are presented in Figure 3.14.

A first development was the multilayered structure. It is a layer system in which the two components alternate at fixed thicknesses in the nm range (see Fig. 3.13 again). With adjusted refraction indices, the resulting reflectivity has another region of high reflectivity but a more transmitting region in between (see Fig. 3.14 again).

A further development is the supermirror. Its layers alternate while the thicknesses of each layer decreases (see Fig. 3.13 again). With the right arrangment of layer diameters and refractive indices, the supermirror's reflectivity features a widened range of angles with high reflectivity

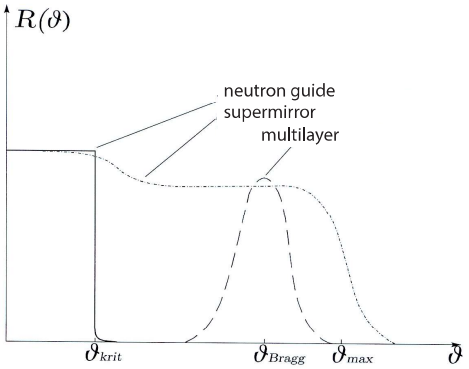

Figure 3.14: Reflectivity R in dependence of the incidence angle to the surface ϑ for three different structures [34]: the neutron guide, the multilayer system and the supermirror. The neutron guide has a reflectivity of 1 until the critical angle at which the reflectivity jumps almost immediately to zero. The multilayer structure has the same reflectivity as the neutron guide below the critical angle but at the Bragg angle an additional peak in reflectivity. The supermirror has a high reflectivity in a range of multiple critical angles.

(see Fig. 3.14 again). Furthermore, one can modify the system: one non-magnetic material can be chosen while the other is magnetic, resulting in different refraction indices for each spin component. There are combinations of materials that have almost the same index for one spin orientation but differ in the other one. The layers of our devices are composed of cobalt (magnetic) and titanium (non-magnetic). Therefore, neutrons of one spin component will mostly be transmitted through the layers to an absorber and do not occur behind the apparatus in contrast to the magnetic prisms, where neutrons of both spin states exit the device. The small fraction of neutrons with opposite spin orientation reflected lowers the polarisation of the subsequent beam. These are the properties nowadays used for polarimetry and polarised neutron interferometry: one polariser (prism for interferometry or supermirror for polarimetry) at the front of the beam selects the spin state regarded as up-spin. After some manipulations a supermirror is placed in front of the detector as an analyser. As only polarising supermirrors are used in this thesis, they are called simply supermirrors.

Ideally, the estimated loss of intensity of a totally mixed spin ensemble after its interaction with the supermirror is by the factor of 1/2 that represents the split in two equally present spin states. However, a further reduction is produced due to the incidence of the beam that does not match the situation presented in Figure 3.6: the beam penetrates the supermirror not only from the top of the layer system but also its side which empirically leads to a total factor of intensity loss of about 1/4.

3.4 Neutron Spin in Magnetic Fields

3.4.1 Guide Field

Spin manipulators are realised by using magnetic fields that interact with the neutron spin. As magnetic fields decrease with the distance to their source quadratically but extend in principle into infinity (see Biot-Savart law in Equ. 4.1), different manipulators have to be separated spatially in order to reduce interference with other manipulators. In the region between the manipulators, a superposition of weak fields from various sources occurs, e.g. from the manipulators themselves, their sources or earth's magnetic field. When interacting with the neutron, this would result in

undesired and complex spin manipulations.

Instead of neglecting or trying to suppress this effect, the whole set-up is coverd by a magnetic guide field reducing the influence of ambient field disturbances. The guide field is a magnetic field in z-direction generated by a direct currrent (DC) in coils of Helmholtz geometry in order to homogenise the field in the region of the beam (see Fig. 3.15). Its magnitude is much stronger than all the stray fields in the region between the manipulators. In its regime, this field is dominant and all stay fields can be neglected. As a consequence, the magnetic field in z-direction conserves its spin eigenstates $|\pm z\rangle$. They accumulate a phase while in the guide field according to

$$\psi(t) = e^{-\frac{iHt}{\hbar}}\psi(0) = e^{\frac{i\mu Bt}{\hbar}}\psi(0) = e^{\pm i\omega t}\psi(0), \tag{3.16}$$

with the angular frequency ω. The positive sign on the right hand side corresponds to a down-spin, the negative sign to an up-spin. States in a superposition of its two eigenstates therefore accumulate a relative phase. Consequently, the neutrons undergo the Larmor precession. This is a rotation of the spin polarisation around the direction of the guide field, following the Larmor angular frequency

$$\omega_L = -2\mu B/\hbar. \tag{3.17}$$

The factor 2 in this formula comes from adding the angular frequencies of the two eigenstates in Equation (3.16) to a relative phase. The frequency in time is then

$$f_t(B) = \frac{|\omega_L|}{2\pi} = \frac{2|\mu B|}{h} \tag{3.18}$$

or in space

$$f_x(B) = \frac{f_t}{v} = \frac{2\mu B}{hv} = \frac{2\mu Bm\lambda}{h^2} = 0.012\,532\,\mathrm{cm}^{-1} \tag{3.19}$$

for neutrons with a wavelength specified to 1.7 Å and a field of 1 G. The length for one full Larmor precession in a guide field of 9 G, becoming important in the measurements, is calculated as

$$1/f_x(9\,\mathrm{G}) \sim 8.87\,\mathrm{cm}. \tag{3.20}$$

Thus, instead of preparing a specific spin state with some coil and letting it enter the next coil, a spin state with the same polar angle ϑ, as introduced in equation (2.7), is prepared with the first coil. The distance between the first and the second coil is then chosen such that the Larmor precession between them results in the necessary state as its input for the second coil.

3.4.2 DC Coils

The effects of homogeneous fields are very easy to calculate and control. DC coils are used to generate them. The most basic one, which will be required in the interferometer experiment, is a Larmor accelerator: It only generates a field that amplifies the guide field locally, increasing the Larmor frequency in its region. In principle, the guide field itself is a DC coil, too. However, the crucial property for maintaining the polarisation is reason enough to present it separetly.

The other type of DC coil is used to generate an effective field in x-direction (see Fig. 3.16 and for the adjustment procedure Section 5.2). In fact, it consists of two coils. One coil generates a field in z-direction of the guide field's amplitude but in the opposite direction (antiparallel). The superposition of all fields in this region is then assumed to be zero. The other, perpendicular coil generates the field in x-direction with some field amplitude B_x. The mounting of the coils can be tilted to align the resulting fields with the polariser and the guide field as well as lifted to control the neutron beam's incidence to the coils.

In contrast to a voltage source, whose currents and therefore created fields will change in time due to the induced heat that changes the electrical resistance, the coils are supplied with current sources to stabilise the magnetic fields.

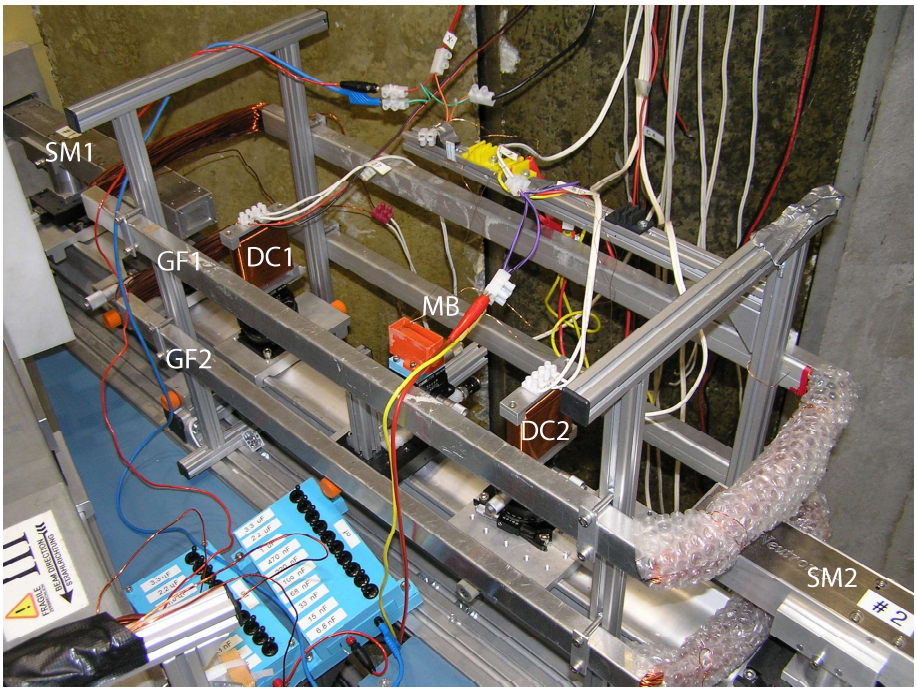

Figure 3.15: The guide field coils (GF1 and GF2) located centrally between two supermirrors (SM1 and SM2). Two DC coils (DC1 and DC2) and the Mashhoon box (MB) are placed in it.

3.5 Detectors

As source for this section, Chapter 4 of the "Vorlesungsskriptum Neutronen und Kernphysik" [35] was used. Most neutron detectors use the same principle: an incoming neutron causes an initial nuclear reaction with a nucleus. For thermal neutrons, ^{3}He and ^{10}B have high cross-sections for the following reactions:

$$^{10}\mathrm{B} + \mathrm{n} \longrightarrow {}^{7}\mathrm{Li} + \alpha \qquad \text{and}$$
$$^{3}\mathrm{He} + \mathrm{n} \longrightarrow {}^{3}\mathrm{H} + \mathrm{p} \qquad \text{respectively}\,.$$

The gases helium-3 (^{3}He) and boron trifluoride (BF_3) are typically used in gas detectors which are realised as counter tubes (see Fig. 3.17). Subsequently, a chain reaction is produced: The binding energy transforming into kinetic energy in the nuclear reaction is in the range of MeV. Consequently, the lighter of the reaction products with most of the kinetic energy is fast enough to pass the electronic cloud, bound to the heavier nucleus with higher charge, without binding electrons. A pair of primary ions is the result. Both of them have high energy and cause secondary ions on their trajectories. These secondary particles are then accelerated inside an environment of high voltage and, through collisions, cause a cascade of charged particles, mostly electrons. The electrons are light and are accelerated much more than the heavy primary ions by the electric field. In this process, these electrons amount to most of the current between anode and cathode that can be integrated to a charge with macroscopic instruments. In the gas, the electron has a mean free path dependent on the pressure. Since an electron must have a minimum kinetic energy to ionise an atom through a collision and generate a chain reaction with more free electrons, high electric fields of about $1 \cdot 10^6\,\mathrm{V/m}$ are implemented: the geometry is chosen cylindrically. In its centre, a fine wire composes one electric pole, the outer wall is the other. The anode, which the electrons are accelerated to, is chosen as the wire. The wall is then the cathode which is most often

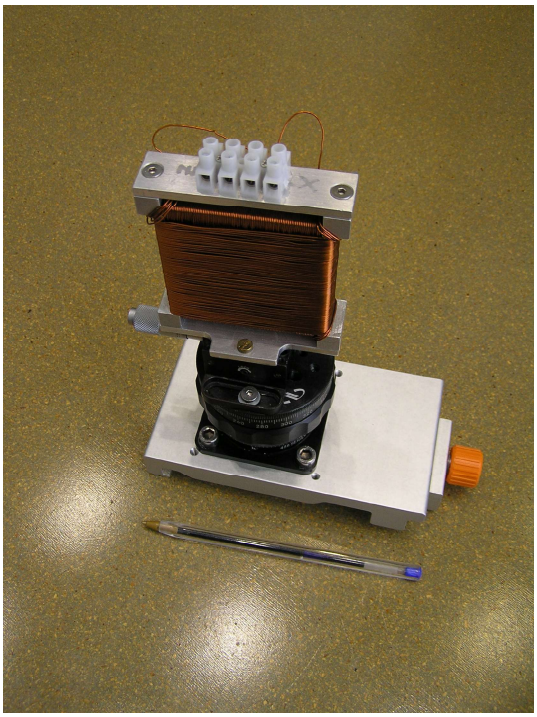

Figure 3.16: DC coil on top of a mount (grey platform) for the polarimeter with a pen for comparison. The two black elements can be used to adjust the height and tilt of the coil. The dimensions of the coils are about 2 cm × 12 cm × 12 cm. For the two wound coils there are 4 screw terminals on top.

grounded. Because of the geometry, the electric field strength will rise with lowered radius r to the centre of the wire with $1/r$. For a fine wire with diameter of 0.1 mm, this arrangement allows to reduce the voltage used to about 1 kV while a parallel-plate capacitor with the same gas pressure needs voltages of tens of kV for the same field strength. Outside of the high field volume of the cylindrical geometry, any collisions of electrons will not cause any ionisations, but the electron will again be accelerated to the anode. The volume where the energy added on a mean free path of an electron is high enough for an ionisation is also very small compared to the total volume. This means, wherever in the counter tube a secondary ion is created, it is most probable to result in the same signal.

Adjusting the detector is a delicate process: The signals of γ-rays which are also present have to be distinguished from those of nuclear reactions induced by neutrons. Ideally, when the detector is very big, all neutrons lead to the same kind of reaction and a single peak will be detected. In reality, the detector has finite dimensions and wall effects will change the signal spectrum: If the nuclear reaction takes place near the anode, the primary anion can be adsorbed immediately without a multiplication of its charge. A signal of less charge, compared to the ideal one, is the result. In Figure 3.18 one can see an adjusted spectrum of a ^{3}He detector. The lower energy peak is γ-noise that must be discarded. The main peak at high energies corresponds to the case where the initial reaction has a sufficient distance to all walls so that the primary ions cause a maximum number of secondary ionisations. In between are signals form neutrons which generate different signals because of wall effects.

Each signal is sent to a pre-amplifier. The presented spectrum is recorded by a multi-channel analyser (MCA) that gets its input from the pre-amplifier via an analog connection and discriminates signals depending on their amplitude into different pins. At a high-voltage in the detector

of about 1 kV, the γ-peak and the signals from neutrons can be distinguished while the resulting signal to the pre-amplifier still depends on the number of secondary ions. This voltage domain is called "proportional region"; within this region a particular voltage is set to be the working point. For much higher voltages, all signals lead to oversaturated chain reactions and γ-rays cannot be differentiated any more. Lower voltages do not initiate a chain reaction or do not cause any signal of neutrons at all.

The MCA has a maximum signal input amplitude of 5 V. Above this value, it cannot distinguish signal amplitudes from each other and passes them on as 5 V signals. At the pre-amplifier, in combination with the high-voltage, the gain, i.e. the amplification, can be changed such that the main neutron peak of the spectrum is at about 3.5 V. To count the neutrons, the transistor-transistor logic (TTL) output of the pre-amplifier is used that only sends a binary signal. The additional threshold feature of the pre-amplifier allows to specify the signal amplitude below which no signal is sent through the digital output, neglecting the γ-noise. Usual γ-rays from a reactor induce only a few ionisations and the signal voltage is low. The threshold is conveniently chosen in the minimum between γ-peak and the lowest neutron signals.

Although two primary ions are accelerated and each produces a signal, the whole process is in the range of nanoseconds, too fast for the time-resolution of any neutron detector to distinguish both signals.

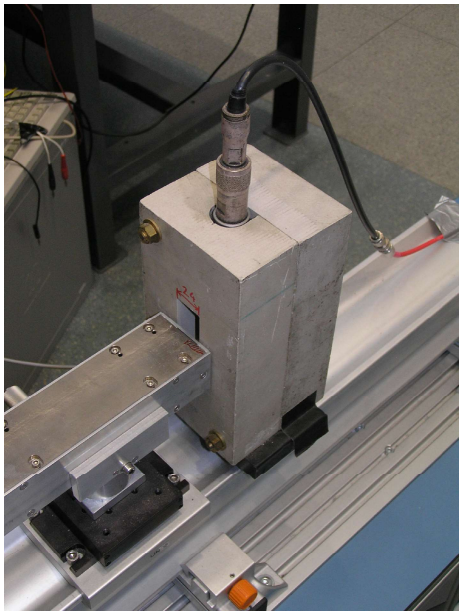

Figure 3.17: The detector behind the supermirror in its boron carbide shielding. A high voltage is applied to register neutrons and a detecting signal is transported to a computer through the cable.

3.6 Experimental Techniques in More Detail

3.6.1 Neutron Interferometry

Theory

A detailed overview of neutron interferometry and source for this section is given by [36]. The principle of neutron interferometry was described already in Section 2.5.1. Although a scheme of the procedure is easily drawn, when the physical object discussed is the spin of neutrons,

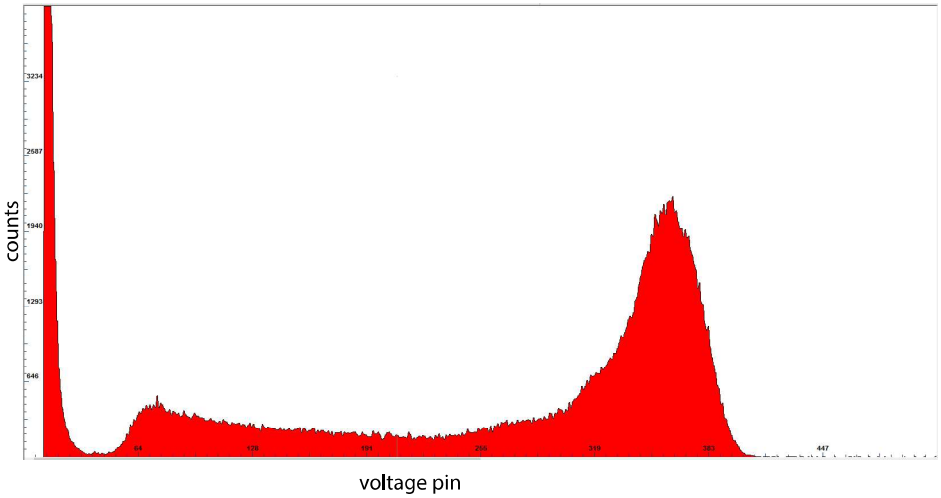

Figure 3.18: Spectrum of voltage signals from the detector. The energy is proportional to the voltage signal.

there are serious endeavours to realise this in experiments. An approach reflecting the pattern is now well established. The first realisation of relative phase shifts in neutron interferometry was done at the reactor in Vienna [10]: single neutrons are split in their amplitudes into two parts spatially separated by several cm inside a perfect crystal interferometer (see later in this section). These dimensions are big enough to construct spin manipulators that approximately interact with only one of the arms. The two beams are then recombined coherently. After this recombination, two beams emerge from the interferometer in different directions: the H-beam (name from the reflection vector $\vec{H}$) and the O-beam (letter O from the number $0 = \vec{H}$) only displaced horizontally with respect to the incident beam in front of the interferometer. The O and the H-beam are superpositions of the two paths inside the interferometer.

In addition to the two spin states, the two separated paths of the beams in the interferometer found another two level system in Hilbert space. In analogy to the Bloch sphere for the spins, the path states can be regarded as poles and O and H-beam are their own perpendicular system of equal superpostions of them. Phase shifts between the interferometer arms can be interpreted as change of the direction of projection, leading to complementary detection rates. Phase information can be gained by comparing the intensities in those directions with and without the researched interaction.

A common design of neutron interferometers uses three plates where transmissions and reflections occur. An adapted version where the function of the middle plate is executed by two different plates is presented in Figure 3.19. The H-beam is a superposition of a portion that was reflected (denoted as factor r in next formula) once and transmitted (factor t) twice and a portion that was reflected three times. The O-beam was reflected twice and reflected once in different permutations for both its portions superposed. This consideration allows to calculate the intensities in both beams leaving the interferometer in relation to the incident amplitude ψ_0 and the relative phase between the arms $\Delta\chi$ (see Appendix A.2 for derivation):

$$\begin{aligned} I_O &= |\psi_I + \psi_{II}|^2 \\ &= |rrt\ \psi_0 e^{i\chi_I} + trr\ \psi_0 e^{i\chi_{II}}|^2 \\ &= A(1 + \cos\Delta\chi) \end{aligned} \tag{3.21}$$

with $A = 2|r|^4|t|^2|\psi_0|^2$ and $\Delta\chi = \chi_{II} - \chi_I$. For the H-beam the same considerations yield

$$\begin{aligned} I_H &= |\psi'_I + \psi'_{II}|^2 \\ &= |rrr\ \psi_0 e^{i\chi_I} + trt\ \psi_0 e^{i\chi_{II}}|^2 \\ &= B - A\cos\Delta\chi \end{aligned} \tag{3.22}$$

with $B = |r|^2(|r|^2+|t|^2)|\psi_0|^2$ what implies

$$I_O + I_H = A + B = const. \tag{3.23}$$

An important expansion is interfereometry with polarised neutrons: Up and down spin states are split by magnetic prisms (see Section 3.3.2) in front of the interferometer dependent on their projections on a chosen axis. The interferometer is adjusted to let only one spin component satisfy the Bragg condition and pass the interferometer in a way O and H-beams occur. States in both kinds of systems, spin and path, interfere separately with possible phase shifts. An increased interaction continuously inducing only a phase for one arm would then, according to Equations (3.21) and (3.22), be detected as sinusoidially changing count rates.

It is, however, conventional for multiple reasons to use an additional phase shifter (see description below) that induces another relative phase between the arms. Different tilts of this device, that both beams pass through, induce different relative phases. First of all, the ideal case of only the interaction of interest present is never given. There is always some phase shift from multiple sources. A phase shifter at least allows one to control the phase and to set a reference of one's choice. Secondly, in this way, using the phase shifter one can continuously change between constructive and destructive interference for O and H-beam and always check whether coherence is still given. Without coherence the amplitude of the intensity oscillation induced by the phase shifter would shrink or vanish altogether. A measure for the quality of the coherence is the contrast C. It uses the comparison of the respective minimal and maximal intensities I_{min} and I_{max} in the expression

$$C = \frac{I_{max} - I_{min}}{I_{max} + I_{min}}. \tag{3.24}$$

Thirdly, the resulting interferogram offers an interpolation of a sinusoidal fit function with phase as fit parameter that is statistically more reliable than just the single point measurable without phase shifter.

As already explained, the interference depends, beside the states, also on the phases of the sub-beams. A crucial condition for making this work is the phase homogeneity of each beam. If an arbitrary phase is added dependent on the position in the beam cross-section, another added phase induced by the researched interaction will not change the count rate of O and H-beam. This is a general problem in dealing with neutron interferometry, as the mechanism of phase shifter and interferometer (read below) rely on matter in the beams that can induce phases dependent on time and the position in the cross-section. When electromagnetic coils near the interferometer are involved, it is inevitable to cool them. Without cooling, the interferometer plates deform in comparison and, in macroscopic terms, give rise to an arbitrary phase induced by the main mechanism of convection.

Interferometer Crystal

The silicon perfect crystal is the heart of the proposed interferometer experiment. In principle, the interferometer interacts the same way with neutrons as the perfect crystal monochromator: if the Bragg condition is fulfilled, the partial waves interfere constructively at the reflective angle.

The differences between both devices lie in their shape and used orientation to the neutron beam: while a reflected beam does only penetrate the surface of the monochromator because the used planes are parallel to the surface, in the interferometer it is reflected from the same planes but transmitted through the crystal plates at the same time (see Fig. 3.19). This is called a "Laue geometry".

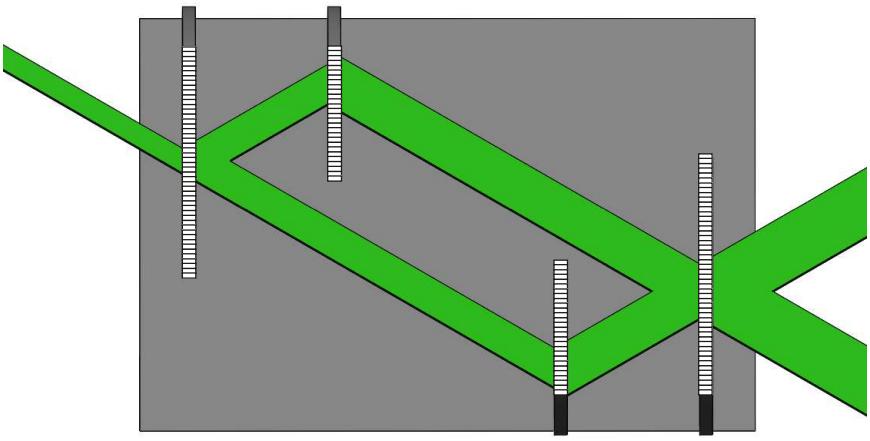

Figure 3.19: Sceme of the beam paths (green) in the scew-symmetric interferometer (grey). The four interferometer plates are in white. The (220) reflection planes inside the interferometer plates are perpendicular to the surface of the material which defines a Laue geometry. With each passing of a plate, the beam becomes broader by the plate diameter.

The technology to fabricate perfect silicon crystals is well established and researched due to their use in computer technology. The aspired form is cut out of the crystal and its surface etched to remove distortions. The interferometer that will be used is of skew-symmetric design to allow space for larger manipulators than in other designs. The perfect crystal is composed of face-centered cubic diamond structures with lattice parameter $a = 5.43\,\text{Å}$. The lattice parameter for the used plane (220) is then $d_{220} = \frac{a}{\sqrt{2^2+2^2+0^2}} = 1.91\,\text{Å}$, which is in the region of the maximum of the thermal neutron distribution. (For a more detailed decription, see [37].)

Every plate splits the neutronic wave by amplitude into two beams of almost the same intensity. The two beams reflected at the middle plates can interfere from the last plate onwards. The interaction of the beam inside the crystal is treated with dynamical diffraction theory. The used angle of 30° between beam and net planes is in a Laue geometry equivalent to an angle of 60° between beam and surface of the plate. Therefore, the beam is at each plate broadened perpendicular to the net planes by the plate diameter of 3 mm (see Fig. 3.19 again) due to reflections that take place throughout the plate diameter. The vector normal to the net planes is usually aligned horizontally.

The perfect crystal is to interact with a neutron at all four plates the in same way, therefore thermal stability is very important: if different temperatures occur at the plates, thermal expansion will deform them in relation to each other. The lattice parameters will vary and the different wave parts in each arm of the interferometer will gather random phases that suppress the so-called Moiré fringes. The microscopic behaviour is regarded as highly time-dependent because of thermal convections. There are different means to prevent this from happening (see also the section about air conditioning below and 4.3).

Phase Shifter

One degree of freedom between the sub-beams in the interferometer is their relative phase. A phase shifter that reaches both arms can induce such. In the case of the present experiment, a sapphire crystal plate will be used. It has a diameter l and its refractive index for neutrons n is below 1 with a difference to the relevant index of air Δn. This means the neutrons are propagating faster in sapphire than in air. According to the relation $\lambda = h/p$, the wavelength inside this material is smaller, so when the wave exits the crystal, the phase is in general different from that without the crystal present. This holds for both paths. If the angle α between the sapphire and interferometer plate can be varied, the path length through the sapphire crystal of one path can be shortened while lengthened in the other, resulting in a difference of path lengths through the phase shifter Δl. Hence, the relative phase can be controlled, following in first order $\Delta\varphi = \Delta n \Delta l = \Delta n l \cos\alpha$.

Concomitantly, a spatial shift between the incoming and outgoing beam of the sapphire occurs. The phase shifter could, without cooling of the coils, induce a temperature dependent phase shift like the interferometer, too.

Other Critical Devices for Interferometry at instrument S18

Oscillations of the interferometer can disrupt the measurements, as described above, by inducing dephasing. These have two main sources: mechanical vibrations and thermal fluctuations. For each of these sources, separate insulations are implemented at the beamline S18:

1. Optical Bench/Table

The interferometer is placed on top of an optical bench which is mounted on multiple large springs with high stiffness to decouple the interferometer from environmental vibrations. The table on which the interferometer is standing can be rotated with a piezo crystal. Another motorised micrometer screw can adjust the so-called ρ-axis that can tilt the table. Both are necessary to adequately position the interferometer. Without them, it is not possible to achieve the necessary angular accuracy of adjustment.

2. Air Conditioning

As mentioned previously, the thermal control of the interferometer is crucial. The beamline S18 is located inside a big experimental hall, where various experiments take place. As primary thermal insulation the whole apparatus is set up inside a cabin (see Fig. 3.20). A couple of years ago, another insulating chamber was constructed on the inside. An air conditioner (AC) on top of the cabin can provide air at an exit between these two structures and is fed via an entry on the other side of the room. The AC is supplied with fresh water as medium to exchange heat with. Its regulation relies on a sensor measuring the temperature on top of the chamber. Various other sensors are positioned at the following locations to control the stability: at the exterior top of the cabin, in the ceiling of the cabin, in the ceiling of the chamber, on the floor of the chamber, and near the output of the air conditioner.

In addition, an acrylic glass frame surrounds the interferometer crystal. The frame has an opening on top implemented to insert spin manipulartors into the interferometer.

3.6.2 Neutron Polarimetry

Neutron polarimetry was already briefly described in Section 2.5.2. To realise the concept, a polariser selects one spin orientation. Different spin manipulators are then used to change this

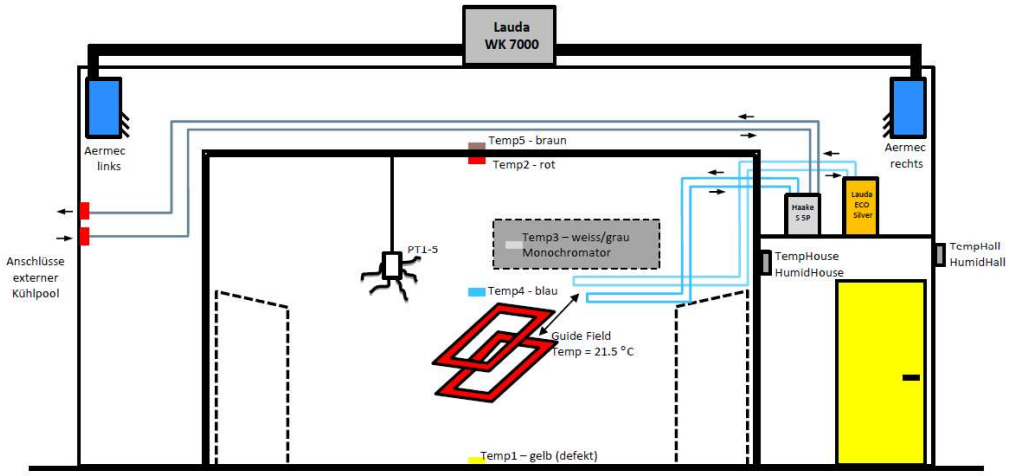

Figure 3.20: Scheme of the thermal insulation and control at the instrument S18. The outer structure of the instrument is a cabin. An air conditioning is located on its top which feeds the cabin with tempered air on one side and which is supplied with air from the other side. Inside the cabin, a chamber is the next thermal insulation from the interferometer to the outside. Two water pumps located between the two structures supply the guide field and the spin manipulators inside the interferometer with tempered water. Multiple sensors measure the temperatures at their locations. One of the signals from the sensors can be used to control the air conditioning on top of the cabin.

orientation. After the spin manipulators, the neutrons interact with an analyser, oriented like the polariser. That ratio of neutrons passes the analyser that has the same orientation as the initial polarisation. Mathematically, this is described with a projection between the spin state leaving the polariser and the spin state entering the analyser. Both analyser and polariser of a polarimeter experiment are usually polarising supermirros with different schematic function. Essentially the analyser compares the initially prepared state with the one after some manipulations. At the end of the beam line, a detector is placed measuring the intensity

$$I(\varphi, \vartheta) = |\langle \uparrow | \psi(\varphi, \vartheta) \rangle|^2. \tag{3.25}$$

This is called neutron polarimetry in analogy to light optics.

As the idea is to construct a common-path interferometer with this concept, the spin orientation entering the regime of the interaction of interest, realised by a spin manipulator between the supermirrors, must be carefully chosen. Any orientation can be also described in the basis of a set of spatially antiparallel orientated spins (see Section 2.2). However, the concept of polarimetry suggests especially feasible sets dependent on the interaction studied and its geometrical realisation. The spin state at the entering point to the interaction of interest is chosen as a superposition of equal ratios of perpendicular eigenstates of the interaction. For the final step of this thesis (see Section 5.4), an upward spin orientation is the superposition of forward and backward spin orientations, whose spin states are eigenstates of the interaction induced by the Mashhoon box.

This interferometer technique is insensitive to matter in the beam because any phase shift induced will simultaniously be gathered by both the superposing perpendicular spin states.

Since the single spin states of the interference are required for the adjustment procedure (see Section 5.2), an eigenstate is first prepared to enter the Mashoon box. Specifically, a Ramsey arrangement is used for this purpose: a beam polarised in z-direction is rotated by $\pi/2$ into a superposition of equal ratios of up and down-spins. They undergo the Larmor precession in

the guide field. An interaction of interest dependent on its spin eigenstates is turned on and the spin is rotated again by $\pi/2$ around the same axis, let us assume in the same direction. Without interaction the final count rate is minimal. An additional interaction can change this. Like the phase shifter in interferometry and interferograms, the last spin manipulator can be varied in its rotation angle which results in polarograms. This gives the quality of the spin manipulations in terms of contrast and can be used for interpolation of the sinusoidal phase. If the spin manipulations are systematically added, the intensity at the detector can be converted into the polarisation vector in three dimensions at the exit of the last spin manipulator used.

Chapter 4

Preparations

Prior to writing this thesis, there was already an attempt to measure the spin-rotation coupling in Grenoble. It failed very early on in the measurements due to a leaking water cooler. Also, the few interferograms recorded had a contrast of only about 10 %. The low contrast was a result of dephasing due to the coil design with neutrons passing through copper ribbons required to generate the rotating magnetic field. So following this setback, the whole concept of the Mashhoon box began to be questioned. To produce the water cooler and the coil mounters, 3D printing was used. "Solidworks Education Edition 2016-2017" was used to create the models and an "Ulimaker 2+" as a 3D printer.

4.1 Coil Design of the Mashhoon box

The plan for the second attempt was to create a window for the neutrons in the coil containing nothing but air. The aim was to thereby markedly increase the interferograms' contrasts. The previous coil design was chosen because its field transition is known to be non-adiabatic, i.e. sudden (see Section 4.2), as assumed in the mathematical calculations of Section 2.4. The problem was to find a design with a sudden field transition but without material in the neutron beam.

4.1.1 Helmholtz

The first trial was a design with two separated coil mounters for each field direction above and below the window for the beam (see Fig. 4.1). It was a simple concept, in accordance with the Helmholtz geometry. When testing the coil at the polarimeter, the polarograms could not be made symmetrical (see Section 5.2.1). A similar problem occurs generally when the chosen guide field strength is too low to set a fixed field orientation due to the changing ambient fields. There seemed to be a basic problem with the field characteristics. It may not be homogenious and non-adiabatic enough for this purpose (see the corresponding field simulations of Section 4.2.1) because the dimensions of the coil and wires were inappropriate and strong gradient magnetic fields over the cross-section of the beam were unavoidable. Furthermore, the conducting wires may be to far away from the beam to generate strong field gradients in beam direction to generate a sudden field transition.

4.1.2 Miniature

The second trial was to simply miniaturise the Mashhoon box of Demirel et al., which is 20 cm long and does not fit into the interferometer (see Figs. 4.2 and 4.3). That attempt violated the one

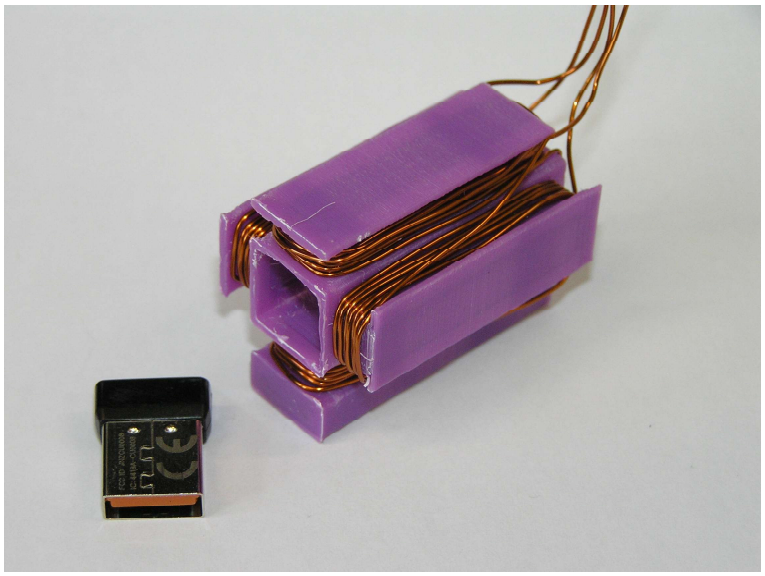

Figure 4.1: Helmholtz design with USB stick for comparison.

basic property of a free window needed to increase the contrast. The idea behind it was to first test the magnetic properties and then deal with making the window free of material afterwards, in the hope the field would not change significantly. The first measurements were satisfying but not complete when an idea for another coil design establishing a window was at hand:

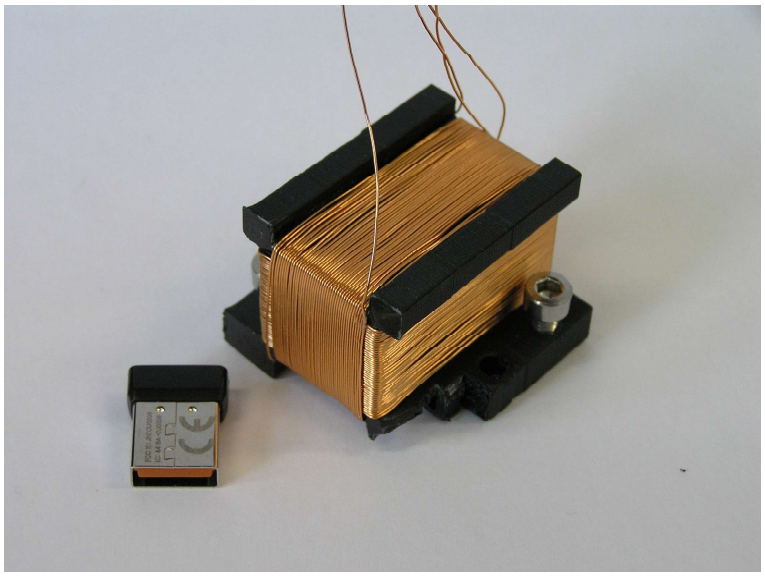

Figure 4.2: Miniaturised Mashhoon box with design of Demirel et al. with USB stick for comparison.

4.1.3 Grooved

To hold the wire in place on the sides of the coil, a multiple of grooves were made (see Figs. 4.3 and 4.4). These confine the positions of the wires on the sides while on the ends they can be wound around the window. This design was tested for a very long time until it could be assured that it suits all the properties required for conducting the desired measurement in Grenoble. Those

measurements on the polarimeter are described in the corresponding Chapter 5.

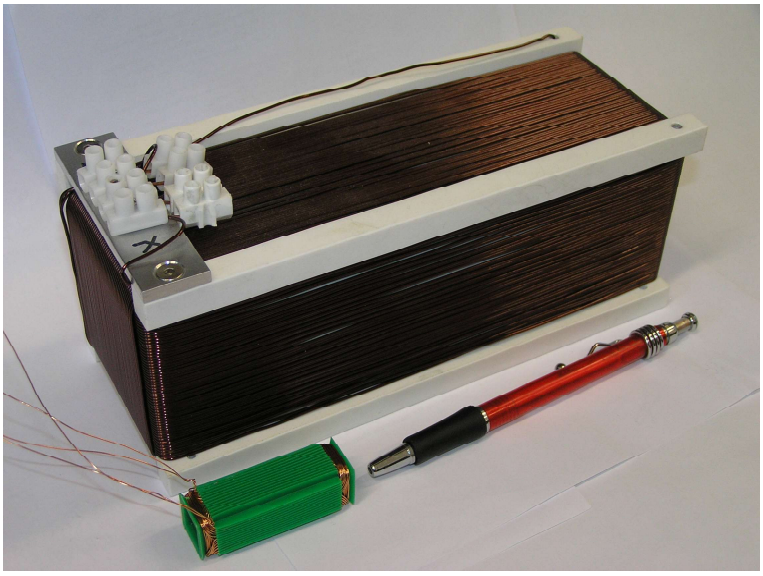

Figure 4.3: Miniaturised Mashhoon box and the previous design of Demirel et al., and with a pen for comparison.

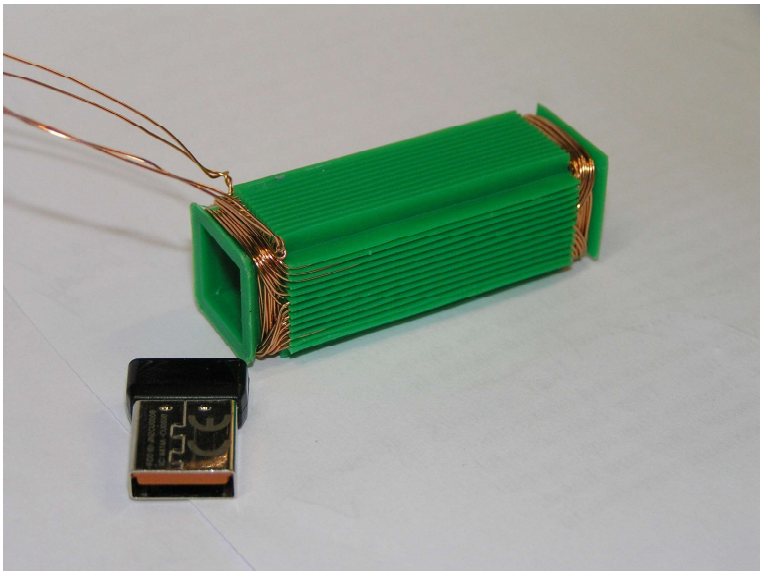

Figure 4.4: Miniaturised Mashhoon box with open window, and USB stick for comparison.

4.2 Field Simulations

For this part, "Comsol Multiphysics 5.3" was used. The software uses the finite element method to approximate physical models. The "Magnetic Fields" module calculates the magnetic flux $\vec{B}$ from Biot–Savart's law

$$\vec{B}(\vec{r}) = \frac{\mu_0}{4\pi} \int_{\text{Coil}} \mathrm{d}\vec{r}' \vec{j}(\vec{r}') \frac{\vec{r} - \vec{r}'}{|(\vec{r} - \vec{r}')^3|}, \tag{4.1}$$

with the position vectors $\vec{r}$ and $\vec{r}'$, the permeability μ_0 and the current density $\vec{j}$. Although the goal is to generate the time-dependent rotating field of Equation 2.26, the qualitative field properties of homogeneity over the beam cross-section in field amplitude norm and direction, and transition characteristics can be simulated in the static case. The quantitative information as to which currents are necessary was determined through the measurements of Chapter 5. Furthermore, only one of the two combined coils, which are wound on the same mounter (inescapably having slightly different geometries), is simulated. A continuous geometry approximating the wire volume of each coil was constructed with "Solidworks Education Edition 2016-2017". The number of single windings in this volume can afterwards be stated to specify the current homogeneity inside. The geometry is therefore altered from the real situation in multiple ways, but because empirical measurements were undertaken as the main method, any short-coming of the model is noticed.

The simulation software requires a plane inside the material to which the electric current is flowing perpendicularly. This means that only an eighth fraction of the geometry was imported into Comsol and mirroring operations using the three symmetry planes of the coil were undertaken to add the missing parts. The information of this full geometry is already implied in the eighth fraction due to the symmetry. However, several attempts of using the appropriate boundary conditions, i.e. "perfect magnetic conductor" and "magnetic insulation", did not yield the same field results. Therefore, the presented results are from simulations with the full geometry without using the symmetry in the calculations.

As the simulation volume, in which the magnetic field is calculated, has to be finite, the dimensions of the simulation volume and there boundary conditions were considered. The boundary surfaces $\mathcal{S}$ of the volume wherein the simulation takes place are assumed to be magnetic insulators which force the relation $0 = \vec{n}(\vec{r}) \cdot \vec{B}(\vec{r})$ with normal vector to some boundary surface $\vec{n}(\vec{r})$ to uphold for all position vectors $\vec{r} \in \mathcal{S}$. To reflect the distinguished direction of the neutron beam with its relatively small cross-section, a cylindric simulation volume is chosen. Therefore, the fields in the vicinity of the coil, positioned in the centre of the volume, are influenced by the longitudinal length l and the radius r of the cylinder and converge with increasing dimensions. The simulation volume was fixed when increases in diameters only marginally changed the results of the fields in the coil at $l = 200\,\text{mm}$ and $r = 80\,\text{mm}$ (see fig. 4.5). At this point, convergence was reached in terms of these qualitative purposes.

All coil types are basically magnetic dipoles. Hence, internal and external field are always pointing in opposite directions. The two main properties constituting the quality of the coils are the homogeneity in their inner region and the suddenness of the transitions. The homogeneity is dependent on the flux norm as well as the flux direction. The centres of the coils are the most homogeneous, as there whole field directions vanish because fields from sources $\vec{r}'_1$ symmetric to sources $\vec{r}'_2$ with opposing amplitudes cancel each other. The transitions into the main field should ideally jump from no field to a constant one. Derivations of real coils to this case can be quantified by the transition length in comparison to the Larmor precession and the peaks occuring in front and after the transition compared to the field at the geometric centre.

4.2.1 Helmholtz

The basic geometry of the first simulated model can be seen in Figure 4.5. The field in the x-z-plane (x-y-plane) in the middle can be seen in Figure 4.6 (Fig. 4.7). Near the coils, the field is much stronger following the square law. The flux norm is roughly constant in the middle of the x-z-plane. In the plot with the field directions, the same area looks quiet perturbed. The field directions are continuously changing in this region. The field in the y-z-plane has also a homogeneous region in the middle of the coil but with good directional adjustment for all the inner region. The field strength for a neutron propagating along the middle of the coil is presented in Figure 4.8. The transition from the inner to the outer peak is about 2 cm long. This is less than one magnitude of order smaller than the Larmor precession length of ~ 10 cm for the usual guide field strengths of ~ 10 G. The Helmholtz geometry implies a large distance between the coils compared to the homogeneous region diameter. A sudden field transition is only easily constructed with wires in the beam's path. The unsuccessful test with this coil type may have its roots in this circumstance as well as the different field directions in the beam cross-section.

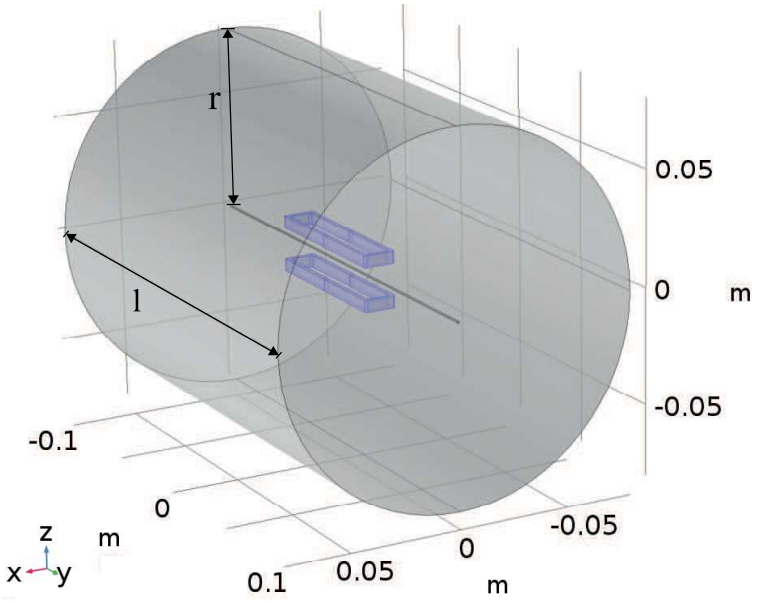

Figure 4.5: Simulated geometry of the Helmholtz coils. The air cylinder in grey and the coils in blue. A line through the middle of the cylinder is implemented to plot the field transition.

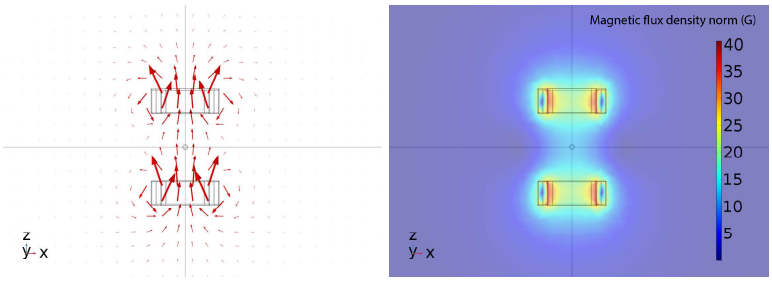

Figure 4.6: Simulated magnetic flux of the centre x-z plane of the Helmholtz coil at some grid points as vector field and in continuous space with flux norm.

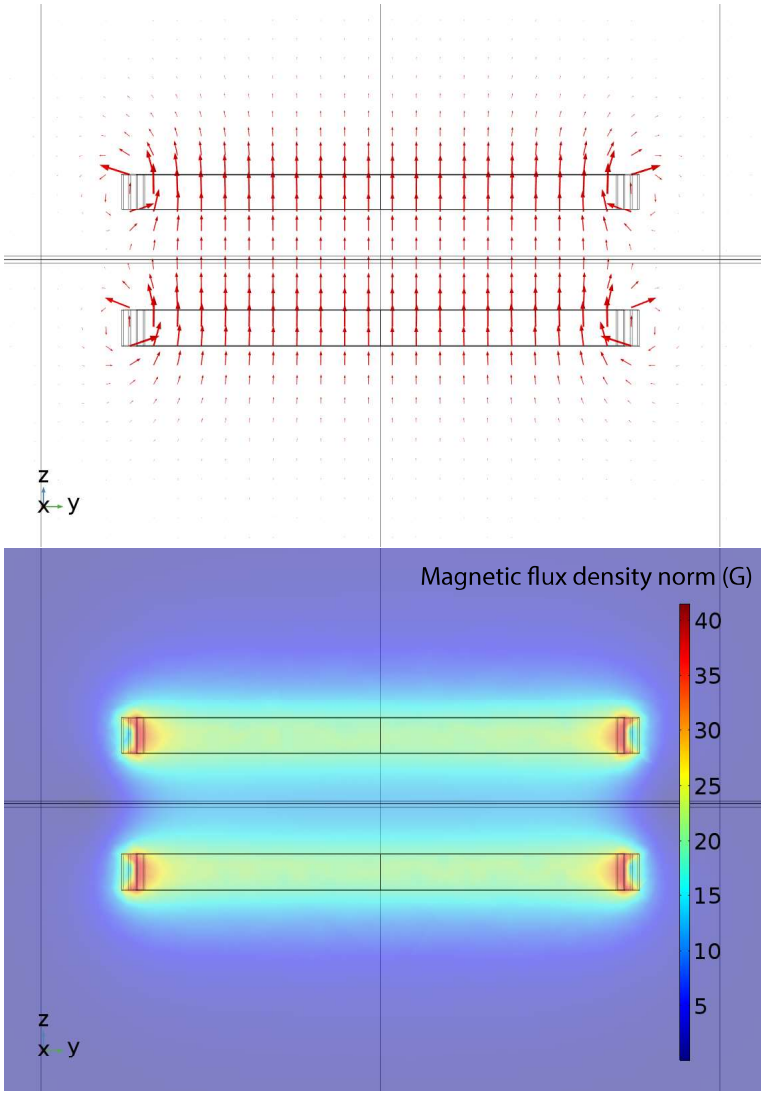

Figure 4.7: Simulated magnetic flux of the centre y-z plane of the Helmholtz coil at some grid points as vector field in continuous space with flux norm.

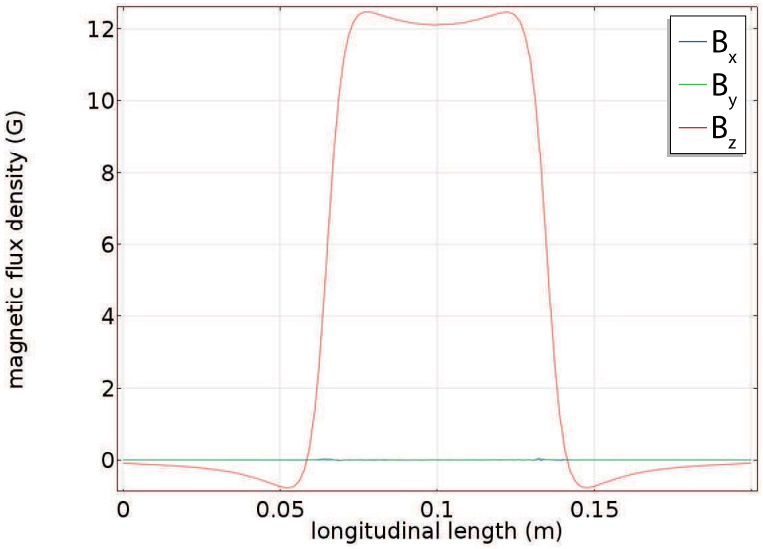

Figure 4.8: Simulated magnetic flux in the optical axis of the Helmholtz coil.

4.2.2 Miniature

Equal field simulations were conducted for the miniaturised design of Demirel et al. (see Fig. 4.9). The directions of the field in the middle x-z-plane are aligned in a larger area compared to the Helmholtz geometry (see Fig. 4.10). The advantage is the sudden field transition (see Fig. 4.12) because of the wires in the beam. The disadvantages are connected to this suddenness: in front and after the transition, the field amplitude changes significantly. Just inside the coil, the field amplitude is 50 % higher than in the centre. Outside the coil, a counter-field of magnitude of the inner field emerges. Also the field direction in the y-z-plane inside the coil (see Fig. 4.11) changes significantly over the beam cross-section. The applicability of this design can be attributed to the suddenness of the transition and the alignment in the inner field's cross-section in the x-z plane.

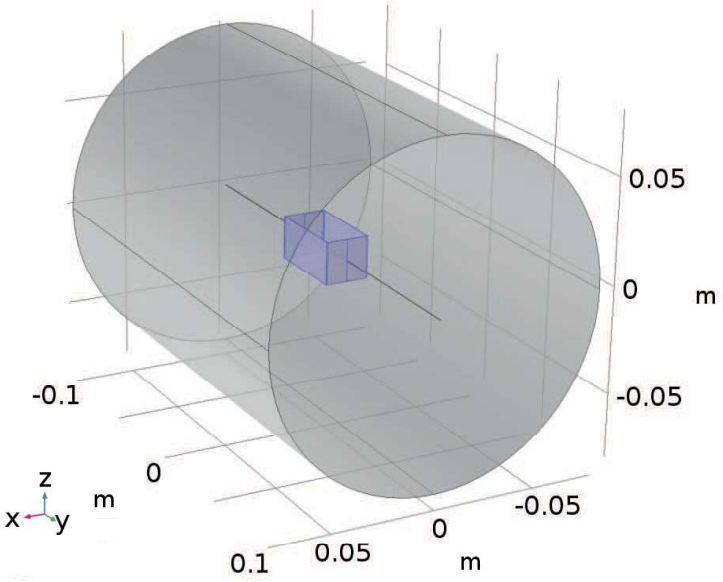

Figure 4.9: Simulated geometry of the miniaturised coil. The air cylinder in grey and the coil in blue. A line through the centre of the cylinder is implemented to plot the field transition on it.

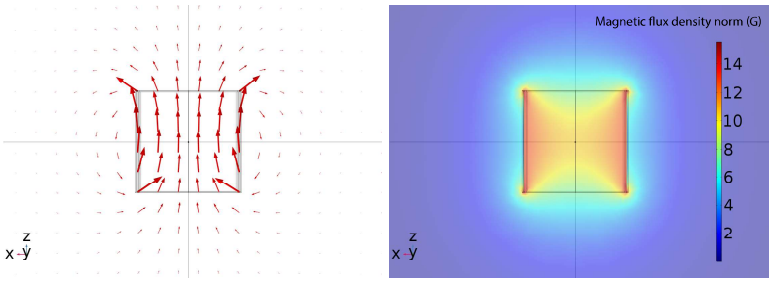

Figure 4.10: Simulated magentic flux of the centre x-z plane of the miniaturised coil at some raster points as vector field and in continuous space with flux norm.

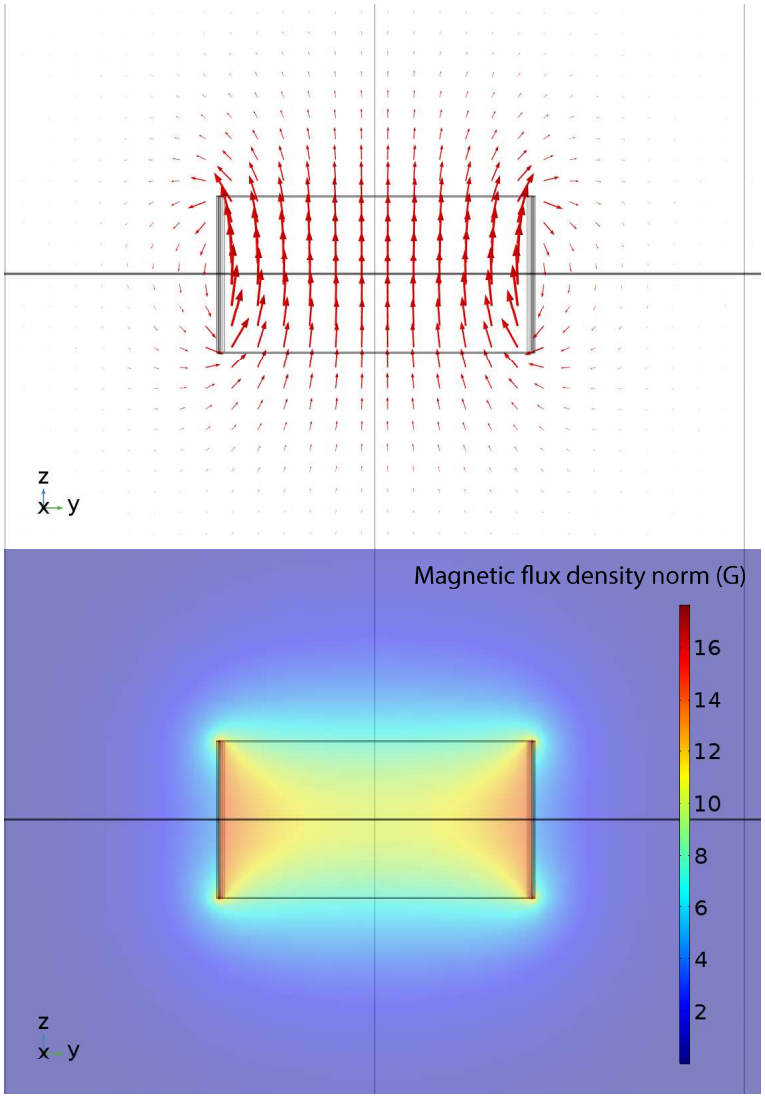

Figure 4.11: Simulated magentic flux of the centre y-z plane of the miniaturised coil at some raster points as vector field and in continuous space with flux norm.

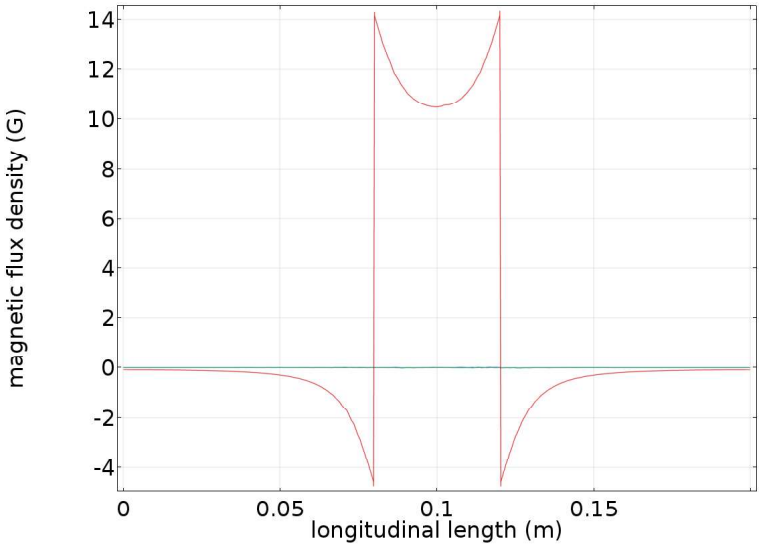

Figure 4.12: Simulated magnetic flux in the optical axis of the miniaturised coil.

4.2.3 Grooved

In the simulation, the grooved coil is split into two halves – one located on top of the windows and one underneath (see Fig. 4.13). Lines were included in the geometry according to the possible paths of neutrons through the field. In the middle of the window, only the desired z-field emerges in the simulation (see Fig. 4.16). The other two field directions are negligible. However, the field transition is in the range of 1 cm. This is, as for the Helmholtz coil, much too long for a sudden field transition. As the measurements showed, there has to be some additional effect to produce the sought effect: the alignment of the field in both planes presented is good (see Figs. 4.14 and 4.15), and seems to be even better for the y-z-plane than for the Helmholtz coils. Also the peaks at the transitions in the optical axis are less than 5 % higher than the minimum inside the coil. So, the high degree of homogeneity may compensate for the long field transition.

Other lines simulating paths of neutrons off the centre show the growing portions of the other field directions in the superposition. The z-symmetry axis of the coil distinguishes a direction in the plane of the beam cross-section. In this direction of the coil, a y-field occurs at the transitions (see Fig. 4.18). In the other spatial direction only deviations of the desired field direction arise (see Fig. 4.17). In the diagonal, both undesired field directions appear visually in the simulations (see Fig. 4.19). From the presented four beam paths, the field characteristics for the whole beam cross-section can be deduced.

A beam with asymmetric cross-section could then be oriented to the distinguished axis to lower the unintentional field strengths. However, as the Mashhoon box has two rectangular coils, in which such a distinguished direction in the cross-section for a beam of the one coil is the other direction for the second coil, this effect cannot be used. In conclusion, a symmetric beam cross-section would be the best option. This is, however, not identical to a symmetric aperture in the interferometer experiment. It seems reasonable, at least for the function of the Mashhoon box, to use an asymmetrical aperture that results in a symmetric beam after the first interferometer plate.

Another idea was to enlarge the coil. The field in the same cross-section would then be more homogeneous. But the space inside the interferometer is limited and the larger the coil, the more current is needed for the same field strength. A small current is prefered. Therefore, the tests were conducted with the present geometry.

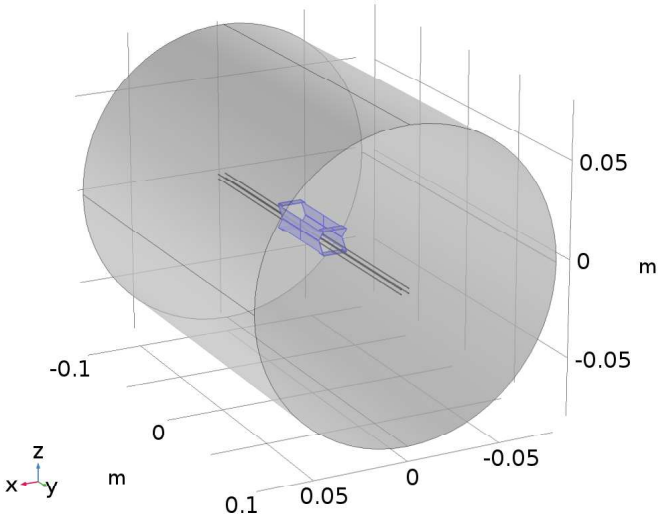

Figure 4.13: The cylindrical volume in which the magnetic fields were calculated and the geometry of the coils in it (blue). Several lines represent possible flight paths of neutrons through.

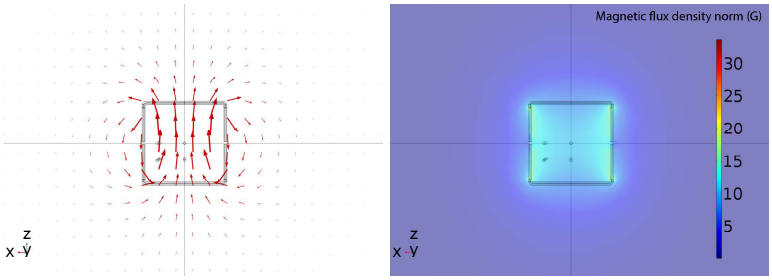

Figure 4.14: Simulated magentic flux of the centre x-z plane of the grooved coil at some raster points as vector field and in continuous space with flux norm.

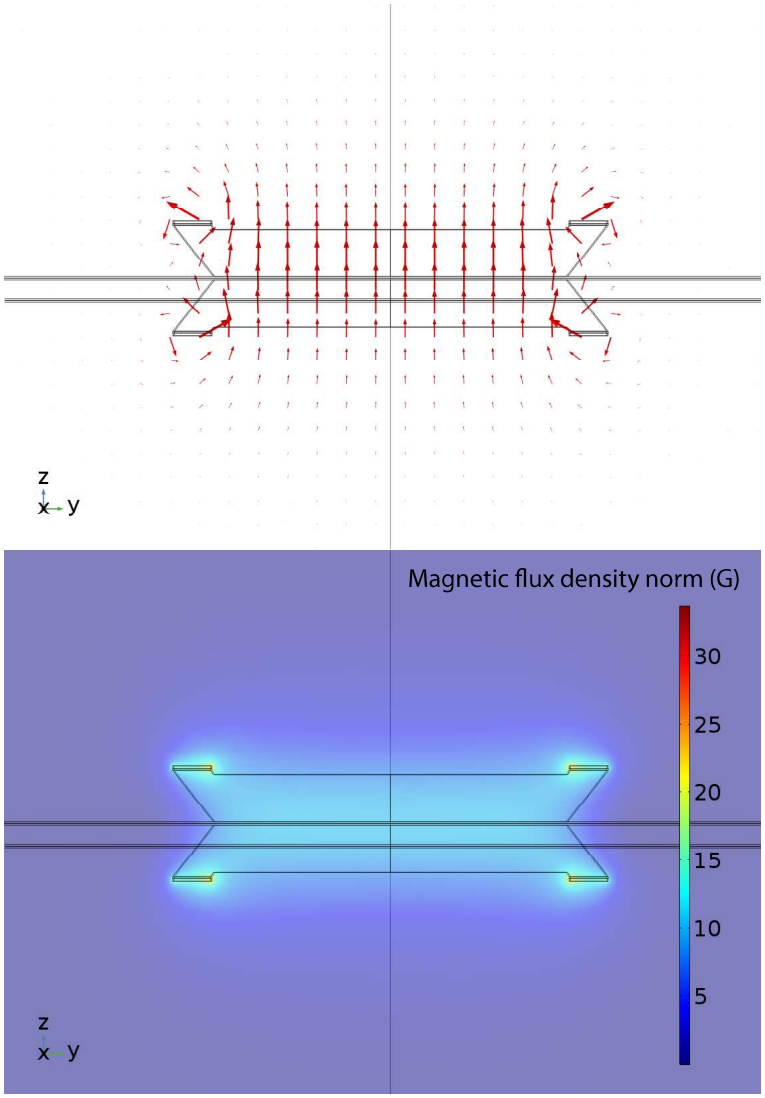

Figure 4.15: Simulated magentic flux of the centre y-z plane of the grooved coil at some raster points as vector field and in continuous space with flux norm.

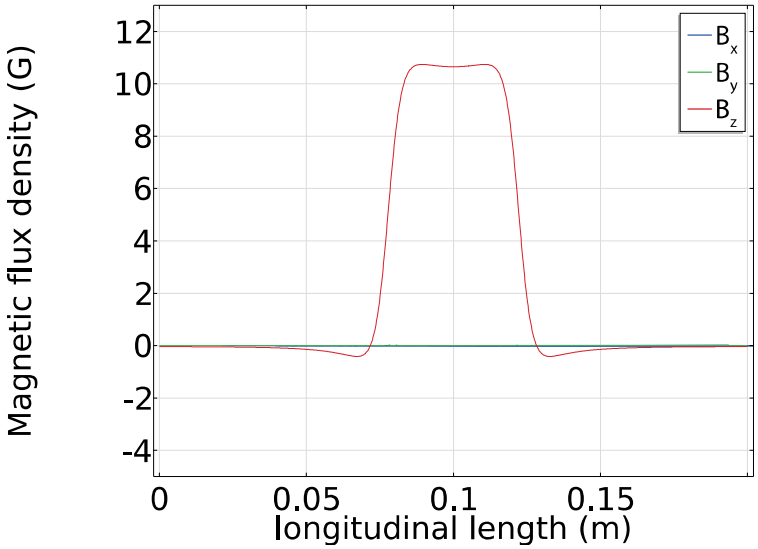

Figure 4.16: Simulated magnetic flux in the centre axis of the grooved coil.

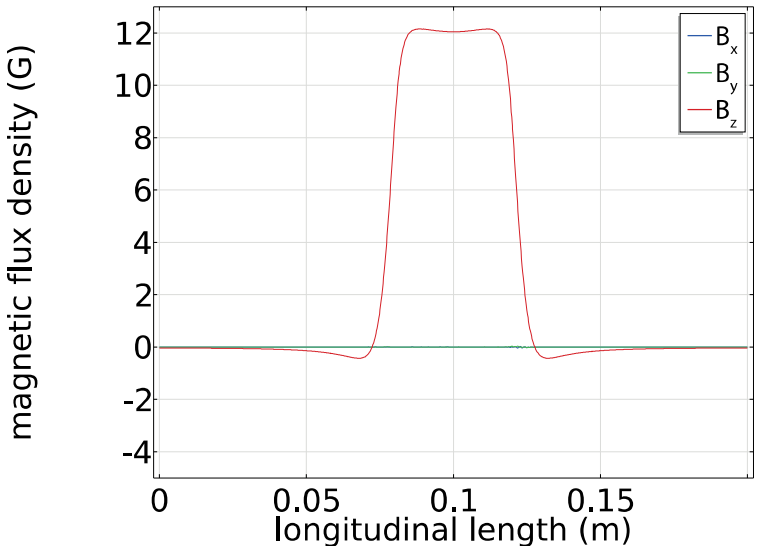

Figure 4.17: Simulated magnetic flux along the path (4 mm, 0 mm) off the centre axis of the grooved coil.

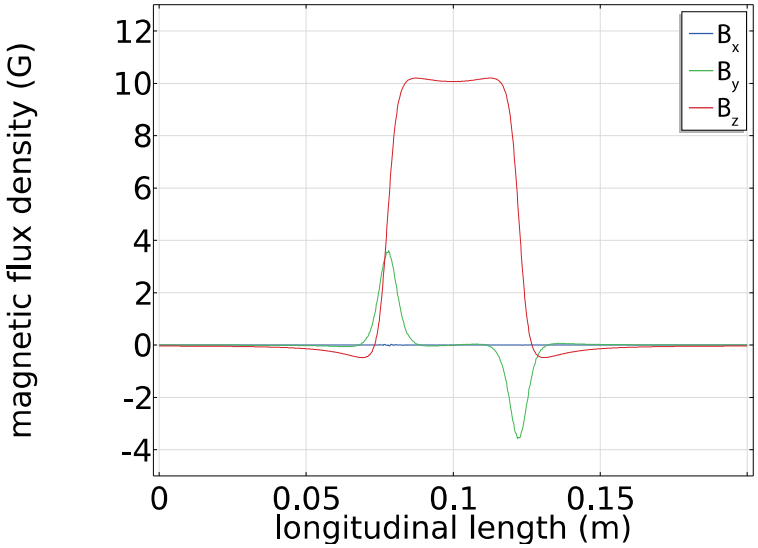

Figure 4.18: Simulated magnetic flux along the path (0 mm, 2.5 mm) off the centre axis of the grooved coil.

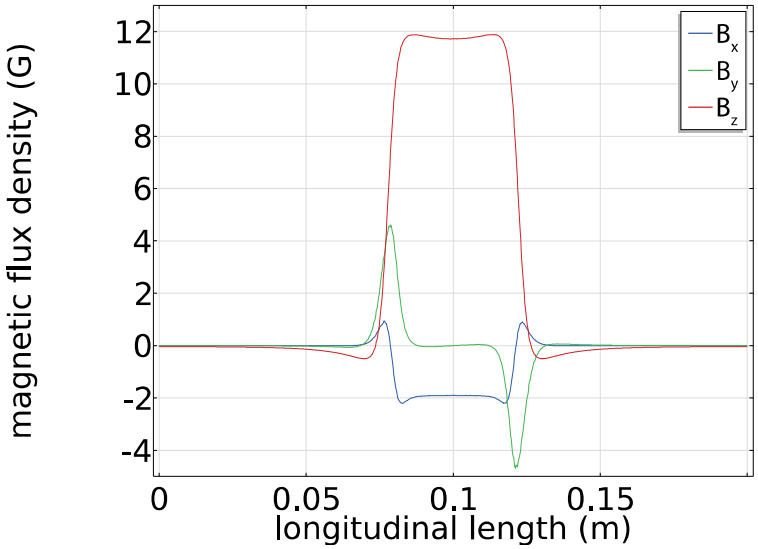

Figure 4.19: Simulated magnetic flux along the path (4 mm, 2.5 mm) off the centre axis of the grooved coil.

4.2.4 Grooved with Small Window

In addition to the promising results of the grooved coil, a slight variation was simulated. The idea for its geometry was already present when the miniature was prepared: a window had to be constructed in order to clear the neutron beam from material. Proper field characteristics were prefered to a larger diameter of the window and an increased neutron flux. In the realisation of the window, it was at first easier to make it as big as the overall cross-section of the coil. In this section, the field simulations for a small window are presented.

The constructed geometry is a mixture of the miniature and the grooved coil with its larger window (see Fig. 4.20). In the presented case, the window's dimensions are 4 mm × 4 mm which corresponds to an aperture adjusted to 4 mm × 1 mm. The results (see Figures 4.21 to 4.26) show a more sudden field transition at the cost of a more inhomogeneous field. Whether the experimental properties are better would have been tested if the grooved coil did not work. Even if the small window would have been better, the difference is not high. The disadvantage of the small cross-section and its reduced neutron flux did not seem worth the attempt to test it when the grooved coil proofed its function and the time of the experiment came closer.

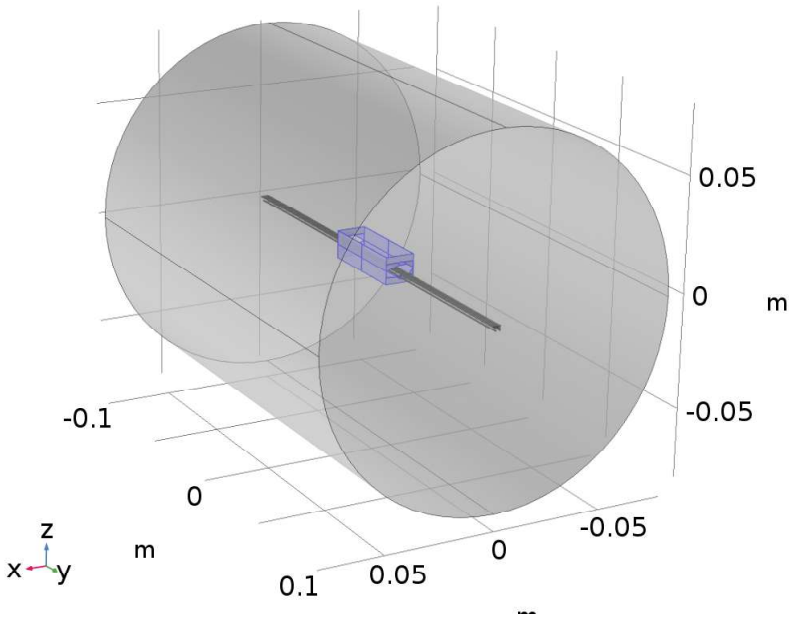

Figure 4.20: The cylindrical volume in which the magnetic fields are calculated and the geometry of the coils with small window in it (blue). Several lines represent possible flight paths of neutrons through the box.

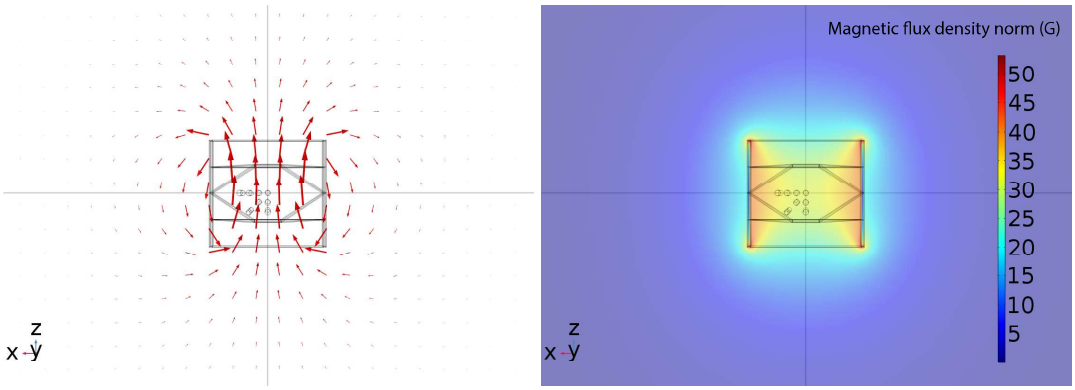

Figure 4.21: Simulated magnetic flux of the centre x-z plane of the coil with small window at some grid points as vector field and in continuous space with flux norm.

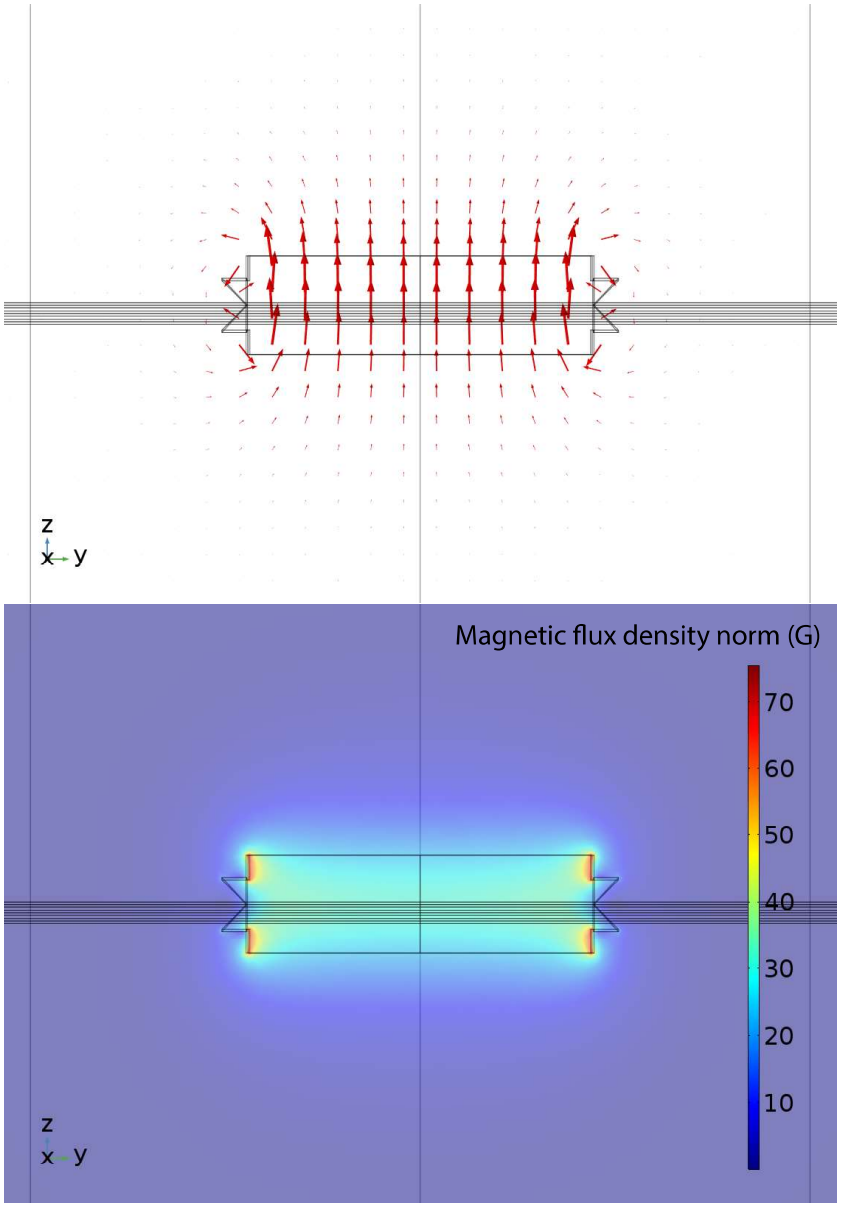

Figure 4.22: Simulated magnetic flux of the centre y-z plane of the coil with small window at some grid points as vector field and in continuous space with flux norm.

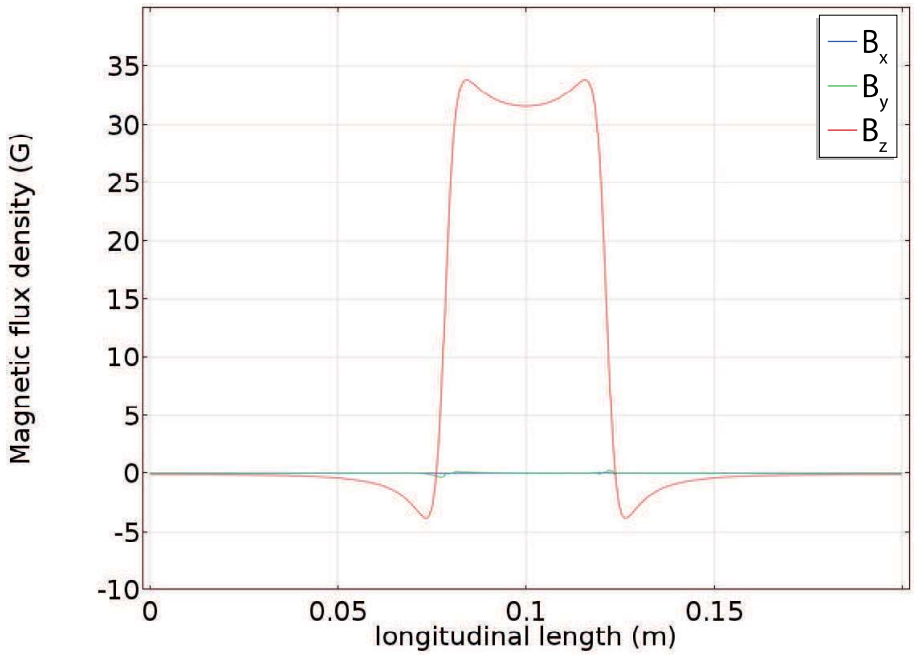

Figure 4.23: Simulated magnetic flux in the optical axis of the coil with small window.

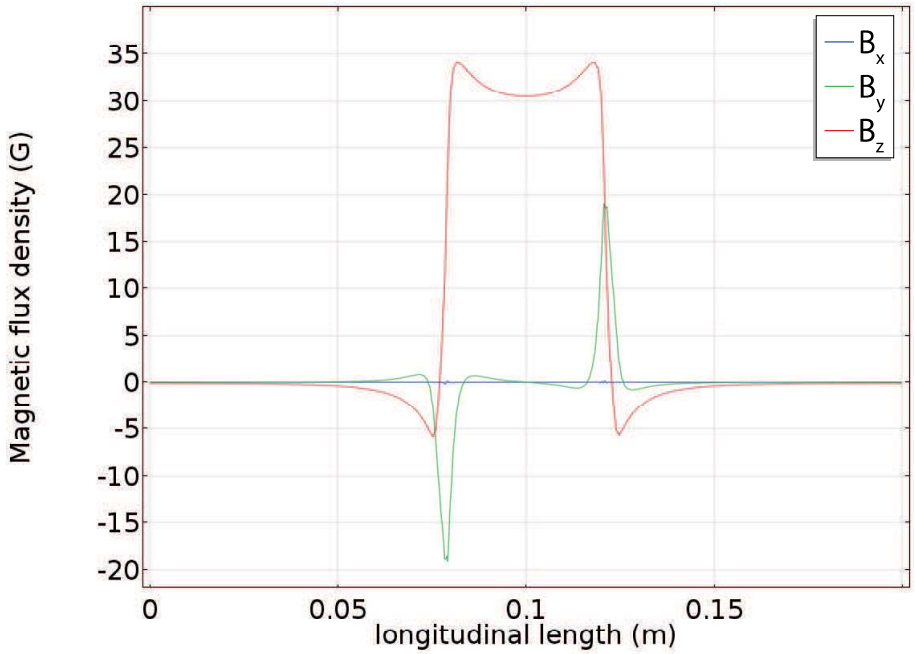

Figure 4.24: Simulated magnetic flux along the path (2 mm, 0 mm) off the center of the coil with small window.

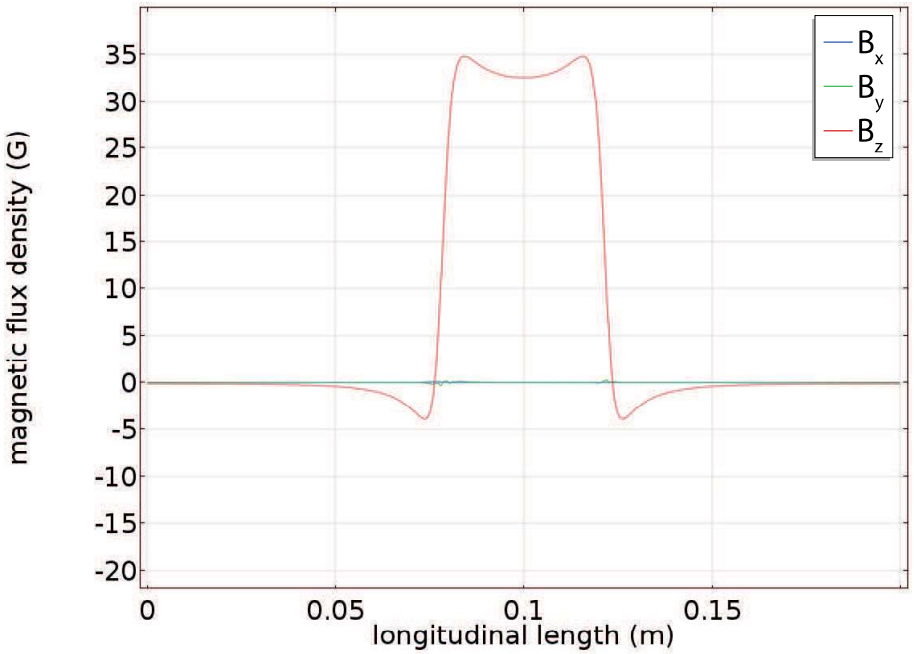

Figure 4.25: Simulated magnetic flux along the path (0 mm, 2 mm) off the center of the coil with small window.

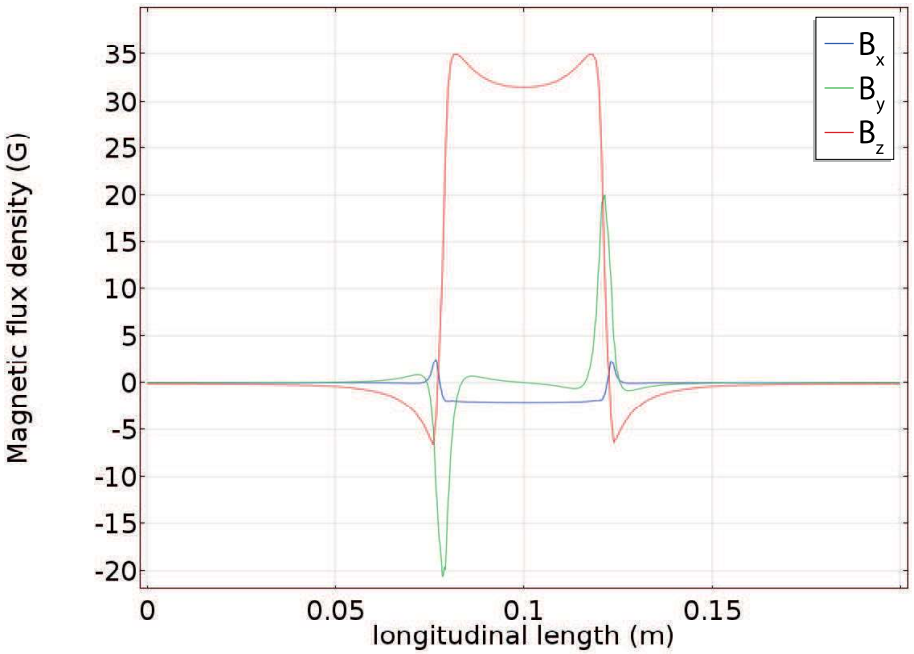

Figure 4.26: Simulated magnetic flux along the path (2 mm, 2 mm) off the center of the coil with small window.

4.3 Water Cooler

The interferometer is very sensible to temperature differences throughout the crystal. Fluctuations can make a measurement impossible if they exceed 0.1 K. As the spin manipulations between the plates depend on electromagnets that have ohmic resistances, without any precautions they will heat the crystal through radiation, heat conduction and convection. The crystal will be heated inhomogeneously, which oppresses the interference pattern through dephasing of the two path states.

To stabilise the measurements, a water cooler for all coils inside the interferometer is necessary. The concept of the water cooler at the previous attempt was complex (see Fig. 4.27), but it most definetly failed due to the inferior technique of connecting the single parts with epoxy resin. Two boundaries between epoxy and acrylonitrile butadiene styrene (ABS) arise where water can reach between and slowly lever them apart. The superior method is to use acetone at those sections of the parts that shall be connected and press the etched surfaced together. The acetone evaporates in time and only one material remains while the etched acetone parts can bind to each other without signified inner glue surface. Although it was only a small problem that ruined the measurements, it hopefully paved the way for a much better second attempt.

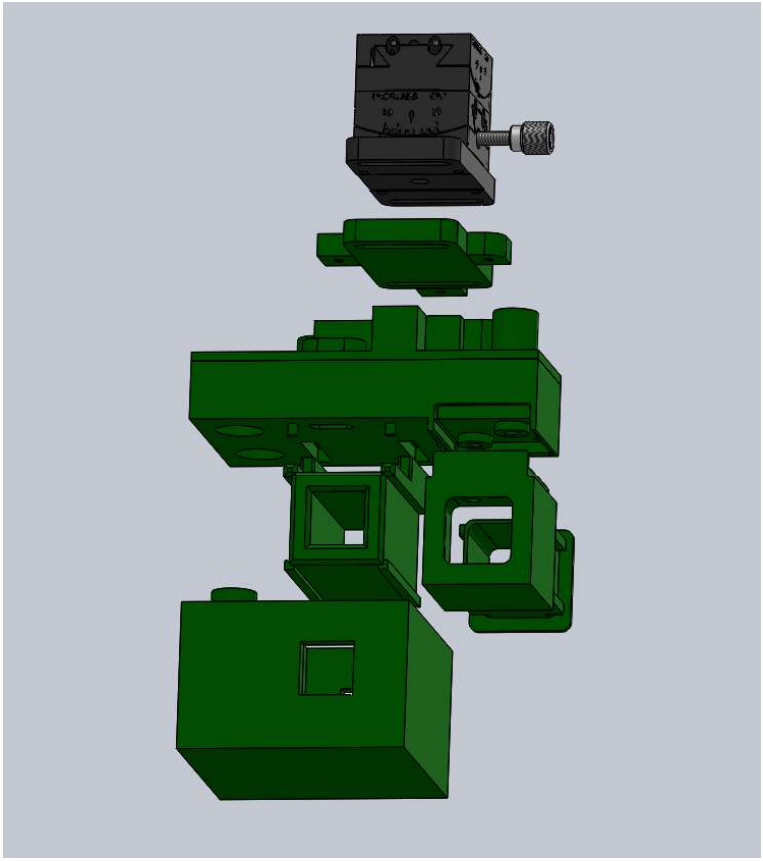

Figure 4.27: Exploded view of the previous water cooler with eight fine glued connections.

As the coil has a window in the new design, the concept for the water cooler also became much easier (see Fig. 4.28): instead of an inner and an outer cooler for the coil, it can now just float in water.

Although temperature stability is not necessary for the polarimeter experiments, the Mashhoon box was placed in a bath nethertheless after high currents deformed two coil mounters made of

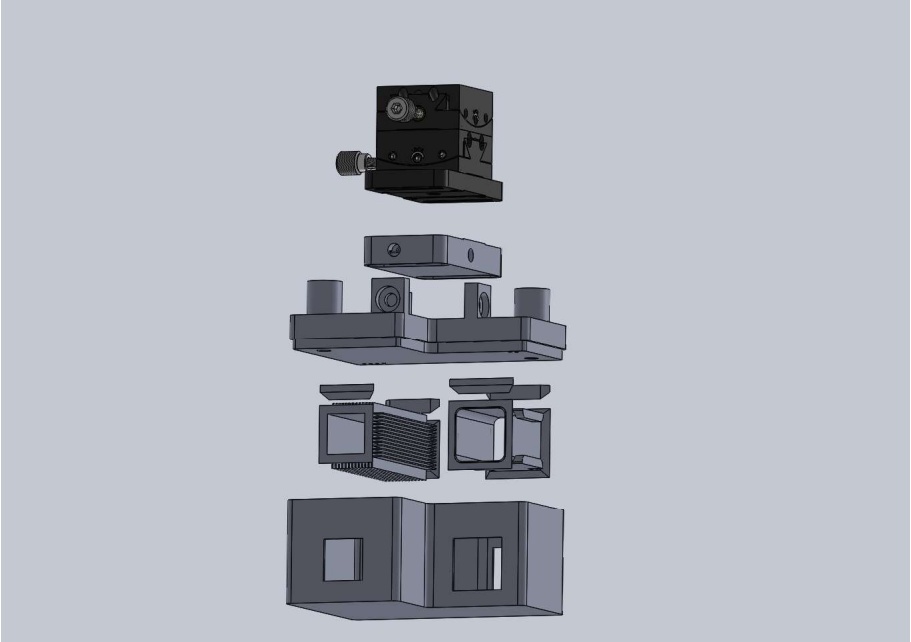

Figure 4.28: Exploded view of the current water cooler design with 5 better controllable connections.

ABS. The deformations hung into the beam and, instead of trying to repair the mounter, a new one was produced; the second time with a water cooler. This was also a test of the concept of the connections between the coil mounters and the bath.

The new concept for the water cooler is basically finished. However, a long term test of watertightness must still be conducted. The acetone etching is well proven through previous measurements and a positive outcome is expected.

4.4 Variable Capacitator

With alternating currents (AC) each coil of the Mashhoon box is part of a resonant circuit. Both coils have roughly the same inductance $I \sim 20\,\mu\text{H}$ and resistance $R \sim 1\,\Omega$. The electrical set-up is shown in Figure 4.29. An amplifier feeds the signal from the generator into the circuit. A capacitator is connected in parallel. Kirchhoff's loop rule translates the configuration in the right loop into the differential equation

$$0 = L\frac{dI}{dt} + RI + Q/C \Rightarrow 0 = \frac{d^2I}{dt^2} + \frac{R}{L}\frac{dI}{dt} + \frac{1}{LC}I. \tag{4.2}$$

The resonance frequency f_{res} follows as

$$f_{\text{res}} = \frac{1}{2\pi}\sqrt{\frac{1}{LC} - \frac{R^2}{4L^2}} \tag{4.3}$$

which is smaller than the one for the ideal case without resistance, $R = 0$. With fixed resistance and inductance, the capacity has to be adjusted to guarantee the resonant case for all frequencies. Otherwise the amplifier may not be able to produce the amplitudes needed. A pair of capacitators was built whose capacity can be changed just by switching single capacitators on and off (see Fig. 4.30). Various combinations can sum up from 7 nF to 7 µF.

The calculated capacities for inductance and resistance as stated above are listed in Table 4.1. These capacities specify the situation where the eigenfrequency matches the outer stimulus from

Table 4.1: From equation (4.3) calculated capacities for the frequencies used.

frequency (kHz)	capacity (µF)
10	10.9
20	3.0
30	1.4
40	0.78
50	0.50

the amplifier. As an example, for the case $f \to 0$ any oscillation would be oppressed by infinite capacity.

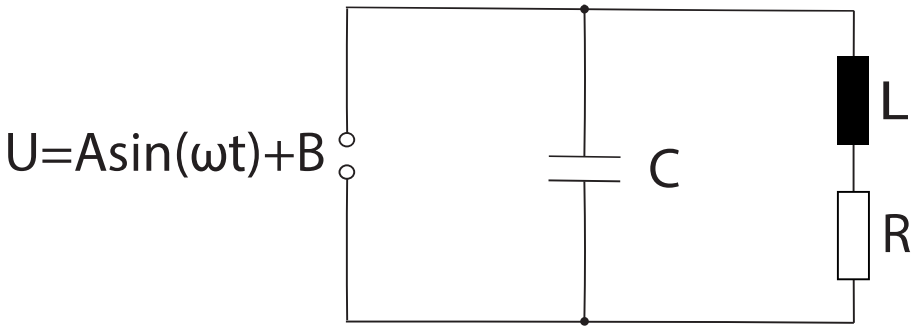

Figure 4.29: The scheme of the electrical circuit with voltage source, capacitator, resistor and inductance. The voltage used is oscillating with amplitude A plus an offset B.

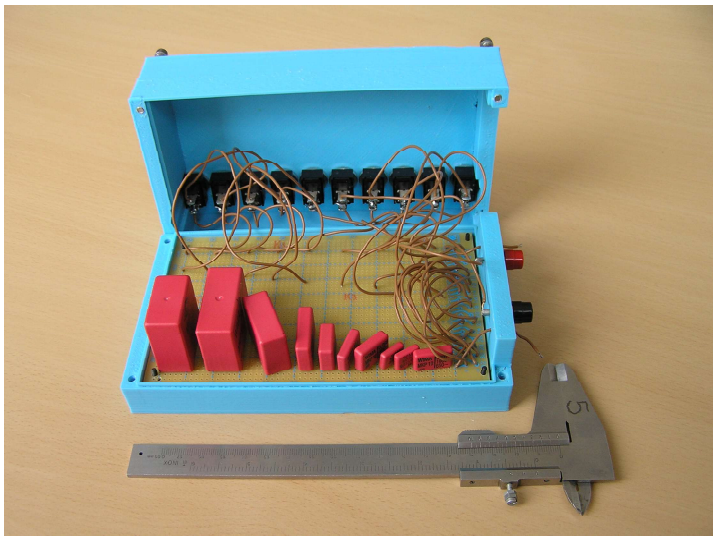

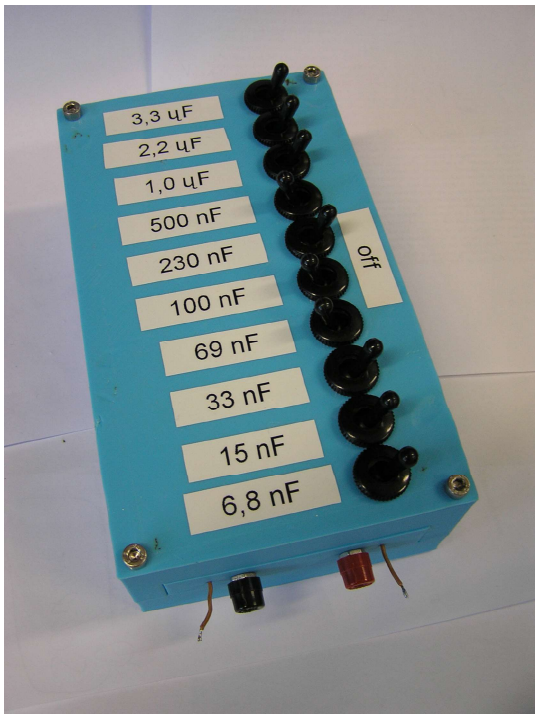

Figure 4.30: On top the inside of the capacitator with switches (black) in the lid and single capacities (red) on the conductor plate, connected via the brown wires. To the right are the connections for electrical circuits (red and black) and for a RLC meter for control purposes (brown wires). The second figure shows the closed capacitor box.

Chapter 5

Measurements

5.1 Concept

5.1.1 Goal

The method used in these measurements is neutron polarimetry. In the first steps, presented in Section 5.2, the following properties of the new coil are characterised: the required currents to induce rotations by π and 2π in the static case, the contrast in the static case, the current to compensate the guide field, the guide field in which the coil works best, and the effectivity of spin manipulations dependent on the field direction and on the initial spin orientation.

But these measurements were performed with the final goal to reproduce the result of Demirel et al. of a spin-rotation coupling phase linear to frequency (see Section 2.7) with the method of neutron polarimetry and a Mashhoon box designed for interferometry. The results of this final set-up are presented in Section 5.4. The intermediate steps to establish the final set-up (already presented in Figure 2.7) are described briefly in the next section and presented in more detail in the Sections 5.2 and 5.3. In the process included is the crucial test of the spin behaviour in one interferometer arm whose results are important for the proposed interferometer experiment.

5.1.2 Set-Up and Short Description of the Experiment

The set-up is as follows: The reactor emits thermal neutrons. The first element at the beam port is a graphite mosaic monochromator. It extracts neutrons with a wavelength of 1.7 Å onto the beamline. As a consequence, all magnetic fields generated on the beamline interact with each neutron for the same amount of time. The next device in the beam used is a polarising supermirror that selects neutrons with up-spins. At its exit begins the guide field that ends at the entry of the second supermirror, which makes an analysation in the same orientation as the first supermirror and which is placed just before the ^{3}He detector. Inside the guide field are two auxiliary DC coils on both its ends and, in between them, an aperture and the Mashhoon box.

The auxiliary DC coils were used in all but the first steps of the measurements. The first auxiliary coil (DC1) in front of the Mashhoon box can change the spin orientation propagating into the Mashhoon box. The second auxiliary coil (DC2) in the rear can change the orientation of the analysed spin orientation. Although the spin orientation is also rotated in the guide field behind the second auxiliary DC coil, this precession does only produce a relative phase between up-spin and down-spin. Therefore, the ratio of neutrons reflected by the second supermirror is not affected by the guide field behind the last coil.

The z-coordinate is defined as the direction of the guide field between the supermirrors with

identical spin orientation selected by the supermirrors. The y-coordinate is the direction of propagation of the neutrons in the beam. The x-coordinate is the remaining direction in a right-handed, orthogonal system.

After the basic properties of the Mashhoon box are determined, the set-up of Demirel et al. is rebuilt in a few steps: one is to supply the coils of the Mashhoon box with AC and a relative phase shift of the currents of 90° to produce a rotating field. With DC1 and the guide field, an eigenstate of the spin-rotation coupling is prepared at the entry of the Mashhoon box. Then the necessary amplitudes of the rotating fields are determined that produce cyclic spin evolutions for different frequencies. The final step, presented separetly to the adjustment procedure, is then to turn DC1 off, which results in a superpostion of the eigenstates of the spin-rotation coupling at the Mashhoon box. The intrinsic spin interference behind the Mashhoon box is measured dependent on the frequency to detect phase shifts induced by spin-rotation coupling.

5.2 Characterisation

5.2.1 Single Coil Installation

Procedure

For the installation of the Mashhoon box, it is placed in the beamline in the middle of the guide field. The window of the Mashhoon box in all presented cases is 12 mm × 12 mm which leaves clearances for the neutron beam of at least 2 mm in both horizontal and vertical direction for all used apertures. The position is checked with a hand monitor. This is a device wherein thermal neutrons initiate a nuclear reaction resulting in the emission of light and that has a spatial resolution in the sub-mm range. The precision of the adjustments of the coils by eye is therefore in the mm-range in this step. Further improvements are not necessary because the resulting error is acceptable for these purposes. An attempt to adjust the position with higher precision is brought forward in Section 5.5.2 but did not improve the adjustment.

The adjustable tilts around the x and y-axes of the Mashhoon box were at first set even to visual judgement. A current is set in one coil of the Mashhoon box to generate a field in the supposed x-direction (see Fig. 5.1). The spin evolution follows Equation (2.17). The counts for a fixed time period are saved and this is repeated for a set of currents that can change the polarisation vector differently. This process of recording count rates with different currents is called a "scan". The term "scanning sth." will be used synonymical for the scan of the according current. The resulting polarogram of the scan should in this case be symmetric around zero current: the sign of the current corresponds to the field direction. For both field directions with same magnetic flux, the polarisation vector will be rotated with opposing but same amount of angles around a rotation axis. If both field directions are perpendicular to the initial polarisation vector, the projection of the final polarisation vector on the z-axis with the second supermirror will result in the same intensities at the detector for both positive and negative currents. But, in general, the coil is not yet well-aligned with respect to the guide field and has to be tilted until symmetry of the polarogram is reached.

For a static field, a specific rotation angle of the spin orientation can be achieved by either changing the time of interaction with the field while the field amplitude is fixed or changing the amplitude of the field while the time of interaction is fixed. Therefore, polarograms are in the case of a static field a representation of the time evolution of the spin orientation that precesses on a circle around the magnetic field on the Bloch sphere because an increased current and field is equivalent to a longer time period in this static field. A sinusoidal fit function describes the

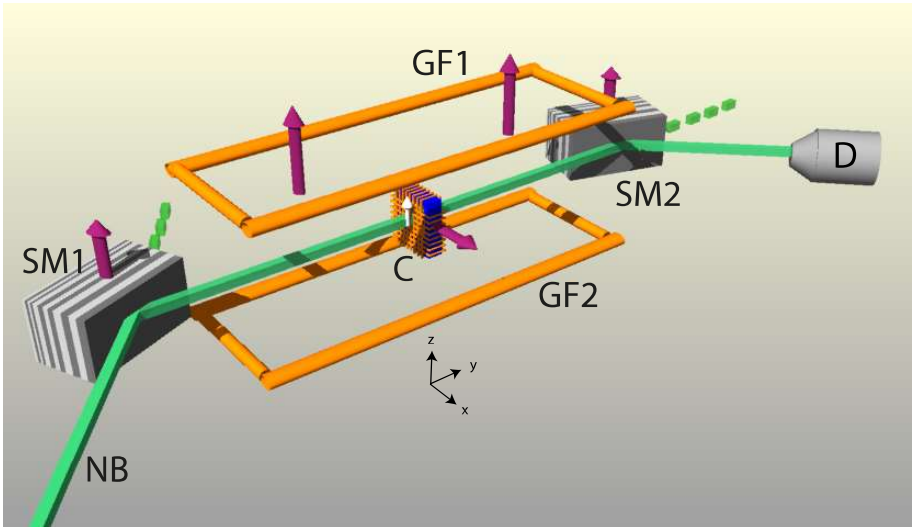

Figure 5.1: The set-up at the beam line for the installation of each coil: neutron beam (NB), supermirrors (SM1 and SM2), the detector (D), coils of the guide field (GF1 and GF2), the installed coil (C), effective local magnetic fields (purple arrows), the orientation of the polarisation in front of the installed coil (white arrow). Neutrons with a wavelength of 1.7 Å propagate to the first supermirror to the left. It reflects only neutrons with up-spin state that enter the region of the guide field. Neutrons with down-spins are transmitted by the supermirrors (dashed beams). The beam of reflected neutrons enters the installed coil in the center of the guide field and those neutrons with up-spins at the second supermirror are reflected towards the detector. All coils are installed near the middle of the guide field.

polarograms mathematically (e.g. Fig. 2.8). Its phase shift to the case of a sine is a measure for the symmetry of the polarogram. If it is below 2° apart from the symmetrical cosine value of 90°, the coil can be considered to be adjusted. Further improvements of the phase shift towards symmetry can be done, but are reduced in their validity because other errors in the count rate (see Section 5.5.1) become more significant compared to the tilt of the coil. Another, correlated, measure for the symmetry is the ratio of intensities in the minima. The minima represent the situations where the polarisation vector is rotated furthest towards the negative z-direction. Ideally, the supermirror should then not transmit any neutrons and the count rate be zero. The minima in real situations are off the value of zero count rate. The first reason are scattered neutrons: some amount of detected neutrons comes from different directions than the pronounced beam. Free neutrons are present everywhere in the reactor hall where the experiment takes place and can reach the detector. This is called “background”.

The second reason is the efficiency of the supermirrors: they can separate the two spin states only imperfectly. While the higher number of neutrons with up-spins are turned into down-spins by the magnetic fields of the minimum count rates, the smaller number of down-spins is turned into up-spins that are likely to be reflected by the second supermirror towards the detector. The efficiency of polarisation of the employed supermirrors is $> 90\,\%$. If we assume only neutrons from the beam present at the detector, the efficiency of the supermirror is equal to the contrast of a perfect spin manipulation. All real manipulators have additional losses in contrast because no real spin manipulator has a perfect efficiency of $100\,\%$.

The third reason for a reduced contrast can be the guide field: The fields generated in the first scan superpose with the guide field to a vector in the x-z-plane. But only if the field is solely in x-direction, the polarisation vector can be purely rotated into the downward direction (called

"π-flip"). In the scan, the minima only represent those directions of the polarisation vector closest to the downward direction. But because of the guide field, the polarisation vector does not evolve on a great circle and cannot reach the down-orientation. In order to realise evolutions on great circles, the superposing z-field from the guide field has to be compensated. This is accomplished by first setting the x-current for the minimum in count rate of the first scan while scanning the current in the perpendicular coil (wound on the same mount) that generates a z-field. Scans of this z-field superposed with the x-field of the minima of the first scans have only one minimum in the count rate. All other currents either strengthen, undercompensate or overcompensate the guide field. The asymmetry of a scan of the compensation current represents the distinguished direction of the guide field. Naturally, the additional compensation field is also generated by a spin manipulator with an imperfect efficiency. The compensation is therefore only used if the contrast gained is high compared with the additional imperfections. This is almost always the case. It is called "compensation" when a coil is supplied with a current that compensates the guide field locally.

With the compensation determined, the x-current for the minimum of a π-flip has to be scanned once more but this time with compensation because the originally determined current produced a Larmor precession in combination with the guide field. The amplitude of their superposition generated a rotation of π around the field. This rotation angle results only from the combination of the neutron's magnetic moment and the field strength regardless of their directions. Their orientations determine which circle the spin orientation precesses on. After the compensation current is determined, the same field amplitude for a π-rotation in the Mashhoon box has to be produced only with the x-field that needs to be a certain amount larger than previously. Although one could calculate the necessary current with the first two measurements, it is empirically determined with measurements. As a result, a polarogram with deepened minima takes shape. The ratio of maximum and minimum intensity is a measure for the quality of the coil's spin manipulation for a fixed degree of polarisation. The currents producing half the intensity correspond to a $\pi/2$-rotation, minimum intensity corresponds to a π-flip, and a recurrence of the full intensity, the 1^{st} side maxima, correspond to a 2π-rotation.

The compensation current depends on the guide field at the location. To see which guide field strength is ideal for the Mashhoon box design, the guide field strength is varied and the contrasts of the respective polarograms are compared. As the Mashhoon box will, for the interferometer measurements, always be operated simultaneously to the DC coils, a restriction arises: the DC coils work best at a guide field of 13 G but can be used in a wider range of field strengths with good performance. However, below about 7 G their efficiencies become lower very fast. So, the Mashhoon box's efficiencies are compared only above this threshold.

With the guide field strength fixed at the value of highest contrast for the Mashhoon box, the two auxiliary DC coils are installed at a location near the middle of the guide field with the same procedure. At the ends of the guide field, the increasing influence of the supermirrors would make the process of installation more difficult.

Results

First, a Mashhoon box of Helmholtz geometry (see Section 4.1.1) was tested with a symmetric aperture of 8 mm × 8 mm. However, the polarograms could not be made symmetrically. From a multiple of attempts, the best result with a phase shift of more than 6° is shown in Figure 5.2.

The second geometry used was the miniature (see Section 4.1.2). It produced symmetric polarograms. Different symmetric aperture diameters of 4–8 mm were tested in a guide field of 13 G with contrasts from 52–63 % (see Fig. 5.3). The contrast declines with smaller aperture. After

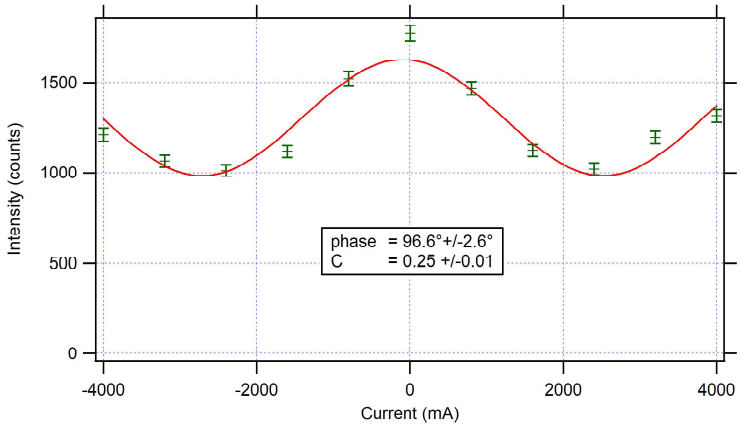

Figure 5.2: Data points and sinusoidal fit of the most symmetric polarogram achieved with the Mashhoon box with Helmholtz geometry. The inlet contains fit parameters. The phase shift is still $>5°$.

these first steps, the coil geometry was changed.

The third geometry tested was the grooved coil. Presented in Figures 5.4 and 5.5 are the single steps of the installation of the Mashhoon box of this type. The initial contrast in the case of symmetry is 24 % (see Fig. 5.4b). The compensation of the guide field of 9 G is reached just above 600 mA (see Fig. 5.4c). The contrast with compensation is initially > 70 % at a guide field of 9 G showing better results than other guide field strenghts (see Fig. 5.5b). Because after this step the Mashhoon box got heavily deformed, the measurements got repeated with 9 G resulting in the presented higher contrast of 77 % (see Fig. 5.5a). The minima are at approx. 750 mA. A scan expanded to the first side maxima of rotations by 2π is presented in Figure 5.5c for a guide field of 9 G. The side maxima in this scan are almost as high as with zero current.

The same sequence of installation was performed for the DC1 and DC2 in a guide field of 9 G. Their main results are presented respectively in Figures 5.6 and 5.7. Their compensation currents are approx. 300 mA and their respective contrasts are 80 % un-compensated and 86 % compensated. The current necessary for a π-flip is approx. 1200 mA and for the half intesity of a $\pi/2$-rotation approx. 600 mA. The $\pi/2$-rotation is used in all but the last succeeding steps (Sections 5.2.2 to 5.3).

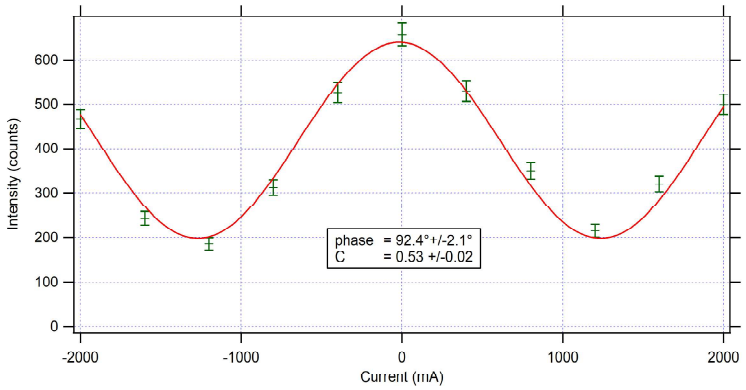

(a) Scan of the x-field in the miniature with 4 mm × 4 mm aperture and a measurement time of 75 s per data point.

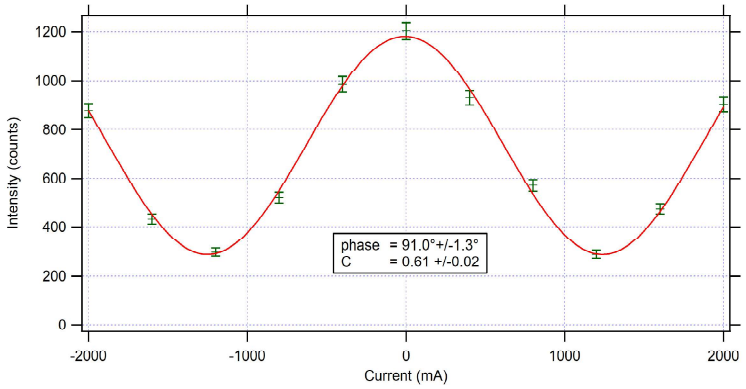

(b) Scan of the x-field in the miniature with 6 mm × 6 mm aperture and a measurement time of 75 s per data point.

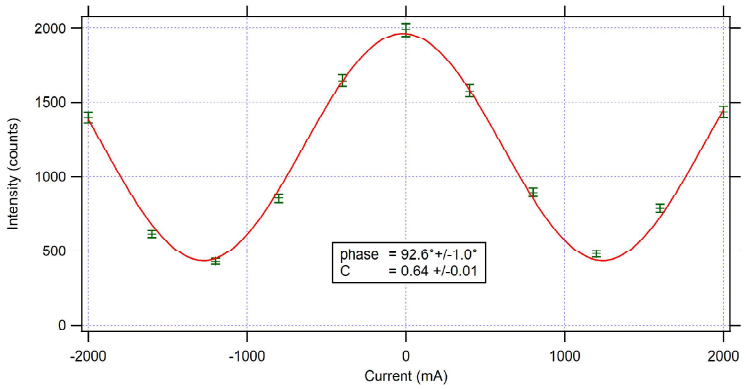

(c) Scan of the x-field in the miniature with 8 mm × 8 mm aperture and a measurement time of 75 s per data point.

Figure 5.3: Polarograms and sinusoidal fits of the miniature with different apertures and a guide field of 13 G. The inlets contain fit parameters.

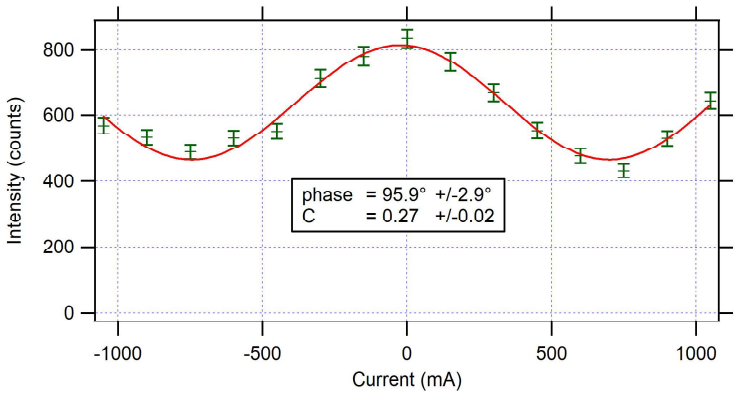

(a) Asymmetric scan of the current in the x-coil when it is not yet properly tilted with respect to the guide field.

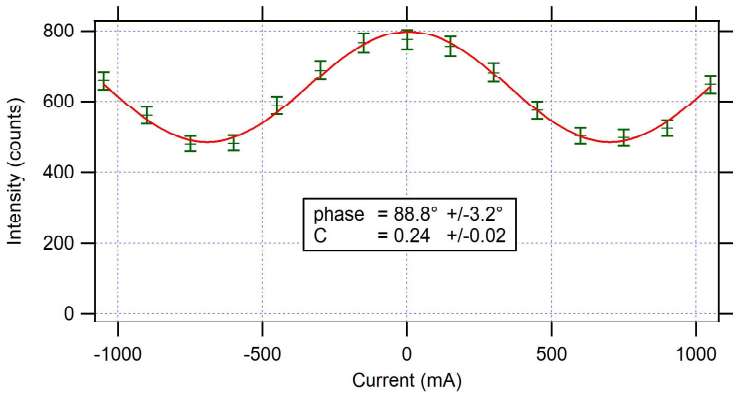

(b) Symmetric scan of the current in the x-coil with adjusted tilt of the coil. The contrast is about 24 %.

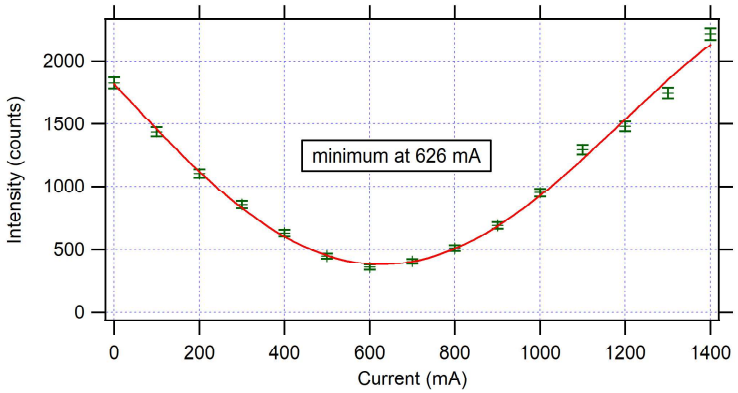

(c) Scan of the current in the z-coil for compensation of the guide field of 9 G with a minimum just above 600 mA.

Figure 5.4: First steps in the installation of the grooved Mashhoon box.

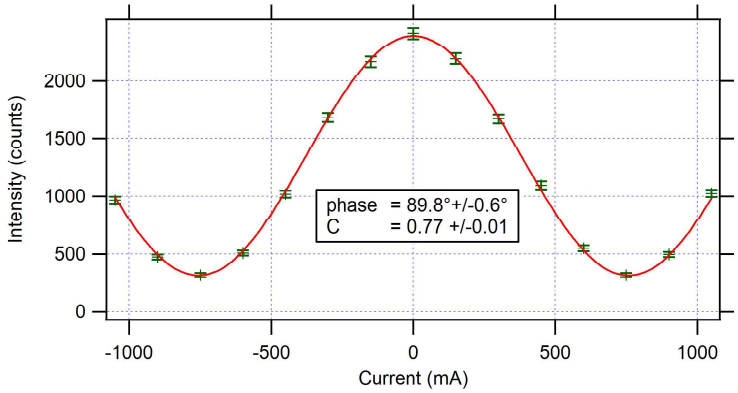

(a) Scan of the current in the x-coil with 9 G guide field compensated. The compensation decreases the minimum count rates and increases the contrast to about 77 %. The minima of the π-flip are at about ± 750 mA.

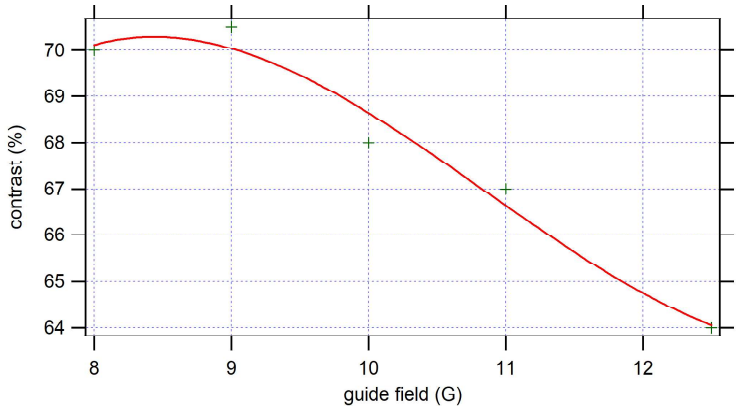

(b) Contrasts for different guide field strenghts compensated and fitted with a polynomial of 4^{th} order. The highest contrast is reached at 9 G.

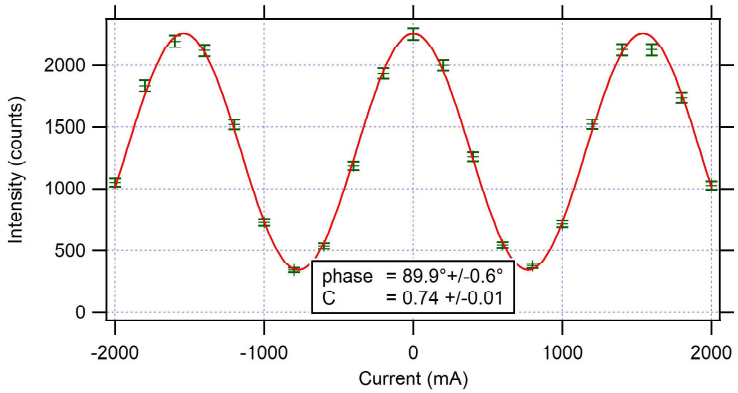

(c) Similar scan as in Figure 5.5a with higher currents scanned. The first side maxima are almost as high in intesity as the 0^{th} maximum which is a sign of quality of the spin manipulation.

Figure 5.5: First results of the grooved Mashhoon box.

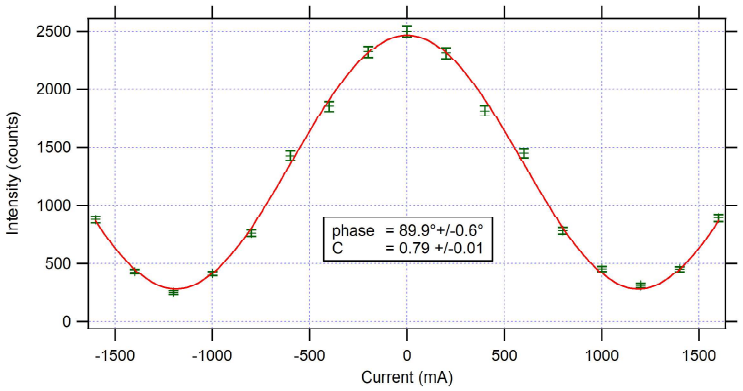

(a) Symmetric scan of the current in the x-coil with a contrast of about 80 %.

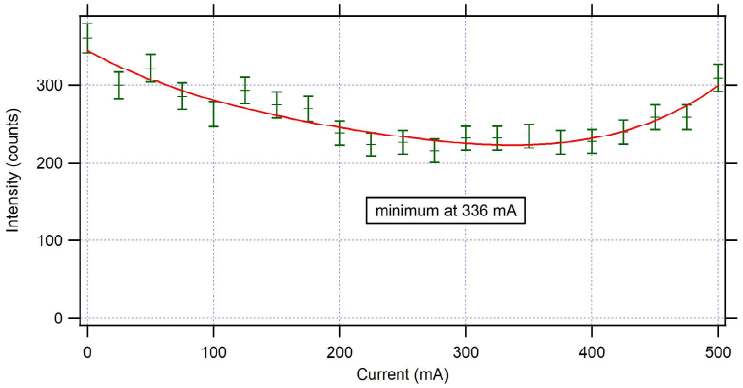

(b) Scan of the current in the z-coil for compensation.

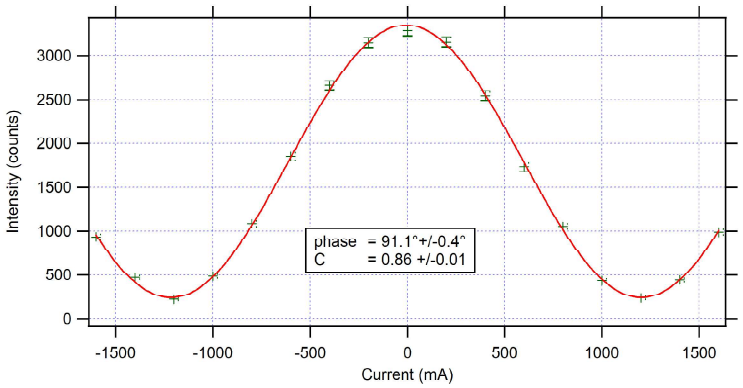

(c) Scan of the current in the x-coil with guide field compensated.

Figure 5.6: Main results of the installation of the coil DC1.

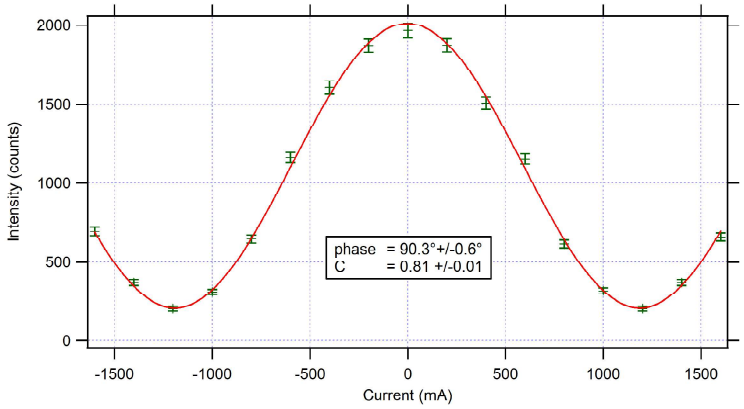

(a) Symmetric scan of the current in the x-coil.

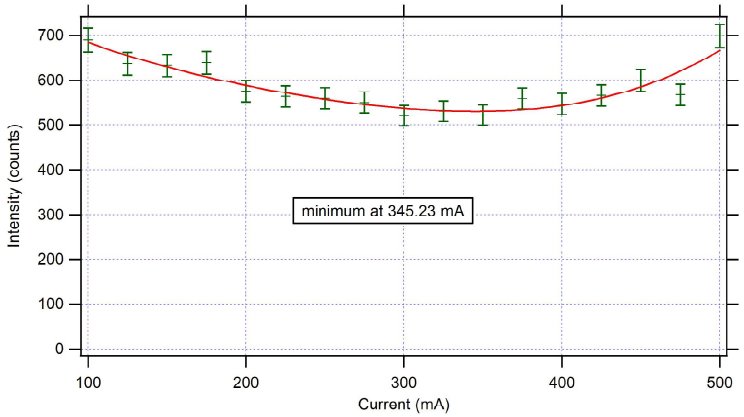

(b) Scan of the current in the z-coil for compensation.

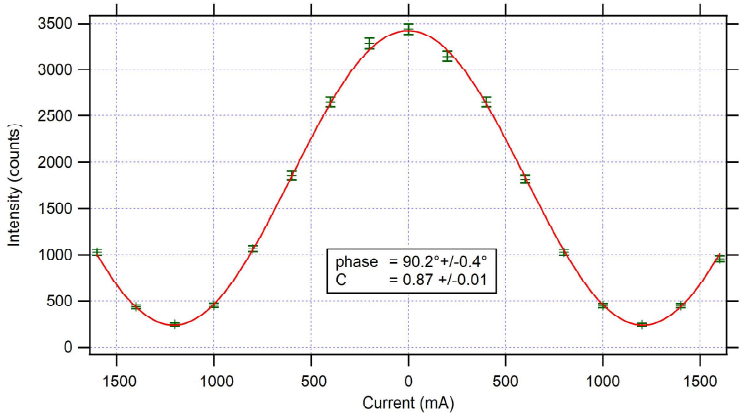

(c) Scan of the current in the x-coil with guide field compensated.

Figure 5.7: Main results of the installation of the coil DC2.

Discussion

As presented in Figure 4.6, the field of the Helmholtz coil is inhomogeneous over the cross-section of a beam. To guarantee symmetry of polarograms, the coil has to be centered very accurately around the beam. Even for a small aperture, the missing symmetry in all scans suggests that the adjustment misses the precission to do so.

With the miniature, the higher contrast for a bigger aperture is surprising. Usually, the field inhomogeneities become higher with a higher beam cross-section. As the homogeneity is very good for this coil type (see Fig. 4.10), the rising countrate of the higher cross-section may outweight the disadvantages of the rising inhomogeneities by reducing the ratio of the background to the total count rate.

The auxiliary DC coils are very similar. Their contrasts with and without compensation are higher than the Mashhoon box's. The difference of the contrasts to unity are due to the degree of polarisation and the coil's efficiencies. The DC coils are constructed for conducting manipulations in the polarimeter while the Mashhoon box, designated for the interferometer, has more restrictions implemented in the design (see Sections 4.1 and 4.3). This allows the diameters of the auxiliary coils to strech far over the beam cross-section. Therefore, at the beam, the generated magnetic field is much more homogeneous than the field of the Mashhoon box, whose geometry is confined tightly to the beam. Therefore, the auxiliary coils have a higher level of contrast.

The polarograms' contrasts of the auxiliary DC coils gain only about 5 % with compensation of the guide field. The Mashhoon box is twice as long as each DC1 and DC2. On this longer distance, the rotation of the polarisation vector by a specific angle is realised with a smaller field amplitude. Thus, the superposition with the guide field can result in a significant angle between the composed field and the x-axis and therefore reduce the contrast. Hence, the compensation can increase the contrast far more for the longer geometry of the Mashhoon box. A tripled contrast, though, is surprising: if the situation without compensation is considered, the π-flip additionally intended with the x-field is performed on the distance of 4 cm which are about half a Larmor precession of the guide field of 9 G on 8.87 cm (see equ. 3.20). Both fields should superpose with their similar amplitudes to an angle of 45° towards the x-axis. Thus, the contrast has an upper limit of $\sin(45°) = 1/\sqrt{2} \approx 0.707$. A smaller portion of the difference to the result of 26 % contrast is due to the imperfect degree of polarisation. The bigger portion is accounted to by unknown sources.

Because the auxiliary DC coils have about 45 windings while the Mashhoon box has 24 for each coil, their necessary currents for the compensation of the guide field are separated approx. by a factor of 2.

Looking at the field simulations for the Mashhoon box in Section 4.2.3, the higher contrast for weaker guide fields and their spatially longer Larmor precessions is plausible because the field transition length of about 1 cm (see Fig. 4.18) has to be compared to the length for a full Larmor precession in order to evaluate its suddenness. For small field strengths, the ratio of the field transition length to the length for a full Larmor precession length is reduced and the suddenness is more pronounced. The decline in contrast below 9 G guide field is not plausible. The simulated field transition is almost one order of magnitude below the Larmor precession. Another order of magnitude would suffice to assume a sudden field transition.

In the expanded scan of Figure 5.5c, the similar height of all maxima is a sign of good quality of the spin manipulation

5.2.2 Auxiliary Coils in Combination

Procedure

After all coils are installed, this step combines both auxiliary coils. The procedure of this step is only a preliminary for the results of the next Section 5.2.3 where all coils are used simulataneously and additional effects of the the Mashhoon box are evaluated.

Both auxiliary DC coils are set to produce $\pi/2$-rotations. The first one (DC1, placed at the beginning of the guide field) transforms the polarisation vector to be parallel or antiparallel to the beam direction. In the guide field, this polarisation vector is rotated through Larmor precession. Depending on the position of the second coil, DC2, the intensity at the detector oscillates. The position of the coil DC2 is chosen at the end of the guide field such that a minimum count rate is obtained with the detector (see Fig. 5.8). A maximum could be chosen as well, but for low intensity the absolute error is smaller due to the Poisson distribution of neutrons and the intended extremal count rate can be identified with higher precission. Both fields of the DC coils are parallel which is confirmed with a magnetic probe. This means that after the first coil, either the polarisation vector is parallel to the beam direction and gets to the second coil the same way before it is rotated into a downward orientation, or it is rotated by DC1 into an antiparallel orientation which is the same orientation as in front of DC2 which rotates the polarisation vector into a downward orientation. Either way, a $2\pi n$ Larmor precession occurs in between the two, with an integer n. The compensation of all coils has to be re-adjusted, as their positions compared to their initial positions of installation are changed in this procedure. With the fixed currents in DC1, DC2 is scanned in its x-field to create a reference polarogram for the additional effects of the Mashhoon box presented in Section 5.2.3].

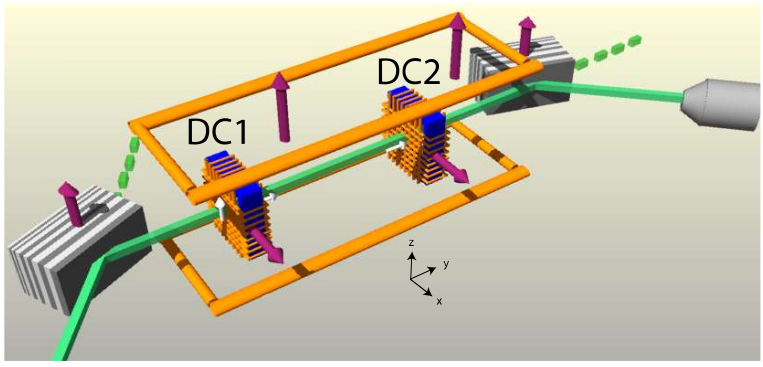

Figure 5.8: Set-up with two auxiliary DC coils (DC1 and DC2) which rotate the spin vectors each by $\pi/2$ with the same sense of rotation. The distance between the coils is chosen such that two full Larmor precessions occur between them.

Results

Both DC coils were positioned to result in a $2\pi n$ Larmor precession with a distance of about 15 cm between them. The current for the x-field of DC2 was then scanned to result in a polarogram (see Fig. 5.9). The combined contrast sank to 79 % from their individual values of 86 %.

Discussion

15 cm are certainly two full Larmor precessions in the 9 G guide field when comparing with the value of 8.87 cm for one full precession (compare Equation 3.20). As the field amplitude was

measured with a Hall probe, the deviation from the calculated value of about 10 % is an estimation of the error of the measurement of the field amplitude.

In Figure 5.9, a zero current in the circuit for a x-field in DC2 results in an intermediate value of the count rate. This represents the situation where the polarisation vector is rotated in DC1 into the horizontal plane. It is then affected by the Larmor precession in the guide field which is interrupted in DC2. The neutrons propagate to the polarising supermirror with equal ratios of up and down-spin states, which results in a medium count rate. The current of approx. 600 mA in the minimum intensity was used to adjust the position as described in the "Procedure" section of 5.2.2.

While one auxiliary coil has 86 % contrast, the decline to 79 % can be solely attributed to the efficiency of spin manipulation of one auxiliary DC coil. The naïve estimation of approx. 6 % loss for one coil yields 92 % degree of polarisation as the basis for assessments of all results. With this reference, in review, the approx. 75 % contrast in the DC case of the Mashhoon box, which is not designed for polarimetry, can be considered as high.

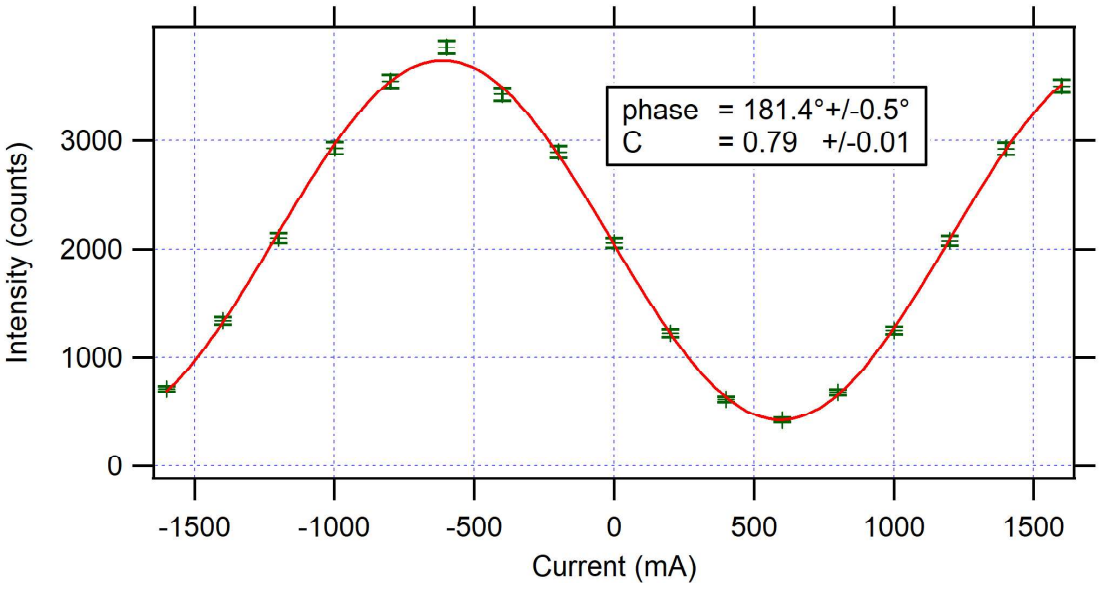

Figure 5.9: Scan of the current for a x-field of DC2. DC1 is adjusted to rotate the polarisation vector by $\pi/2$ and the position of DC2 is adjusted to a distance corresponding to a 4π Larmor precession between the two coils.

5.2.3 Case of Single Interferometer Arm

Procedure

Now, the Mashhoon box is again integrated into the set-up. The goal of this step is to test its interaction with an initial polarisation vector parallel to the beam direction. In this subsection, a static field is used before a rotating field is used in Section 5.3. To produce the spin state parallel to the beam direction at the entry of the Mashhoon box, its position relative to DC1 is set: the distance is adjusted in the same way as between the two auxiliary DC coils in the previous section but with DC1 and Mashhoon box. As the space in the guide field is limited and in the next step DC2 is supposed to be used in the rear of the Mashhoon box, DC1 stays at its place while the Mashhoon box is placed in the middle of the guide field. They are therefore closer together than DC1 and DC2 in the previous step and the integer n of the number of full Larmor precessions

between DC1 and Mashhoon box is smaller. In this configuration, the spin state leaving DC1 is again parallel or antiparallel to the beam direction and the same as the input for the Mashhoon box. The same procedure is applied to the pair of coils of Mashhoon box and DC2. In this step, the Mashhoon box is fixed in its position and DC2 is placed, in the according current configuration, such that a minimum count rate arises. Again, the compensation of the Mashhoon box and DC2 is therefore re-adjusted.

Then DC1 is turned on again and produces a field that rotates the polarisation vector into the horizontal plane. To assess the quality of spin manipulations with the Mashhoon box, it is set to perform π-flips as well as 2π-rotations with three different static field configuations of its own two coils fixed while DC2 is scanned in its x-field (see Fig. 5.10). The three configurations are: a strengthened guide field (+z), an overcompensated guide field with an effective field antiparallel to the guide field (-z), and a compensated guide field with an additional x-field (x). An additional configuration with a x-field with antiparallel direction was not implemented due to the symmetry of the coil.

The above-described sequence of the coils (DC1, Mashhoon box, DC2) is the same for the portion of the neutronic wave through one interferometer arm in the planned interferometer experiment (see Fig. 2.10). Instead of the phase shifter, DC2 is scanned to produce polarograms.

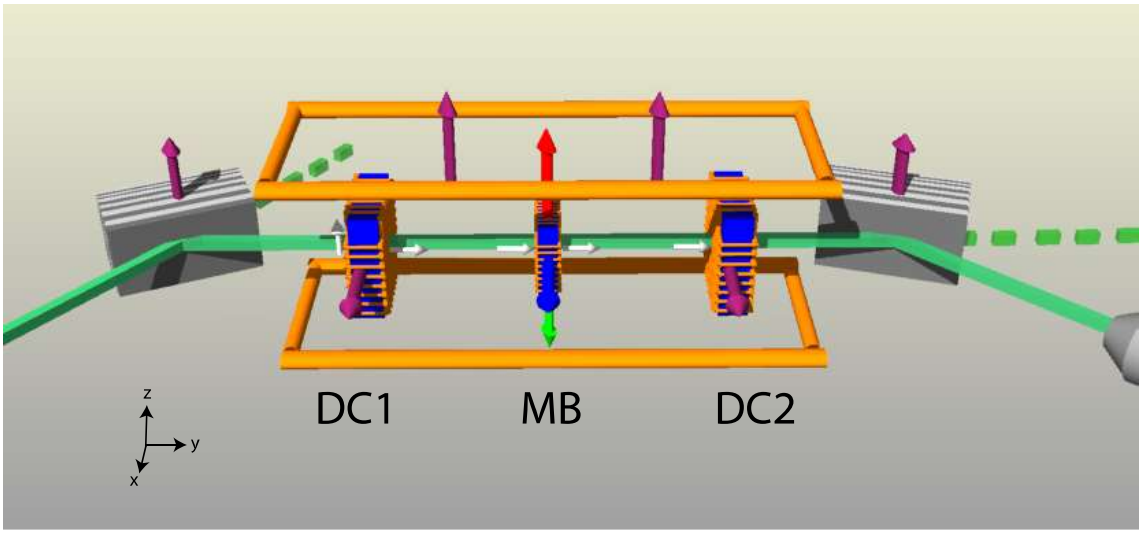

Figure 5.10: DC1, Mashhoon box and DC2 are placed in the guide field at positions which produce one full Larmor precession between each pair of coils. DC1 is set to rotate the polarisation vector by $\pi/2$ into the horizontal plane. The three differently coloured arrows at the Mashhoon box correspond to different effective field directions inside it. The colour code for the directions is the same as in Figure 5.11.

Results

In the adjustment of the distances of the coils, the minimum count rates resulting from full Larmor precessions are at distances of 9 cm between DC1 and the Mashhoon box and 10.5 cm between Mashhoon box and DC2. To produce the minimum count rate with the latter pair, DC2 was replaced approx. 4 cm compared to the adjusted situation of a 4π Larmor precession in Section 5.2.2 which is about the diameter of the Mashhoon box of 5 cm.

Using all three coils at once according to their purpose in this step, the polarograms and their sinusoidal fits of the supposed π-flips are presented in Figure 5.11a. For supposed 2π-rotations

Table 5.1: Contrasts and phases obtained by fitting the polarograms in Figure 5.11.

rotation angle	contrast with field direction (%)			phase with field direction (°)			mean phase (°)
	+z	-z	x	+z	-z	x	
π	80.6	78.0	76.1	-9.71	-9.30	4.53	-5±8
2π	74.3	68.5	75.2	-174.99	-180.85	-180.00	-179±3

the polarograms and their fits are presented in Figure 5.11b. The important results of the fits are listed in Table 5.1. The mean phase of the sinusouidal fits compared to a sine is approx. $-179°$ for 2π-rotations. The mean phase of the fits for π-flips by the Mashhoon box is approx. $-5°$. With the Mashhoon box incorporated in the set-up, the contrast remained stable at the approx. 80 % of the previous subsection for the π-flip with strengthened guide field only. All 2π-rotations and the π-flips with effective fields in x and -z-direction had further reduced combined efficiencies of the spin manipulation. Each π-flip was better than any 2π-flip in terms of contrast. But for the 2π case with overcompensated guide field and contrast below 70 %, all efficiencies are on level or even higher than the Mashhoon box alone (∼75 %). Which field direction results in the highest/lowest contrast, changes with the rotation angle. Only tendencies can be stated: a strengthened guide field to produce the rotations results in the highest contrast for the π-rotation while an effective x-field is slightly better for the 2π-rotation. The effective field in -z-direction has lowest contrast for the 2π-rotation and an intermediate contrast for the π-rotation.

Discussion

The distance of 9 cm between DC1 and Mashhoon box is near the calculated value for one full Larmor precession at the guide field of 9 G. The distance of 10.5 cm between Mashhoon box and DC2 for this case is only roughly the calculated value. The first auxiliary DC coil is closer to a supermirror than the first one. It seems, the guide field strength is significantly changed towards the supermirrors. This deviation may be the reason for the deviations between the calculated distances and the measured ones. The necessary displacement for the adjustment of the distance of DC2 of approx. 4 cm can be assumed to be the effective length of the Mashhoon box in terms of its field regime although its physical diameter is approx. 5 cm. The discrepancy of 1 cm can be attributed to the field transitions.

In general, the fitted phase shift from supposed π-flips to 2π-rotations are accordingly: The expected difference between the according fits is an additional phase shift of $\pm 180°$. The phase shift resulting from the measurements are $-174°$. The deviation from the expected value are $6°$ which are acceptable 4 % of the expected absolute value of $180°$.

The losses in contrast of the polarograms can be seen when the rotation angle inside the Mashhoon box is increased: the π-flips are better than the 2π-rotations. Furthermore, when the effective field in the Mashhoon box deviates more from the outer guide field, the effectivity of the spin manipulation is decreased: rotations with strengthened guide field have smaller field changes and have high effeciency because lower field differences constitute a more homogeneous field. In contrast, when reversing the guide field with overcompensation, the field difference between initial guide field and desired counter field is bigger. Therefore, the inhomogeneities of the effectively generated field becomes larger as well and reduce the efficiency of the spin manipulation. The comparison between overcompensated guide field and effective x-field yields contradicting results: the contrast of the flip with only field in z-direction is better than compensation and additional x-field for the π-flip but vice versa for the 2π-rotation. This can be seen with the fits: for overcompensated guide field and 2π-rotation, the counts deviate more to intermediate values of intensity at higher

absolute currents from the fit and reduce the value of contrast. Fitting only the miniumum and maximum intensities at lower currents would result in a contrast in the range of all other cases of field directions and rotation angles. However, the lowered contrast is still valid to qualify the properties of the field, including higher currents. Because all those measurements were only done once, their reliability is disputable. The significance of deviations between contrasts is higher for higher deviations.

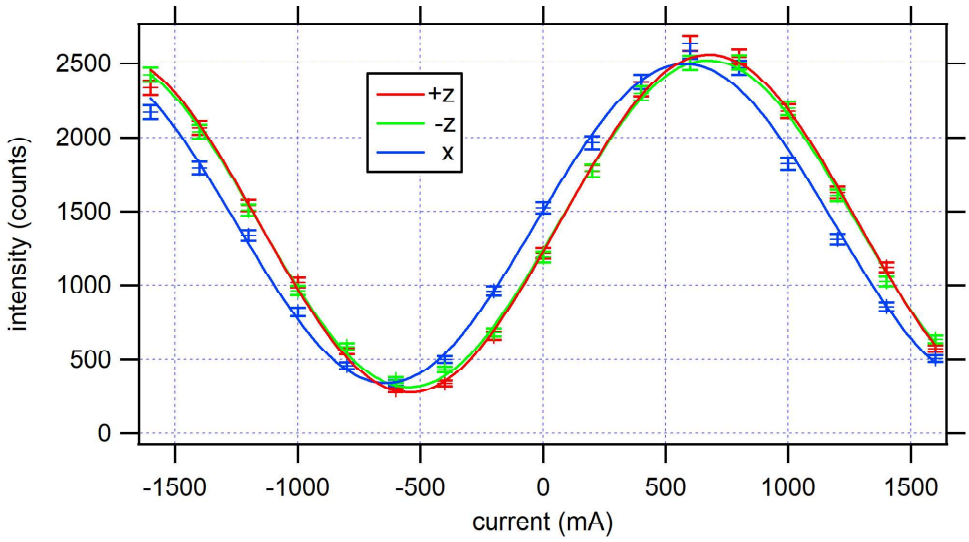

(a) Spin flip with Mashhoon box scanned with DC2. The inlet specifies which polarogram corresponds to which effective field direction inside the Mashhoon box.

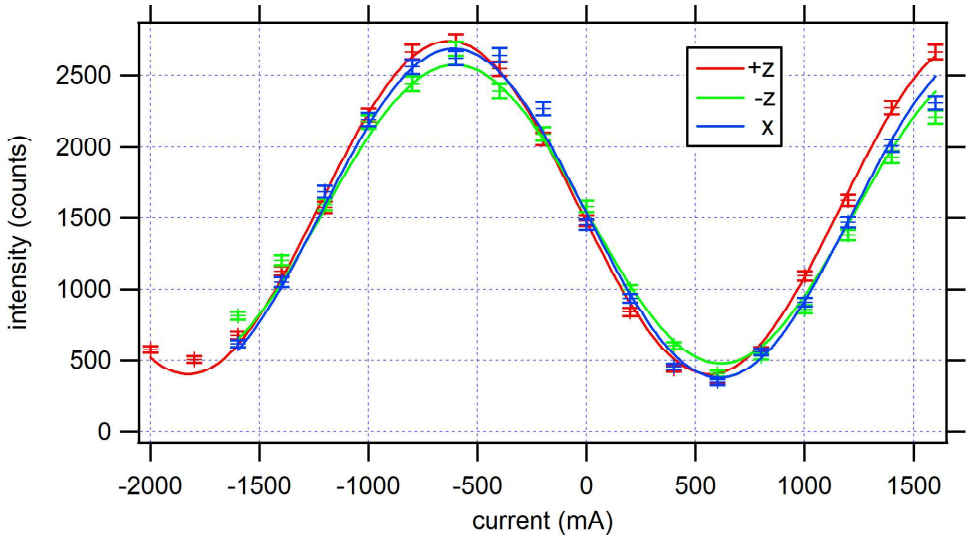

(b) Spin rotation by 2π with Mashhoon box scanned with DC2. The inlet specifies which polarogram corresponds to which effective field direction inside the Mashhoon box.

Figure 5.11: Scans of DC2 with rotations of the polarisation by the Mashhoon box in the static case. See also Figure 5.10 for description of the colour code.

5.3 Adjustment of the Rotating Field

Procedure

After adjusting the positions of the coils with static fields, the Mashhoon box's field is changed to a rotating one superposed by the static field for the guide field compensation (see Fig. 5.12). The rotating field is necessary to induce the spin-rotation coupling, like in the intended interferometer experiment (see Section 2.8). To generate the rotating field inducing the spin-rotation coupling, both coils of the Mashhoon box are supplied with ACs phase shifted by 90°. The sign of this phase shift determines the sense of rotation of the field, the sign of the rotation vector $\vec{\Omega}$, and the sign of the spin-rotation coupling phase for a specific eigenstate (see also Equ. (2.39)).

The coils DC1 and DC2 are both set to rotate the polarisation vector by $\pi/2$. The spin orientation leaving DC1 is then parallel or antiparallel to the beam direction. With the adjustments explained in the previous Sections 5.2.2 and 5.2.3, this is also the spin orientation entering the Mashhoon box. With only the guide field compensation in the Mashhoon box turned on, the final rotation by DC2 produces a minimum count rate. The goal in this section is to adjust the amplitude of the added rotating field for each frequency to generate cyclic spin evolutions with $\alpha = 2\pi$ (compare Equ. (2.42)). This adjustment would automatically create a cyclic spin evolution for the orthogonal spin state. This property is used in the final measurements of Section 5.4 for the reproduction of the results of Demirel et al. The present procedure will be reproduced in one interferometer arm in the intended interferometer experiment (see Section 2.8). Therefore, this step is crucial to test whether the Mashhoon box used is suitable for the interferometer experiment.

In the case of AC, two electric resonant circuits are formed with a variable capacitator (see Section 4.4) integrated in both of them. Each circuit is supplied by an amplifier which in turn is supplied with a signal from a dual channel "Tektronix AFG 3022B" function generator. The currents in the circuits were observed with a "Tektronix TBS 1052B-EDU" digital oscilloscope, supplied with the signal of a current probe. First, amplifiers of the model "AG Series Amplifier" by the firm "T&C Power Conversion, Inc." were used. But this type is designed for frequencies of MHz and does not provide a stable sinusoidal signal in the necessary range of kHz. Thus, a model "TOE 7610-20" of the firm "Toellner" was used which proved suitable for the application.

The resonance of the RLC circuit is determined by finding the capacities with which the highest current amplitudes at the respective frequency for a fixed signal from the generator are accomplished. With these capacities, the field amplitude is scanned and the respective count rates are recorded. In contrast to a static field, for a rotating field an increased field amplitude and a longer amount of interaction time are not equivalent. This means, the evolution paths with adjusted amplitudes presented in Figure 2.4 are only hints of the tendencies of evolution paths with other amplitudes. For a zero amplitude, no change in intensity is expected. While scanning the amplitude, from the original minimum a raise, a decline and another raise in count rate are anticipated. The first maximum is attributed to a spin manipulation inside the Mashhoon box with the leaving polarisation vector closest to a π-flip while the minimum represents a cyclic evolution back to the initial orientation. As the referenced evolution paths of Figure 2.4 show, the spin state is changed less for higher frequencies. In the case $\alpha = 2\pi$, a flip in a scan of amplitude for a fixed frequency is only possible with a static field, i.e. $\Omega = 0$. The flip would lead to a maximum in count rate. Therefore, it is expected in the amplitude scans that a decline in intensity of the maxima arises with rising frequency.

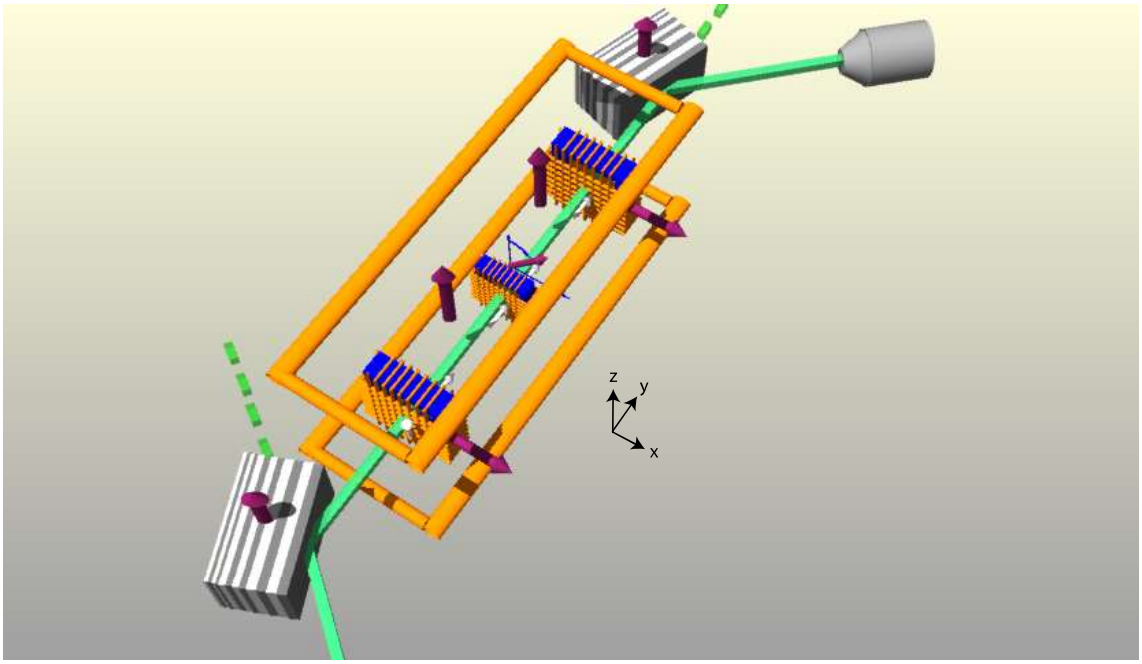

Figure 5.12: Same set-up as in Figure 5.10, but the Mashhoon box is supplied with currents that generate a rotating field.

Results

The capacities for the resonant case are presented in Table 5.2. They accord with the magnitude and tendency of the calculations (see Table 4.1) but are generally lower. The signals necessary for the same current oscillations differ systematically for both coils: the coil used for compensation, too, consistently needs a signal that is about 20 % higher. Initially, I did not mention the difference of the circuit with DC compensation and assumed both circuits to be similar. Therefore, this step had to be repeated when the subsequent flaws of spreading contrasts for different frequencies became clear. The signal for compensation is almost constant. It was generated with the signal generator as well. The offset feature of the amplifier was not used because it is regulated with a screwdriver and its reproducibility is significantly lower than the signal generator's digital operation.

In a scan with fixed frequency, rising amplitudes result, as expected, in an initially higher, then minimum count rate before another increase (see Figs. 5.13a-5.13e). The amplitudes for maxima and side minima are separated roughly by a factor 2. The minima are of the same height for all but 50 kHz. The amplitudes' values for the maximum and second minimum decline with increasing frequency. The maxima between initial and side minima get lower with increasing frequency and cannot be distinguished from a plateau for 50 kHz. With the amplitudes of the second minimum (see Fig. 5.13f and 3$^{\text{rd}}$ column in Table 5.2), polarograms were recorded (see Fig. 5.14). In the case of the plateau, the highest amplitude before the significant rise was chosen. For frequencies 30–50 kHz the respective contrasts are about 75 %, while for 10 kHz it is slightly lower and for 20 kHz slightly higher.

The theoretically expected field amplitudes are compared with those of the experiment in Figure

Table 5.2: The applied configuration of the electrical circuit for all AC frequencies.

frequency (kHz)	capacity (µF)	amplitude for minimum (mVpp)	signal for x-coil (mVpp)	signal for z-coil (mVpp)	signal for compensation (mV)
10	7.45	320	650	754	94
20	5.5	290	731	933	95
30	2.2	250	858	1031	94
40	1.5	200	734	903	93
50	0.9	125	541	669	93

5.15. Above a maximum frequency, here ∼58 kHz, a cyclic evolution with $\alpha = 2\pi$ is not possible any more. Only cyclic evolutions with higher integer n in Equation (2.42) are then possible.

Discussion

For low frequencies the scans are almost sinusoidal. The increases and declines correspond to spin rotations that move further and further from the original polarisation vector towards the opposing one, then the case $\alpha = 2\pi$ of a cyclic evolution of the spin state and a further rotation in the case of the following increase of the intensity. The fact that the two minima cannot be distinguished in intensity is a sign of quality of the cyclic rotations between them. As the according minimum is slightly increased for 50 kHz, the according spin manipulation may be slightly decreased in its quality.

The polarograms are of high contrast. The AC case, counterintuitively, has no further losses. Also the expected losses in contrast with increasing frequency do not occur, contrary to the indication of a slight elevation of the minimum for 50 kHz.

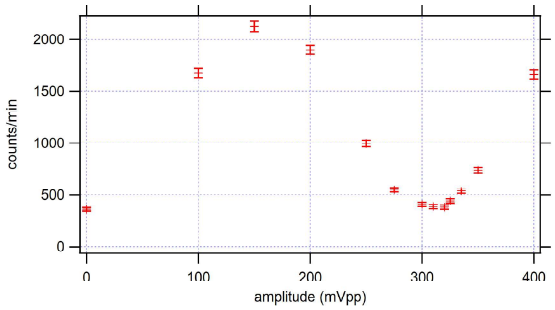

(a) 10 kHz

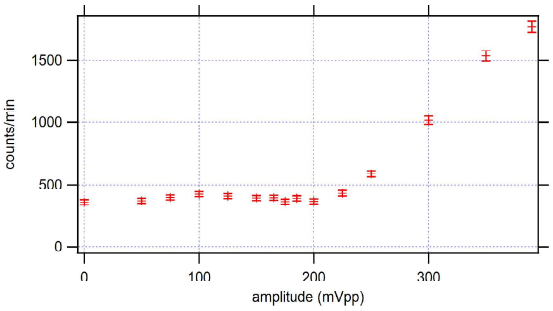

(d) 40 kHz

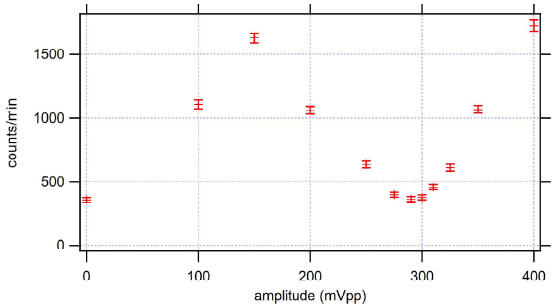

(b) 20 kHz

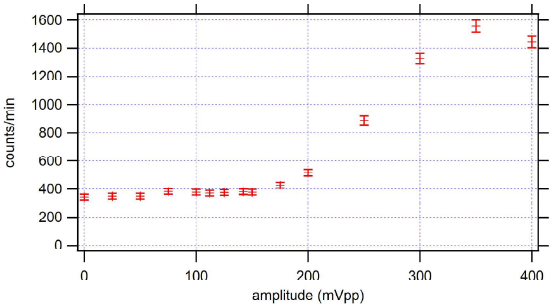

(e) 50 kHz

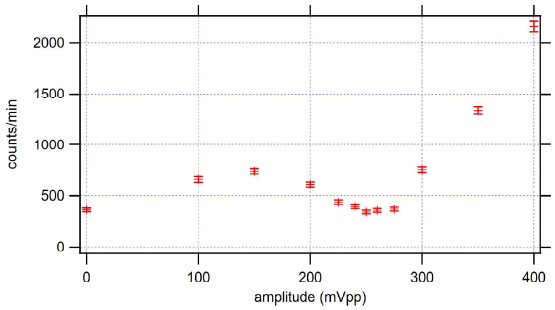

(c) 30 kHz

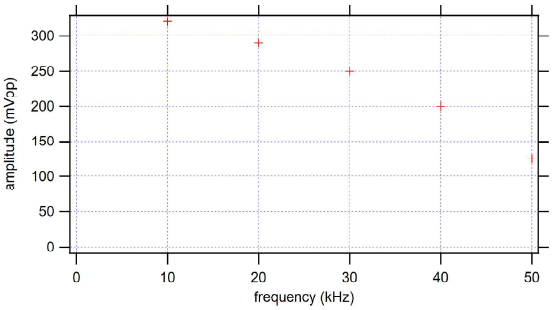

(f) Assumed amplitudes of the rotating field for the cylic spin evolutions for all frequencies. This amplitudes were used as adjustment for the polarograms in Figure 5.14.

Figure 5.13: Scans of the amplitude of the rotating field generated by the Mashhoon box for each frequency used. At zero amplitude, the polarisation is unchanged inside the Mashhoon box which corresponds to a minimum count rate. With rising amplitude, the manipulation of the polarisation is stronger. The first maximum corresponds to the manipulation inside the Mashhoon box closest to a π-flip. At the first minimum, the cyclic case is adjusted. Larger amplitudes increase the intensity again. The last figure shows the amplitudes for the side minima in dependence of the frequency.

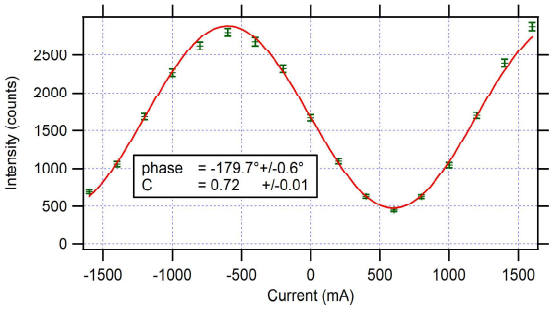

(a) 10 kHz

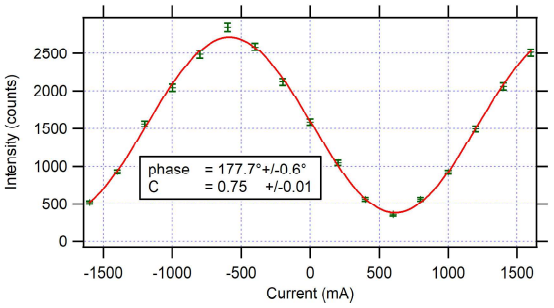

(d) 40 kHz

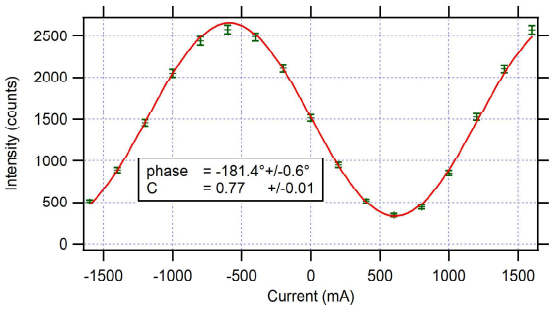

(b) 20 kHz

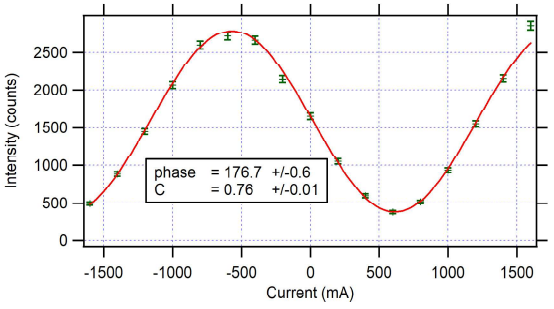

(e) 50 kHz

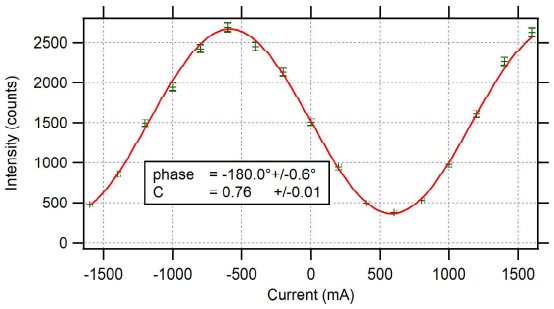

(c) 30 kHz

Figure 5.14: Polarograms with adjusted amplitude of the rotating field for cyclic paths of the spin state inside the Mashhoon box. The x-field of DC2 is scanned while DC1 rotates the spin orientations by $\pi/2$. The inlets contain fit parameters.

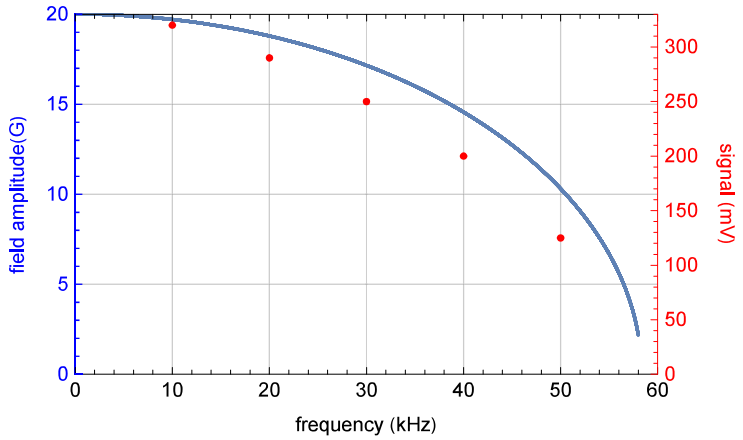

Figure 5.15: Theoretically calculated necessary amplitudes of the rotating magnetic field in blue for a cyclic evolution with $\alpha = 2\pi$ (see Fig. 2.4) and with a fixed interaction time in dependence of the frequency. The interaction time is defined to ∼17 µs by the wavelength λ of the neutrons of 1.7 Å and the path length l in the Mashhoon box of 4 cm via $t = lm\lambda/h$. The signal amplitudes which realise the cyclic case the best are in red on a different scale. Both show alike dependence on the frequency.

5.4 Final Measurements of Phase Shift due to Spin-Rotation Coupling

Procedure

The previous results are used to try to reproduce the results of Demirel et al. Those authors used an up-polarisation as input for the Mashhoon box and DC1 was not used anymore (see Fig. 5.16). In the according base, an up-spin is regarded as a superposition of forward ($|+y\rangle$) and backward-spin ($|-y\rangle$). Each one of them can be manipulated simulateously onto a cyclic path with $\alpha = 2\pi$. In this cyclic case for both forward and backward spin, the final superposition differs to the initial one by the geometrical phases added due to spin-rotation coupling. The resulting total relative phase rotates the initial up-polarisation to the x-z-plane. To verify this, DC2 is scanned. The situation at the entry of DC2 has to be considered: with the adjusted distance between the Mashhoon box and DC2 and a full Larmor precession between them, the input state for DC2 is like the output state of the Mashhoon box. For all polarisation vectors with positive z-component, the polarograms scanned with an effective x-field inside DC2 will have a maximum at zero current. At certain threshold frequencies, the z-component of the polarisation vector will change its sign due to an increased relative phase induced by spin-rotation coupling. This means at these threshold frequencies π phase shifts of the polarograms arise. Only the contrast will differ with frequency of the currents, because certain polarisation vectors will rotate on great circles while in the other extreme case the polarisation vector for the threshold frequencies are (anti)parallel to the x-field and will not be changed at all resulting in zero contrast. Only a y-field could be used to generate suitable polarograms. But only a x-field is available. As a consequence, the initial angle in the x-z-plane is changed into an angle in the y-z-plane using the guide field. A displacment of DC2 according to a quarter Larmor precession accomplishes this. Inside the effective x-field of DC2, this leads to great circle rotations of the polarisation vector for all phase shifts. The polarograms should then have same contrasts and only differ in the phase of their fit functions that is equivalent

to the relative phase induced between up and a down-spins interacting with the rotating field of the Mashhoon box.

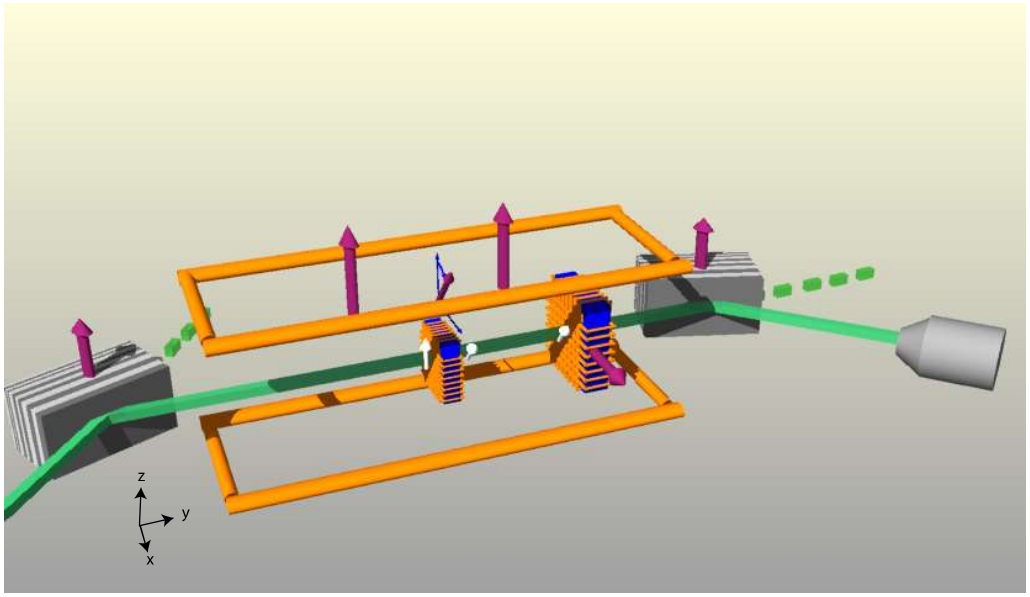

(a) Larmor precession of the spin orientation between Mashhoon box and DC2 by 2π.

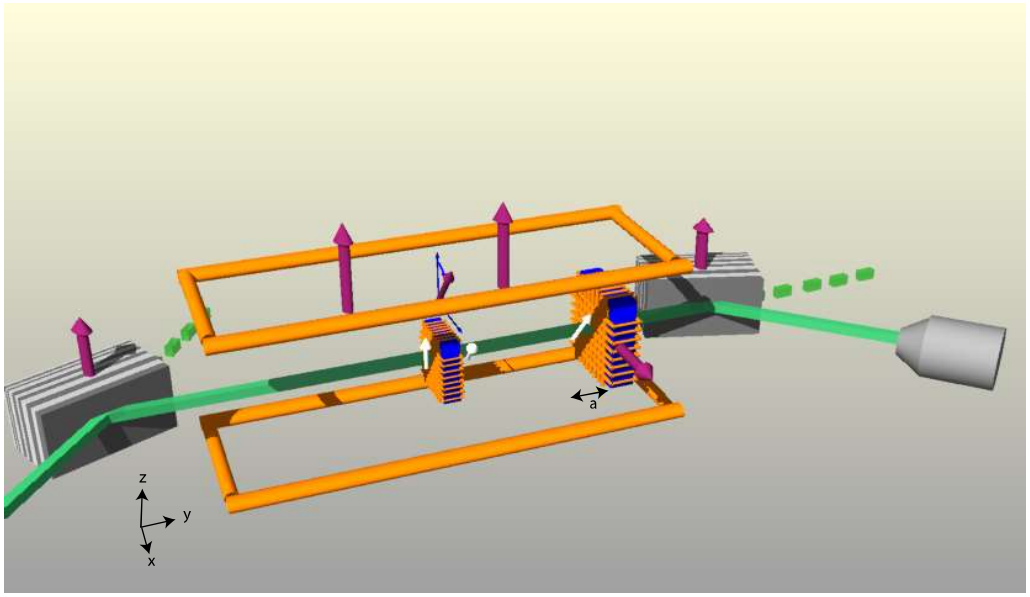

(b) With DC2 replaced by a, Larmor precession of the spin orientation between Mashhoon box and DC2 by $\frac{5}{2}\pi$.

Figure 5.16: Additional displacement of DC2 while DC1 is not used in this last step.

Results

To produce similar contrasts for all frequencies, DC2 was relocated by 2.2 cm which are approx. a quarter of the calculated value for one Larmor precession. With the DC1 turned off and superpositions of forward and backward spin as input for the Mashhoon box, initially, only a single polarogram for each frequency was recorded (see Fig. 5.17). The sinusoidal fits have an increasing phase shift with higher frequency. Because the spin-rotation coupling is expected to be linear in frequency (see Equ. (2.44)) a linear fit of the phase was made. The fit function is

$$\phi(f) = a + bf \tag{5.1}$$

with phase shift ϕ and frequency f. This fit was not satisfying, because it exceeds the calculated standard deviations of the phases. To gain a statistical advantage, ten polarograms for each frequency were recorded. The statistical evaluation of them produces a mean phase for each frequency. In general, the respective standard deviation did not change much compared to a single polarogram. A linear fit for all frequencies still does not match all points in the limit of their estimated errors (see Fig. 5.18a). But when neglecting the point for 50 kHz, the linear model fits the data from 0–40 kHz (see Fig. 5.18b). The according fit parameters are

$$\begin{aligned} a &= (-0.3 \pm 0.6)^\circ, \\ b &= (6.94 \pm 0.02)^\circ\,\mathrm{kHz}^{-1}. \end{aligned} \tag{5.2}$$

Compared to the extrapolation, the phase shift for 50 kHz is about 15° too low. When varying the amplitude of the rotating field on the plateau, a wide range of phase shifts can be created, including the one matching the fit (see Fig. 5.19).

Discussion

The calculated value for the Larmor precession was very accurate in predicting the right replacement of DC2. This fact is surprising because in Section 5.2.3 the deviation from the calculated value of the position of DC2 relative to the Mashhoon box was explained as a result of the increasing influence of the supermirror to the magnetic field at the end of the guide field. In the present case, in the same region, the positioning follows exactly the calculation.

The statistical evaluation of the polarograms seems to generate solid, mutually confirmative values for 0–40 kHz. The value in the case of the high frequencies of 50 kHz differs from the linear phase shift. Usually, higher frequencies are expected to produce higher errors: the generated fields could deviate more and more from the intended field, although such an effect could not be observed with the oscilloscope. In the present case, because the spin orientation is not changed much in the according regime of low field amplitudes, the cyclic case of the spin evolution of the polarisation vector is harder to determine with increasing frequency. The plateau of the amplitude scan in Figure 5.13e does not allow to find and choose the amplitude for the second minimum accurately. What speaks against this argument, however, is the following fact: At the same time, the phase shift for 50 kHz is not following the calculation of the spin-rotation coupling, but the contrast in this case is almost 80 %.

While the fit parameter a is near zero due to setting the phase for the static field as zero, the parameter b can be compared to the value predicted for a spin eigenstate. This value can be calculated from the argument of the third exponential in Equation (2.39) of

$$\frac{\Omega t}{2}. \tag{5.3}$$

The measured phase shift is the total relative phase between both eigenstates of the rotation vector. The slope of the fit must be divided by 2 to get the phase shift for a single eigenstate.

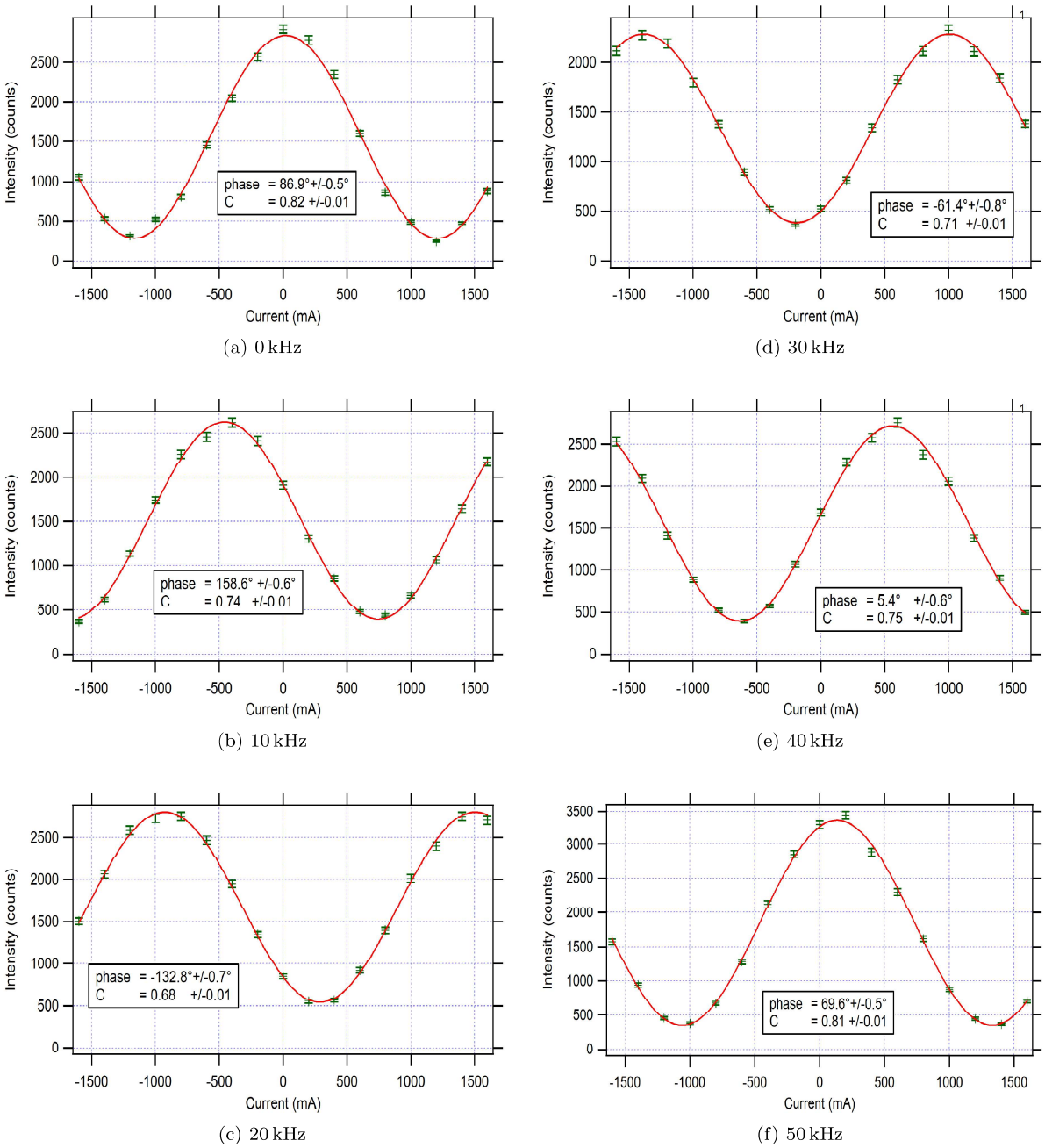

Figure 5.17: First polarograms for each frequency. The phase shift increases with higher frequency. The phase obtained by the fit is ambiguous to additional phases of $2\pi n$ with an integer n.

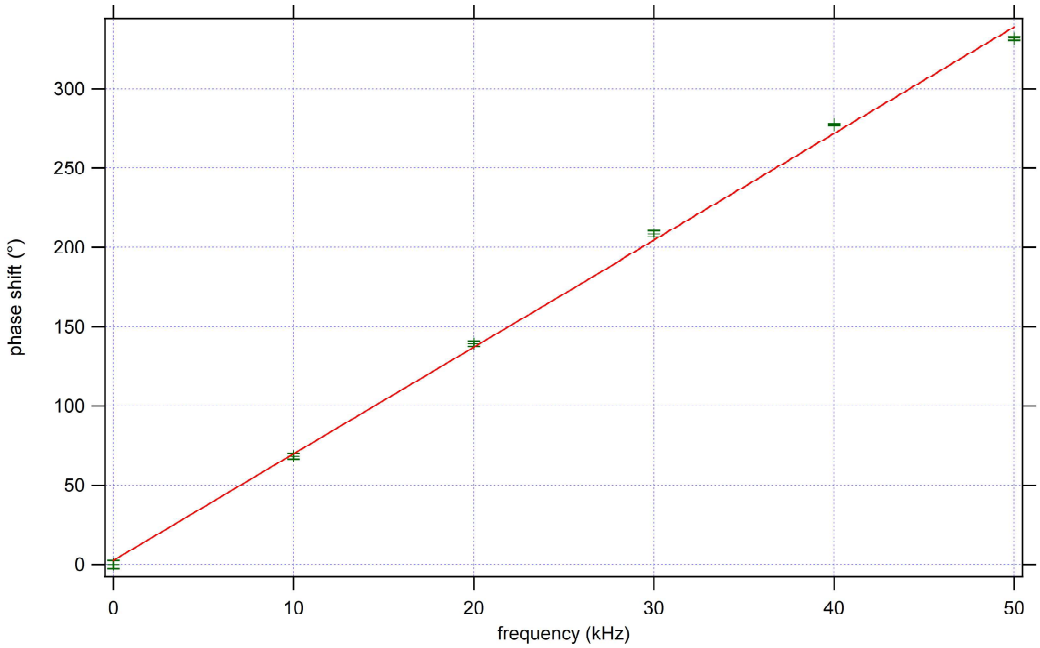

(a) A linear fit up to 50 kHz does exceed the standard deviations.

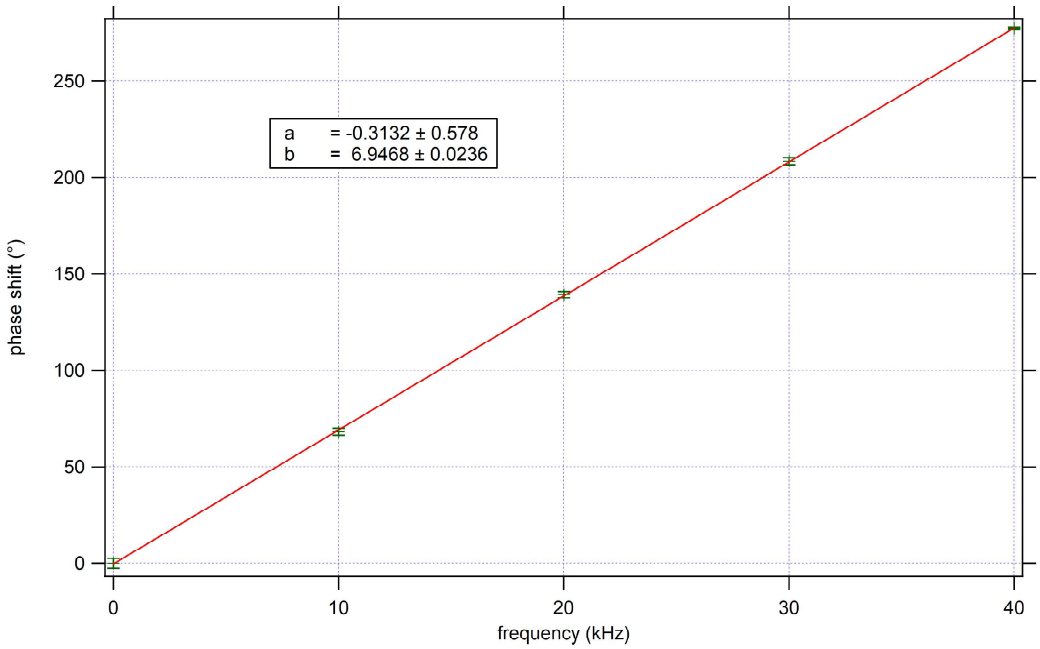

(b) A line up to 40 kHz of the model of Equation (5.1) fits within the errors. The inlet contains the fit parameters.

Figure 5.18: The Gaussian fits of 10 polarograms each are merged to a single point with standard deviation. The graphs exhibit rising phase shift with the frequency. The phase for 0 kHz was substracted for all points as renormalisation.

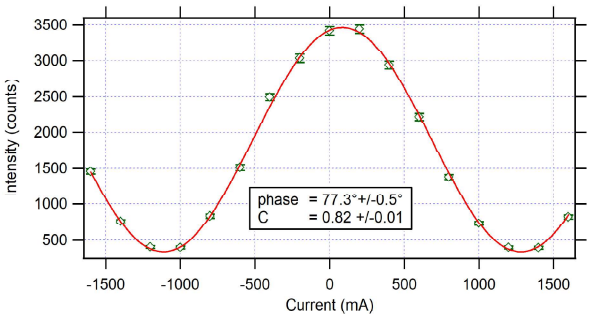

Figure 5.19: Polarogram obtained by adjusting the signal of the amplitude of the field rotating with 50 kHz to 75 mV. The fitted phase shift is less than 1.5 standard deviations apart from the extrapolated value of the fit in the range 0–40 kHz.

Furthermore, the time of interaction has to be estimated. With the estimation of the effective length of the Mashhoon box of 4 cm (obtained in Section 5.2.3) and the wavelength of 1.7 Å, the expected slope of the phase shift is calculated as

$$3.08\,^\circ\,\mathrm{kHz}^{-1}. \tag{5.4}$$

This value is of the same magnitude but more than 10 % off the measured value. The deviation may be due to a overestimated effective length of the coil.

5.5 General Experimental Aspects

5.5.1 Imperfections

The starting point for an error estimation are in the present case the properties of the mosaic monochromator: it selects neutrons with a broad peak around a wavelength that are reflected towards the beamline. As each wavelength corresponds to a velocity and the velocity determines the time period of a neutron in a coil, the spin manipulations for each wavelength are different. To reduce this error with the use of a single crystal monochromator would reduce the count rate significantly at the TRIGA Mark II reactor. All efforts to reduce other errors have to consider this initial error: a reduction of other errors makes only sense, as long as they are in the same order of magnitude as the fixed error from the effects of the mosaic monochromator.

Another main error comes from the divergence of the beam that increases the cross-section with increasing distance form the source. Generally, the magnetic fields depend on the position. Different neutrons consequently interact with more different magnetic field strengths and directions when they diverge. Also the imperfect degree of polarisation of the supermirrors contributes largely to the errors. This last influence can at least be estimated to 92 % through the comparison of the different contrasts of polarograms (see paragraph “Results” in Section 5.2.2).

An easy improvement would be to change the type of supermirrors used. As these tests are a proof of concept, supermirror and detector available at the beamline with reduced degree of polarisation have been used. The best supermirrors of the neutron physics group at the Atominstitut have a degree of polarisation $> 97\,\%$. For the preparations of the interferometer experiment, the reduced degree of polarisation is still sufficient to characterise the new coil design. For the final experiments of the presented project, a better type of supermirrors will be used.

5.5.2 Count Rate Variations

During the measurements, a variation of the count rate of up to a third loss occured with otherwise the same set-up in coil positions and applied currents. This was only mentioned by comparison between polarograms. As an example, a series of subsequent polarograms is presented in Figure 5.20. A continuous effect during single measurements of polarograms of about 20 minutes or a reduced contrast was not apparent. This means that, fortunetly, all results are valid. Only the relative error is greater than possible with a higher count rate.

A general tendency was a decline during the day from the reactor start-up at 8:45 a.m. to shut-down at 3:45 p.m. On the next day, the intensity once more regained its initial level. This suggests a latent cause in the set-up which intensifies during the operation.

The reactor itself was suspected at first. However, its power is, as mentioned previously and assured by the Reactor Manager Mr. Villa, linearly dependent to the neutron flux inside which in turn is linearly dependent on the count rate. Mr. Villa also stated that the upper boundary for fluctuations in power is 1 %, much too low for an explanation.

Both DC coils and the Mashhoon box were placed in the beam throughout this period. Therefore, a lowered count rate cannot be attributed to more material interacting with the neutrons. A minor reservation regarding this argument will be formulated in the next paragraph. However, other possible reasons were considered. As explained previously, the guide field increases the count rate by about 10 % by avoiding depolarisation. When implementing the Mashhoon box, a decrease was observed. The divergence of the beam might play a role, but the window of the coil mounter has 2 mm clearances in all directions implemented. When the parts were put together with acetone solving, I made a mistake and had to repair the window at both ends: so the window itself was not of best quality. However, the openings were measured in their cross-section and have the same dimensions as intended. Also, no water got into the window. However, a position was found where small tilts and translations of the coil did not reduce the count rate. Only bigger changes did so, by amounts that suggest scattering or absorption of neutrons by the coil mounter. Therefore, with the configuration adjusted with the hand monitor described in the Section “Procedure” in Section 5.2.1, the Mashhoon box is not in the distinct beam.

However, it became apparent not only neutrons flying through the window of the aperture in front of the Mashhoon box are counted: when filling the cooler with water, another decline in count rate was observed. This means that even neutrons that are transmitted through the high absorption material of the aperture, cadmium, get counted. Many of them are scattered by the hydrogen in the added water. In the course of a day, the water evaporates partially and should not reduce but increase the count rate. This was not observed due to the stronger effect in decline of the average neutron intensity. None of the mechanisms above can explain the count rate loss.

The next obvious cause would thus be a heat-related effect from the coils hours in operation. Thus, a goal after the tests was to deliberately induce a continuous decrease in count rate to identify its origin. First, a whole day without any currents induced resulted in a stable count rate. Thus, the reason for higher count rate loss has to be in the electrics of the coils. On another day, the guide field was turned on and the DC coils were attached with a current that strengthens the guide field and should therefore only heat the coils without spin manipulation—with no effect. On a third day, the Mashhoon box was operated the same way of strengthening the guide field—again with no effect.

To date, a precise pinpointing of the cause has not yet been possible. Possible short circuits that change the fields should also lower the contrast which, in contrast, remained stable during the measurements. Perhaps it really was the coil mounter whose material diluted somewhere in the window during the operation of the x-coil and somehow regains its shape when it is cooling

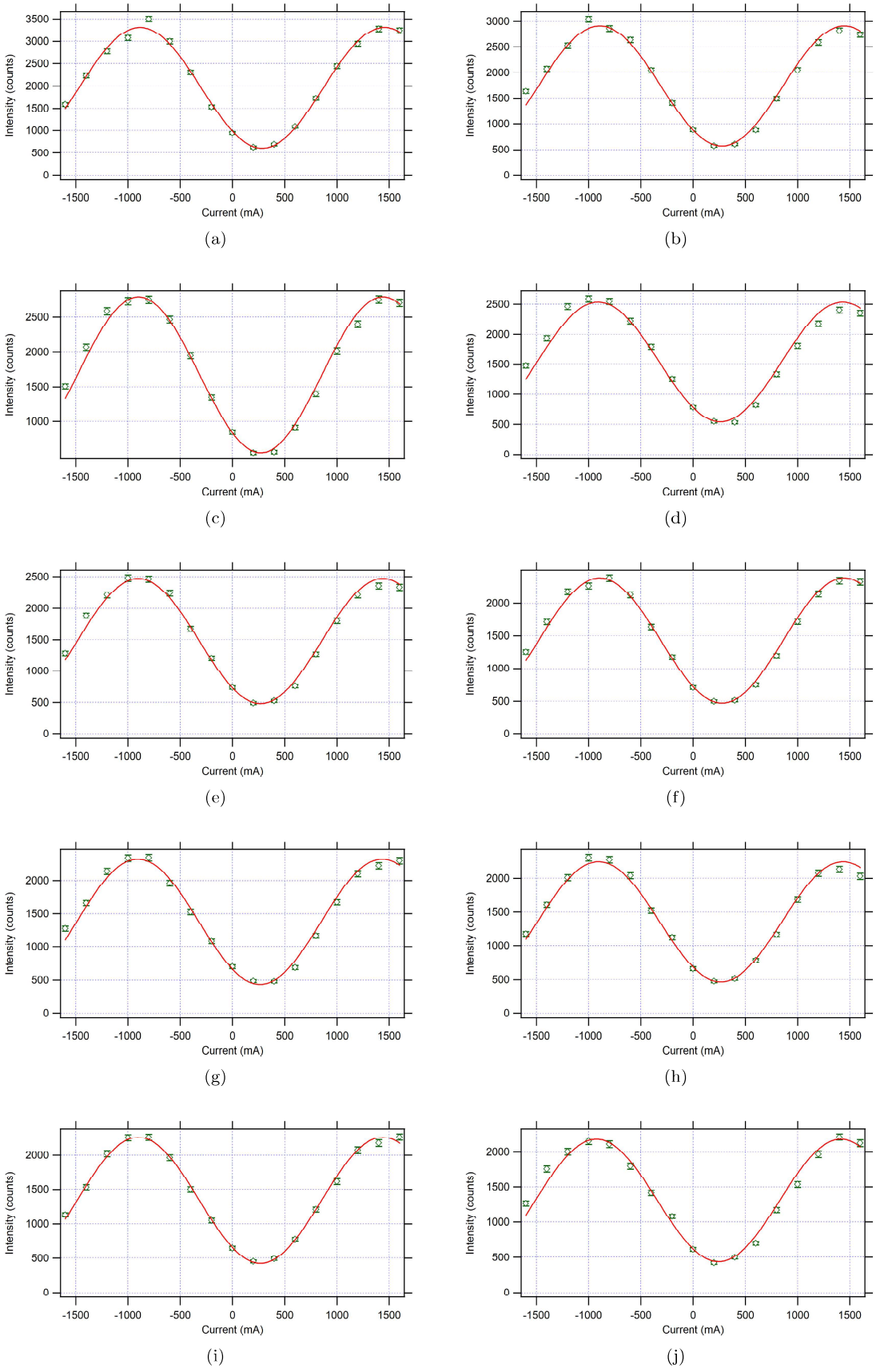

Figure 5.20: A series of subsequent polarograms with the adjustments to measure the phase shift due to spin-rotation coupling at a frequency of 20 kHz. The later the measurement, the lower the maximum intensity.

down. In foresight of the measurements in Grenoble, extra care should be devoted to preparating the coils in order to ensure good statistics: the winding process should exclude any short-circuits and the glueing process any deformations of the coil mount.

Chapter 6

Summary

The design of the Mashhoon box was revised with the goal of creating a window free of any materials for neutrons to fly through in the interferometer. The first experimental tests took place at the polarimeter station at the TRIGA Mark II reactor in Vienna. All coil mounters of the Mashhoon box were printed with a 3D printer. The first attempt with a Helmholtz design did not show the desired properties. The miniaturisation of the design of Demirel et al. with a closed window initially yielded good results. To open the window, grooves were printed on the coil mounter. These fix the wire that is wound around the window.

The magnetic fields for all coil designs were simulated. The grooved one has a field transition of one order of magnitude less than the guide field. According to the field simulations, the sudden field transition aimed should therefore not occur. However, the measurements demonstrate otherwise, probably because in the beam cross-sections the field is very homogeneous in front and after the transitions: the results of Demirel et al. were reproduced with a miniturised Mashhoon box for the frequencies from 0–40 kHz. 50 kHz show less phase shift than calculated.

The suggested guide field strength for the final interferometer experiment is 9 G that allows contrast of about 75 %. The diameters of the aperture are recommended to produce a symmetrical beam in the Mashhoon box. However, in consideration of the Helmholtz coil in the other interferometer arm and the interferometer itself, a weighing of all those factors has to be found. The new coil design should allow the interferograms to have significantly higher contrasts. From the contrast of the interferograms without coils at the previous attempt of about 60 % the estimated goal with an additional factor of 75 % should yield 45 %.

A water cooler fitting the new coil was designed which is much simpler than the previous model. The technique of sticking its parts together was also changed to a more reliable acetone solving. Therefore, it should provide a significantly reduced error probability and make interferometrical measurements stable.

Appendix A

Formulae

A.1 Spin-Rotation Coupling

First, Equation (2.41) will be derived. With that result, Equation (2.35) can be shown more easily: the exponential function is expanded according to its power series as

$$\begin{aligned} e^{i\vec{\alpha}\cdot\vec{\sigma}} :=& \sum_{n=0}^{\infty} \frac{1}{n!} \left.\frac{d^n e^{i\vec{\alpha}\cdot\vec{\sigma}}}{d\vec{\sigma}^n}\right|_{\vec{\sigma}=0} \vec{\sigma}^n \\ =& \mathbb{1} + i\vec{\alpha}\cdot\vec{\sigma} - \frac{1}{2}\vec{\alpha}^2\vec{\sigma}^2 - \frac{i}{6}\vec{\alpha}^3\cdot\vec{\sigma}^3 + \frac{1}{24}\vec{\alpha}^4\vec{\sigma}^4 + \frac{i}{120}\vec{\alpha}^5\cdot\vec{\sigma}^5 - \frac{1}{720}\vec{\alpha}^6\vec{\sigma}^6 - ... \end{aligned} \tag{A.1}$$

With the basic property of all Pauli matrices

$$\sigma_i^2 = \mathbb{1} \tag{A.2}$$

and rearranging the terms, Equation (A.1) simplifies to

$$e^{i\vec{\alpha}\cdot\vec{\sigma}} = \mathbb{1}\left(1 - \frac{\alpha^2}{2} + \frac{\alpha^4}{24} - ...\right) + i\hat{\alpha}\cdot\vec{\sigma}\left(\alpha - \frac{\alpha^3}{6} + \frac{\alpha^5}{120} - ...\right). \tag{A.3}$$

The parenthesis are themselves expansions of the trigonometric functions. It follows that

$$e^{i\vec{\alpha}\cdot\vec{\sigma}} = \mathbb{1}\cos\alpha + i\hat{\alpha}\cdot\vec{\sigma}\sin\alpha. \tag{A.4}$$

Since the dependence to α is linear, the transformation $\alpha \to -\frac{\alpha}{2}$ leads to equation (2.41).

Now to Equation (2.35):

$$e^{-i\frac{\Omega t}{2}\hat{\sigma}_y}\left(\hat{\sigma}_x\cos\Omega t + \hat{\sigma}_z\sin\Omega t\right)e^{i\frac{\Omega t}{2}\hat{\sigma}_y} = \hat{\sigma}_x. \tag{A.5}$$

According to Equation (A.4), the exponentials are expanded to

$$\begin{aligned} & e^{-i\frac{\Omega t}{2}\hat{\sigma}_y}\left(\hat{\sigma}_x\cos\Omega t + \hat{\sigma}_z\sin\Omega t\right)e^{i\frac{\Omega t}{2}\hat{\sigma}_y} = \\ &= \left(\mathbb{1}\cos\frac{\Omega t}{2} - i\hat{\sigma}_y\sin\frac{\Omega t}{2}\right)\left(\hat{\sigma}_x\cos\Omega t + \hat{\sigma}_z\sin\Omega t\right)\left(\mathbb{1}\cos\frac{\Omega t}{2} + i\hat{\sigma}_y\sin\frac{\Omega t}{2}\right) \\ &= \begin{pmatrix} \cos\frac{\Omega t}{2} & -\sin\frac{\Omega t}{2} \\ \sin\frac{\Omega t}{2} & \cos\frac{\Omega t}{2} \end{pmatrix}\begin{pmatrix} \sin\Omega t & \cos\Omega t \\ \cos\Omega t & -\sin\Omega t \end{pmatrix}\begin{pmatrix} \cos\frac{\Omega t}{2} & \sin\frac{\Omega t}{2} \\ -\sin\frac{\Omega t}{2} & \cos\frac{\Omega t}{2} \end{pmatrix}. \end{aligned} \tag{A.6}$$

The result of the two matrix multiplications has the structure

$$\begin{pmatrix} a_{11} & a_{12} \\ a_{21} & a_{22} \end{pmatrix} \tag{A.7}$$

with the components

$$a_{11} = -a_{22} = \cos\frac{\Omega t}{2}\left(\sin\Omega t\cos\frac{\Omega t}{2} - \cos\Omega t\sin\frac{\Omega t}{2}\right) - \sin\frac{\Omega t}{2}\left(\sin\Omega t\sin\frac{\Omega t}{2} + \cos\Omega t\cos\frac{\Omega t}{2}\right), \tag{A.8}$$

$$a_{12} = a_{21} = \cos\frac{\Omega t}{2}\left(\sin\Omega t\sin\frac{\Omega t}{2} + \cos\Omega t\cos\frac{\Omega t}{2}\right) - \sin\frac{\Omega t}{2}\left(\cos\Omega t\sin\frac{\Omega t}{2} - \sin\Omega t\cos\frac{\Omega t}{2}\right). \tag{A.9}$$

This is simplified with the addition theorems

$$\cos\beta = \cos^2\frac{\beta}{2} - \sin^2\frac{\beta}{2} \tag{A.10}$$

and

$$\sin\beta = 2\cos\frac{\beta}{2}\sin\frac{\beta}{2} \tag{A.11}$$

to

$$\begin{pmatrix} 0 & 1 \\ 1 & 0 \end{pmatrix} = \hat{\sigma}_x \tag{A.12}$$

which prooves Equation (2.35).

A.2 Neutron Interferometry

The result of Equation (3.21) is shown using the relative phase $\Delta\chi = \chi_{II} - \chi_I$ and the relation $\cos^2\frac{\alpha}{2} = \frac{1+\cos\alpha}{2}$.

$$\begin{aligned}
I_O &= |\psi_I + \psi_{II}|^2 \\
&= |rrt\ \psi_0 e^{i\chi_I} + trr\ \psi_0 e^{i\chi_{II}}|^2 \\
&= |r|^4|t|^2|\psi_0|^2|e^{i\chi_I} + e^{i\chi_{II}}|^2 \\
&= |r|^4|t|^2|\psi_0|^2|e^{i\frac{\chi_I}{2}}e^{i\frac{\chi_{II}}{2}}(e^{i\frac{\chi_I-\chi_{II}}{2}} + e^{i\frac{\chi_{II}-\chi_I}{2}})|^2 \\
&= |r|^4|t|^2|\psi_0|^2|e^{-i\frac{\Delta\chi}{2}} + e^{i\frac{\Delta\chi}{2}}|^2 \\
&= |r|^4|t|^2|\psi_0|^2|2\cos\frac{\Delta\chi}{2}|^2 \\
&= |r|^4|t|^2|\psi_0|^2 4\cos^2\frac{\Delta\chi}{2} \\
&= 2|r|^4|t|^2|\psi_0|^2(1+\cos\Delta\chi) \\
&= A(1+\cos\Delta\chi)
\end{aligned} \tag{A.13}$$

For Equation (3.22) it is used that $\cos\alpha = \cos^2\frac{\alpha}{2} - \sin^2\frac{\alpha}{2}$, $r = \frac{e^{-2iy}-1}{2}$ and $t = \frac{e^{-2iy}+1}{2}$ with $y = \frac{\pi d}{\Delta}$ where d is the blade diameter and Δ the extinction length. First, it is shown that

$$\begin{aligned}
r^*t &= \frac{e^{2iy}-1}{2}\cdot\frac{e^{-2iy}+1}{2} \\
&= \frac{1}{4}(1-1+e^{2iy}-e^{-2iy}) \\
&= -\frac{1}{4}\left((e^{-2iy}-1)\cdot(e^{2iy}+1)\right) \\
&= -rt^*.
\end{aligned} \tag{A.14}$$

This is used in

$$
\begin{aligned}
I_H &= |\psi'_I + \psi'_{II}|^2 \\
&= |rrr\ \psi_0 e^{i\chi_I} + trt\ \psi_0 e^{i\chi_{II}}|^2 \\
&= |r|^2|\psi_0|^2|rr\ e^{i\chi_I} + tt\ e^{i\chi_{II}}|^2 \\
&= |r|^2|\psi_0|^2\left|e^{i\frac{\chi_I}{2}} e^{i\frac{\chi_{II}}{2}} \left(rr\ e^{i\frac{\chi_I - \chi_{II}}{2}} + tt\ e^{i\frac{\chi_{II} - \chi_I}{2}}\right)\right|^2 \\
&= |r|^2|\psi_0|^2\left(rr\ e^{-i\frac{\Delta\chi}{2}} + tt\ e^{i\frac{\Delta\chi}{2}}\right)^* \left(rr\ e^{-i\frac{\Delta\chi}{2}} + tt\ e^{i\frac{\Delta\chi}{2}}\right) \\
&= |r|^2|\psi_0|^2\left(r^*r^*rr + t^*t^*tt + r^*r^*tt\ e^{\Delta\chi} + t^*t^*rr\ e^{-\Delta\chi}\right) \\
&= |r|^2|\psi_0|^2\left(|r|^4 + |t|^4 - r^*rt^*t\ e^{\Delta\chi} - t^*tr^*r\ e^{-\Delta\chi}\right) \\
&= |r|^2|\psi_0|^2\left(|r|^4 + |t|^4 - 2|r|^2|t|^2\cos\Delta\chi\right) \\
&= B - A\cos\Delta\chi.
\end{aligned}
\tag{A.15}
$$

Bibliography

[1] M. V. Berry, "Quantal phase factors accompanying adiabatic changes," *Proc. Royal Soc. Lond. A* **392**, 45 (1984).

[2] B. Mashhoon, "Neutron Interferometry in a Rotating Frame of Reference," *Phys. Rev. Lett.* **61**, 2639 (1988).

[3] B. Mashhoon, R. Neutze, M. Hannam, and G. E. Stedman, "Observable frequency shifts via spin-rotation coupling," *Phys. Lett. A* **249**, 161 (1998).

[4] B. Mashhoon and H. Kaiser, "Inertia of Intrinsic Spin," *Physica B* **385**, 1381 (2006), arXiv:quant-ph/0508182 [quant-ph] .

[5] B. Demirel, S. Sponar, and Y. Hasegawa, "Measurement of the spin–rotation coupling in neutron polarimetry," *New J. Phys.* **17**, 023065 (2015).

[6] R. DiSalle, "Space and time: Inertial frames," *The Stanford Encyclopedia of Philosophy* (2016).

[7] J. Gilson, "Mach's Principle II," *ArXiv* (2004), arXiv:physics/0409010 .

[8] G. Sagnac, "Sur la preuve de la réalité de l'éther lumineux par l'expérience de l'interférographe tournant," *Comptes Rendus Acad. Sci.* **157** (1913).

[9] A. Michelson and E. Morley, "On the Relative Motion of the Earth and the Luminiferous Ether," *Am. J. Sci.* **34** (1887).

[10] H. Rauch, W. Treimer, and U. Bonse, "Test of a single crystal neutron interferometer," *Physics Letters A* **47**, 369 (1974).

[11] Y. Hasegawa, R. Loidl, G. Badurek, M. Baron, and H. Rauch, "Quantum contextuality in a single-neutron optical experiment," *Phys. Rev. Lett.* **97**, 230401 (2006).

[12] Y. Hasegawa, R. Liodl, G. Badurek, M. Baron, and H. Rauch, "Violation of a Bell-like inequality in single-neutron interferometry," *Nature* **425**, 45 (2003).

[13] H. Geppert, T. Denkmayr, S. Sponar, H. Lemmel, and Y. Hasegawa, "Improvement of the polarized neutron interferometer setup demonstrating violation of a Bell-like inequality," *Nucl. Instr. Meth. Phys. Res.* **763**, 417 (2014).

[14] T. Denkmayr, H. Geppert, S. Sponar, H. Lemmel, A. Matzkin, J. Tollaksen, and Y. Hasegawa, "Observation of a quantum Cheshire Cat in a matter-wave interferometer experiment," *Nat. Commun.* **5** (2007).

[15] A. Wagh, G. Badurek, V. Rakhecha, R. Buchelt, and A. Schricker, "Neutron polarimetric separation of geometric and dynamical phases," *Phys. Lett. A* **268**, 209 (2000).

[16] J. H. Hannay, "Angle variable holonomy in adiabatic excursion of an integrable Hamiltonian," *J. Phys. A* **18**, 221 (1985).

[17] A. Danner, "Water Cooled Coils for Spin-Rotation Coupling in Neutron Interferometry," (2017), unpublished project thesis.

[18] W. Demtröder, "Experimentalphysik 1: Mechanik und Wärme," *Springer,* German, (2005).

[19] W. B. Somerville, "The Description of Foucault's Pendulum," *Q. J. R. Astron. Soc* **13** (1972).

[20] F. Bissey, F.-G. Cao, A. R. Kitson, A. I. Signal, D. B. Leinweber, B. G. Lasscock, and A. G. Williams, "Gluon flux-tube distribution and linear confinement in baryons," *Phys. Rev. D* **76**, 114512 (2007).

[21] K. Durstberger, "Geometric phases in quantum theory," *Universität Wien* (2002), Magisterarbeit.

[22] J. Samuel and R. Bhandari, "General Setting for Berry's Phase," *Phys. Rev. Lett.* **60**, 2339 (1988).

[23] Y. Aharonov and J. Anandan, "Phase change during a cyclic quantum evolution," *Phys. Rev. Lett.* **58**, 1593 (1987).

[24] G. Badurek, "Physik polarisierter Neutronen," *TU Wien* (1982), Habilitationsschrift (German).

[25] F. W. Hehl and W.-T. Ni, "Inertial effects of a Dirac particle," *Phys. Rev. D* **42**, 2045 (1990).

[26] L. Ryder, "Relativistic treatment of inertial spin effects," *J. .Phys. A* **31**, 2465 (1998).

[27] J. Chadwick, "Possible Existence of a Neutron," *Nature* **129** (1932).

[28] "The TRIGA Mark-II Reactor," https://ati.tuwien.ac.at/reactor/EN/, description of the reactor on the homepage of the Atominstitut, accessed 4$^{\text{th}}$ March 2018.

[29] Stahlenschutzgesetz § 36b (3), „Betreiber von Forschungsreaktoren haben sicherzustellen, dass keine abgebrannten Brennelemente zur Entsorgung in Österreich anfallen.".

[30] Stahlenschutzgesetz § 36c (1), „Der Bundesminister für Land- und Forstwirtschaft, Umwelt und Wasserwirtschaft wird [...] weiters ermächtigt als Auftraggeber mit der Austrian Research Centers Ges.m.b.H. – ARC oder anderen geeigneten Institutionen [...] als Auftragnehmer Leistungsverträge über die dem Stand der Technik entsprechende Entsorgung radioaktiver Abfälle, beginnend mit deren Sammlung, abzuschließen.".

[31] B. Demirel, "Spin-Rotation-Coupling in Neutron Polarimetry," *TU Wien* (2015), master thesis.

[32] "Bragg diffraction planes," https://commons.wikimedia.org/wiki/File:BraggPlaneDiffraction.svg.

[33] G. Badurek, R. Buchelt, G. Kroupa, M. Baron, and M. Villa, "Permanent magnetic field-prism polarizer for perfect crystal neutron interferometers," *Physica B* **283**, 389 (2000).

[34] T. Habersohn, "Erste experimentelle Versuche zur magnetischen Spintomographie mit Neutronen," *TU Wien* (2006), diploma thesis, German.

[35] E. Jericha, "Vorlesungsskriptum Neutronen und Kernphysik," (2005), unpublished lecture notes (German).

[36] H. Rauch and S. Werner, "Neutron Interferometry," *Oxford University Press* (2015).

[37] S. Sponar, "A short excursion into crystallography," http://www.neutroninterferometry.com/research-overview/interferometry/a-short-excursion-into-crystallography, description of the crystal structure of silicon, accessed 4^{th} March 2018.